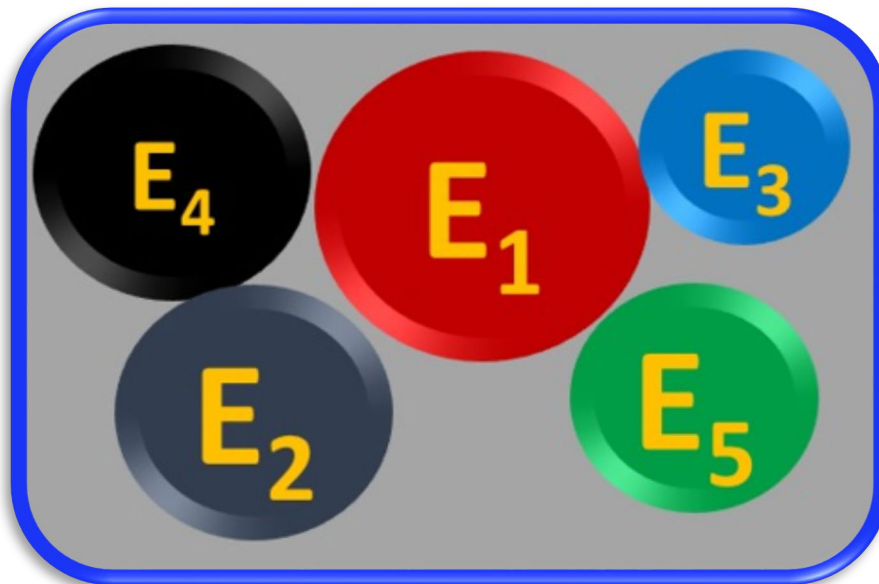


Doctorado en Ingenierías Química, mecánica y fabricación

**TESIS DOCTORAL**

**CARACTERIZACIÓN DEL EFECTO DE MICRODOPAJES  
NOVEDOSOS SOBRE LA ALEACIÓN DE ALTA ENTROPÍA  
CoCrFeMoNi**

Las Palmas de Gran Canaria, mayo de 2023



**Autor:**

Santiago J. Brito García

**Directoras:**

Dra. Julia Claudia Mirza Rosca

Dra. Ionelia Voiculescu



---

---



---

**D. José Miguel Doña Rodríguez, COORDINADOR DEL PROGRAMA DE DOCTORADO en Ingenierías Química, Mecánica y de Fabricación de la UNIVERSIDAD DE LAS PALMAS DE GRAN CANARIA**

**INFORMA,**

De que la Comisión Académica del Programa de Doctorado, en su sesión de fecha ..... tomó el acuerdo de dar el consentimiento para su tramitación, a la tesis doctoral titulada: “CARACTERIZACIÓN DEL EFECTO DE MICRODOPAJES NOVEDOSOS SOBRE LA ALEACIÓN DE ALTA ENTROPÍA CoCrFeMoNi” presentada por el doctorando D. Santiago José Brito García y dirigida por las Doctora Dña. Julia Mirza Rosca.

Y para que así conste, y a efectos de lo previsto en el Art. 11 del Reglamento de Estudios de Doctorado (BOULPGC 04/03/2019) de la Universidad de Las Palmas de Gran Canaria, firmo la presente en Las Palmas de Gran Canaria, a ..... de mayo de dos mil veintitrés.

---



---

---



---

---



---

## AGRADECIMENTOS

Quiero agradecer a los componentes del grupo de investigación, Pedro, Néstor y Iosif que en todo momento me ayudaron y me hicieron sentir uno más en el grupo. También agradecer a Cristina quien no ha dudado en colaborar conmigo desde que se incorporó al grupo hace ya un año. Les deseo lo mejor a todos. Gracias.

También estimar y agradecer el apoyo y la dedicación que han tenido conmigo en todo este tiempo mis Directoras de tesis Dña. Julia Mirza y Dña. Ionelia Voiculescu. Sin sus consejos, indicaciones y correcciones este trabajo no sería el mismo. Mi más sincero agradecimiento.

Pero si este trabajo de tesis ha llegado a buen fin, no me cabe la menor duda de que ha sido por la inestimable comprensión y el apoyo constante que he tenido de mi querida compañera, Mayca. Le estoy eternamente agradecido. Besos.

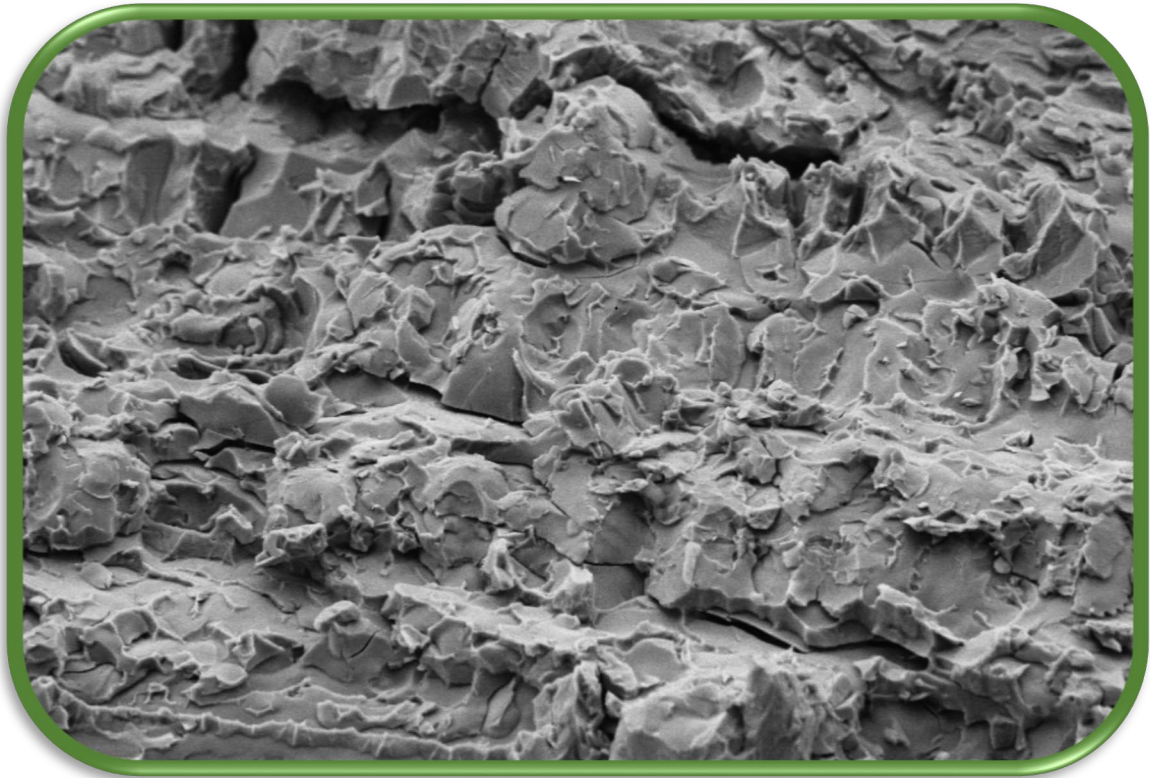
Comparto una frase que encontré una vez navegando por alguna web en internet: “**Nunca sabes de lo que eres capaz hasta que lo intentas**”, me anima a aventurarme a hacer cosas. El tiempo me ha demostrado que es así, con esfuerzo y trabajo, claro. Ahí sigue.

---

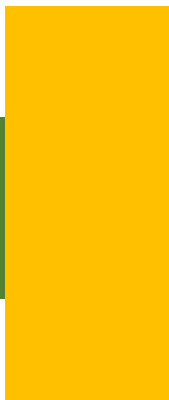


---

---



# Resumen



---



---

---

## Resumen

El **objetivo principal** de este trabajo de tesis es el estudio de las propiedades mecánicas y comportamiento frente a la corrosión en un medio agresivo de la aleación de alta entropía CoCrFeMoNi al ser micro-dopada con los elementos Ti y Zr.

Este objetivo general se aborda a través de los siguientes **objetivos específicos**:

1. Efectos del micro-dopado con Zr sobre las propiedades mecánicas y frente a la corrosión de la aleación de alta entropía CoCrFeMoNi obtenida por refundición por arco al vacío. El estudio electroquímico de la corrosión se realiza en un ambiente altamente corrosivo de agua de mar artificial. Se caracteriza la composición microestructural por microscopía electrónica de barrido (SEM) y se realiza un análisis cualitativo y cuantitativo mediante espectroscopía de rayos X de dispersión de energía (EDS). Las fases presentes se determinan por difracción de rayos X (XRD). Se calcula el módulo de elasticidad E, mediante un ensayo de flexión en tres puntos y la microdureza. Para determinar el comportamiento ante la corrosión se realizan ensayos de potencial a circuito abierto (OCP) espectroscopia de impedancia electroquímica (EIS) y de polarización lineal (PL) en el potencial de corrosión.

2. Efectos del micro-dopado con Ti en el comportamiento de la aleación de alta entropía CoCrFeMoNi en un ambiente corrosivo simulado ante la variación del voltaje desde -1.0 a +0.8 V respecto del electrodo de referencia (SCE). Se analizan los espectros de impedancia obtenidos por espectroscopia de impedancia electroquímica, mediante el ajuste con un circuito eléctrico equivalente de dos constantes de tiempo, una que determina las características de la capa pasiva compacta y otra que determina las propiedades de la capa pasiva porosa.

---

3. Efectos del micro-dopado con Ti en la microestructura, la microdureza y el módulo de elasticidad en la aleación de alta entropía CoCrFeMoNi. La microestructura se consigue observando las muestras, previamente preparadas, por microscopía SEM y XRD. La microdureza se obtiene mediante un ensayo de indentación a diferentes intervalos aplicando una carga constante y, por último, para valorar el módulo de elasticidad se realiza un ensayo a flexión en tres puntos sobre filamentos obtenidos de las muestras.

El tema de tesis propuesto se encuentra relacionado con las siguientes **líneas de investigación** del programa de doctorado en Ingenierías Química, Mecánica y de Fabricación (QUIMEFA):

- Nanomateriales
- Corrosión de los metales

La tesis trata del estudio del efecto del micro dopado de la aleación de alta entropía CoCrFeMoNi con los elementos Ti y Zr y establecer las características mecánicas y electroquímicas que permitan determinar los posibles usos y aplicaciones en los sectores industrial, sanitario, aeroespacial o electrónico entre otros. Por lo tanto, se puede observar que el tema de la tesis es totalmente coherente con las líneas de investigación seleccionadas.

En el artículo “**Mechanical and corrosión behavior of Zr-doped high-entropy alloy from CoCrFeMoNi system**” se analiza el comportamiento frente a la corrosión en ambiente agresivo simulado formado por disolución de NaCl al 3.5 %, la microestructura, la microdureza y el módulo de Young de las aleaciones CoCrFeMoNi y, esta misma aleación, micro-dopada con Zr al 0.71 % en peso. El módulo de Young se obtiene mediante un ensayo de flexión en tres puntos. La corrosión se estudia mediante ensayo de polarización lineal y espectroscopia de

---



---

impedancia electroquímica y se determina la velocidad de corrosión. La microestructura se caracteriza mediante SEM, EDS y XRD.

En el artículo “**EIS Study of doped high entropy alloy**”. Las aleaciones CoCrFeMoNi y CoCrFeMoNi micro-dopada con Ti al 0.36 at % se someten, mediante un ensayo de espectroscopia de impedancia electroquímica, a un rango de potenciales (entre -1.0 a +0.8 V frente al electrodo de referencia) para evaluar su comportamiento ante el cambio de voltaje en un medio agresivo simulado. Los espectros obtenidos se simulan con un circuito equivalente que se ajusta a los datos experimentales y presenta dos constantes de tiempo que se corresponden una con la capa pasiva compacta y la otra con la capa pasiva porosa.

En el artículo “**Impact of Ti doping on the microstructure and mechanical properties of CoCrFeMoNi high entropy alloy**” Se analiza la aleación CoCrFeMoNi y el microdopado con Ti para analizar el efecto que se produce en su microestructura, la microdureza y en el módulo de elasticidad. La microestructura se observa, inicialmente, con un microscopio óptico y posteriormente se realizan observaciones SEM de la superficie para poder obtener los mapas elementales de las muestras. También se realiza un análisis semicuantitativo mediante EDS de las zonas dendríticas, D e interdendríticas ID y se obtiene el grado de segregación,  $S_R$  de los elementos componentes en cada fase.

---



---

---



# Índice



---



---

---

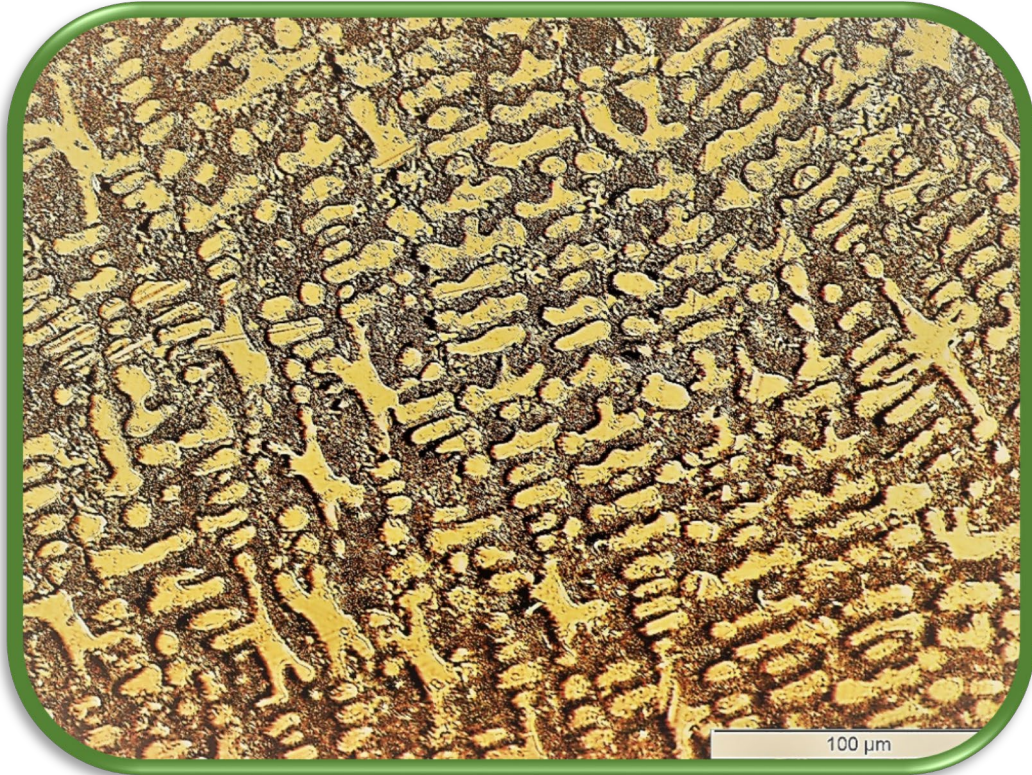
## Índice

.....	2
<b>1. INTRODUCCIÓN</b> .....	<b>2</b>
<b>2. JUSTIFICACIÓN</b> .....	<b>9</b>
<b>3. PUBLICACIONES</b> .....	<b>7</b>
3.1 MECHANICAL AND CORROSION BEHAVIOR OF Zr-DOPED HIGH ENTROPY ALLOY FROM CoCrFeMoNi SYSTEM.....	9
3.2 EIS STUDY OF DOPED HIGH ENTROPY ALLOY.....	12
3.3 IMPACT OF Ti DOPING ON THE MICROSTRUCTURE AND MECHANICAL PROPERTIES OF CoCrFeMoNi HIGH ENTROPY ALLOY .....	14
<b>4. DOCUMENTO DE AUTORÍA</b> .....	<b>17</b>
<b>5. PUBLICACIONES O-PARTICIPADAS</b> .....	<b>23</b>
<b>6. CONCLUSIONES</b> .....	<b>49</b>



---

---



# Introducción

1



---

---

## 1. Introducción

Desde que Yet et al. y Cantor et al. propusieron en sendos artículos en el año 2004 la posibilidad de crear nuevas aleaciones multicomponentes con porcentajes equiatómicos de sus elementos se ha producido un incremento notable en la investigación de estas nuevas aleaciones, que finalmente se han pasado a denominarse Aleaciones de Alta Entropía (HEA), debido a su gran entropía configuracional que nos da una idea del grado de desorden en la disposición de los átomos en la aleación.

La posibilidad de combinar cinco o más elementos en proporciones iguales o aproximadamente iguales abre un amplio abanico de posibilidades en el diseño de nuevos materiales para su posible aplicación en materiales para altas temperaturas para motores de reacción o reactores nucleares también materiales de aleaciones ligeras para aplicaciones aeroespaciales o automovilísticas y recubrimientos resistentes a la corrosión para entornos agresivos. Así mismo se vienen desarrollando HEA para su uso probable en mecanismos electroquímicos que permiten transformar la energía de un combustible en electricidad de manera eficiente y sostenible.

Al combinarse los átomos de manera aleatoria y no existir un elemento predominante se consiguen propiedades excepcionales en los HEA como una muy buena resistencia a la corrosión, alta resistencia, mejores propiedades magnéticas y buena estabilidad a altas temperaturas.

Las investigaciones realizadas se han centrado en la formación de aleaciones con 5 o más elemento y en proporciones equiatómicas o casi equiatómicas a diferencia de las aleaciones

---

tradicionales en las que prima uno o dos elementos principales con la adición de pequeñas cantidades de otros elementos que modifican o mejoran sus propiedades. Desde hace pocos años se vienen realizando una serie de trabajos en aleaciones de alta entropía a las que se les añade micro-dopaje de otro elemento a la aleación base para estudiar su comportamiento en cuanto a la modificación de sus características mecánicas y frente a la corrosión. El efecto del microdopaje depende del elemento dopante añadido, de la concentración y de la aplicación prevista de la aleación.

El **objetivo principal** de este trabajo de tesis es estudiar el comportamiento mecánico y frente a la corrosión en un ambiente químico agresivo de la aleación de alta entropía CoCrFeMoNi al microdoparla con otros elementos, como el Ti, formando la aleación CoCrFeMoNi-Ti y con Zr formando la aleación CoCrFeMoNi-Zr fabricadas mediante fusión por arco al vacío.

Este objetivo general se aborda a través de los siguientes **objetivos específicos**:

- Analizar las características mecánicas y físicas de las aleaciones como la microdureza, la microestructura, el módulo de Young mediante diferentes ensayos y análisis cualitativos y cuantitativos de las muestras.
- Estudio desde el punto de vista de la resistencia a la corrosión de las aleaciones. Dicho estudio se efectúa a partir de medidas del potencial a circuito abierto (OCP), ensayos potencioestáticos y de la aplicación de la técnica de espectroscopía de impedancia electroquímica (EIS).

Por ellos se ha llevado a cabo:

1. El estudio del efecto de la adición de Zr (0.71 % at.) en la aleación CoCrFeMoNi sobre las propiedades mecánicas y su comportamiento ante la corrosión
2. La realización de mediciones de espectroscopía de impedancia electroquímica en las aleaciones CoCrFeMoNi y CoCrFeMoNi-Ti para evaluar la influencia del voltaje en un entorno agresivo simulado. Los espectros se miden entre varios niveles de potencial de -1 a +0.8 V con respecto al electrodo de referencia.
3. El estudio el efecto de la adición de Ti (0.28 % at.) en la aleación CoCrFeMoNi para valorar su influencia en la microestructura, la microdureza y el módulo de elasticidad.
4. El modelado y la simulación con circuitos eléctricos equivalentes del comportamiento en NaCl al 3.5% de las tres aleaciones, CoCrFeMoNi, CoCrFeMoNi-Ti y CoCrFeMoNi-Zr para sus utilizaciones como materiales resistentes a la corrosión en ambientes agresivos.
5. La realización de un ensayo de flexión en tres puntos de las muestras para calcular el módulo de elasticidad de cada aleación, aplicando la teoría de vigas considerando una carga puntual centrada en una viga simple apoyada.
6. La observación por microscopía óptica de la microestructura de las superficies de las muestras tratadas previamente.
7. La observación por microscopía electrónica de barrido (SEM) de la superficie de las muestras para obtener información de la topología de la superficie para determinar el tipo de rotura producido y definir la ductilidad y fragilidad de la fractura.

8. El análisis mediante EDS de la composición química de las aleaciones y de la distribución de la concentración de elementos en una zona determinada y calcular el factor de segregación ( $S_R$ ) para evaluar el grado de segregación de la aleación y poder compararlo con el resto de aleaciones.
9. Un análisis por difracción de rayos X (XRD) para conocer las fases cristalinas que se forman en la microestructura analizando los patrones obtenidos.
10. La realización de un ensayo de indentación Vickers para conocer la microdureza de cada muestra en función de la huella obtenida.

Las publicaciones científicas derivadas de esta tesis doctoral cubren las estrategias mencionadas. En total, se presentan 3 artículos publicados como primer autor, varios artículos como autor o coautor y comunicaciones orales y en poster a varias conferencias internacionales. Todas estas publicaciones suponen el núcleo central del trabajo desarrollado, justificando la unidad temática y permitiendo la presentación de la presente tesis bajo la modalidad de **tesis por compendio de publicaciones**.

El tema de tesis propuesto se encuentra relacionado con las siguientes líneas de investigación del programa de doctorado en Ingenierías Química, Mecánica y de Fabricación (QUIMEFA):

- Nanomateriales
- Corrosión de los metales

La tesis trata del estudio mecánico y electroquímico varias aleaciones de alta entropía tomando como base la formada por CoCrFeMoNi, microdopada con los elementos Ti, formando una primera aleación y Zr que constituye la segunda aleación, y determinar su posible

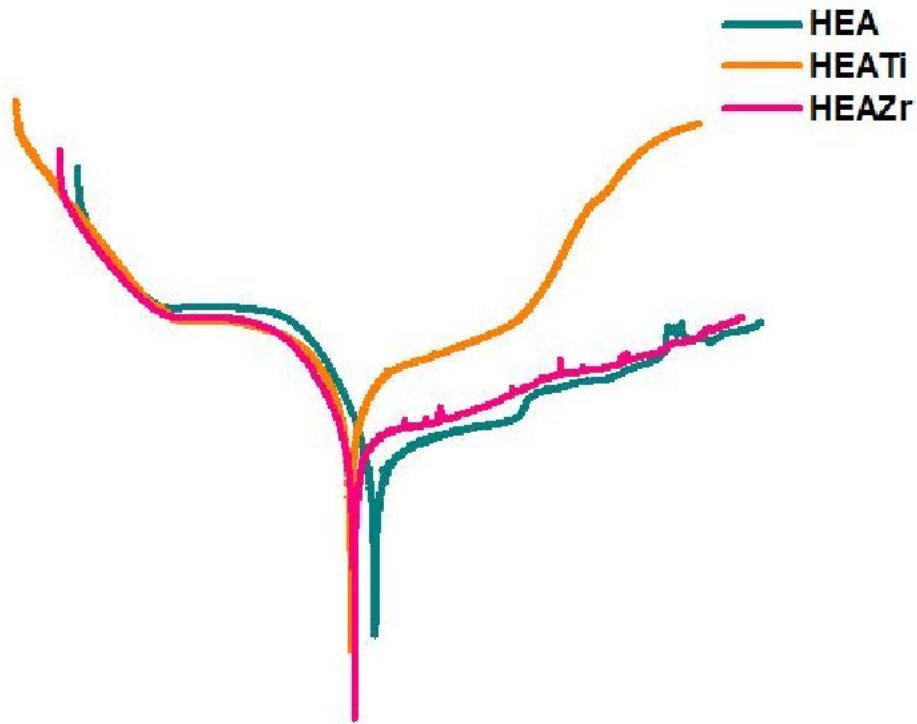
---



---

uso en los sectores industriales que necesiten de materiales novedosos que cumplan los requisitos exigentes que requiere su actividad, como la industria aeroespacial, la energía nuclear, los biomateriales o la industria de componentes electrónicos entre otras. Por lo tanto, se puede observar que el tema de la tesis es totalmente coherente con las líneas de investigación seleccionadas.





# Justificación del compendio

2



---

## 2. Justificación del compendio

Las publicaciones científicas básicas derivadas de esta tesis doctoral son 3 artículos publicados como primer autor. Hay 2 artículos más aceptados para publicación indexados JCR en el cuartil Q1 en los que soy el primer autor. También estoy como primer autor en 4 capítulos de libro y en 1 como co-autor. he participado en 5 congresos con pósteres de los que en 4 estoy como primer autor). Un resumen de cada publicación básica se presenta a continuación:

---

**TÍTULO :** “Mechanical and Corrosion Behavior of Zr-Doped High-Entropy Alloy from CoCrFeMoNi System”

---

**AUTORES:** Santiago Brito-Garcia; Julia Mirza-Rosca; Victor Geanta; Ionelia Voiculescu

---

**REVISTA:** Materials

---

**ÍNDICE DE IMPACTO:** 3.748

---

**CUARTIL:** Q1

---

**DOI:** 10.3390/ma16051832.

---

**ISSN:** 1996-1944

---

**EDITORIAL:** MDPI

---

**MES Y AÑO:** 02/2023

---

**VOLUMEN:** 16

---

**PÁGINAS:** 14

---

El objetivo del trabajo es estudiar el efecto de la adición de Zr sobre las propiedades mecánicas y el comportamiento frente a la corrosión de una aleación de alta entropía del sistema CoCrFeMoNi. Esta aleación se diseñó para ser utilizada en componentes de la industria geotérmica expuestos a altas temperaturas y a la corrosión. Dos aleaciones, una sin Zr



(denominada Muestra 1) y otra dopada con 0,71 % en peso de Zr (denominada Muestra 2), se obtuvieron en un equipo de refundición por arco en vacío a partir de materias primas granulares de gran pureza. Se realizó la caracterización microestructural y el análisis cuantitativo mediante SEM y XRD. Los valores del módulo de Young de las aleaciones experimentales se calcularon a partir de un ensayo de flexión en tres puntos. El comportamiento frente a la corrosión se estimó mediante ensayo de polarización lineal y mediante espectroscopia de impedancia electroquímica. La adición de Zr dio lugar a una disminución del valor del módulo de Young, pero también a una disminución de la resistencia a la corrosión. El efecto beneficioso del Zr sobre la microestructura fue el refinamiento del grano, lo que garantizó una buena desoxidación de la aleación.

---

**TÍTULO :** “EIS Study of Doped High-Entropy Alloy”

---

**AUTORES:** Santiago Jose Brito-Garcia; Julia Claudia Mirza-Rosca;  
Cristina Jimenez-Marcos; Ionelia Voiculescu

---

**REVISTA:** Metals

---

**ÍNDICE DE** 2.695  
**IMPACTO:**

---

**CUARTIL:** Q2

---

**DOI:** 10.3390/met13050883

---

**ISSN:** 2075-4701

---

**EDITORIAL:** MDPI

---

**AÑO:** 2023

---

**VOLUMEN:** 13

---

**PÁGINAS:** 17

---

Los prometedores resultados obtenidos en la investigación de aleaciones de alta entropía fomentan cada vez más nuevas configuraciones de estas aleaciones. Nuestra investigación se realizó sobre la aleación CoCrFeMoNi de alta entropía y la aleación CoCrFeMoNi dopada con



---

Ti. Se realizaron medidas de espectroscopia de impedancia electroquímica (EIS) en muestras de alta entropía CoCrFeMoNi con y sin microdopaje de Ti para evaluar la influencia del voltaje en su comportamiento en un entorno agresivo simulado. Los espectros de impedancia se midieron entre -1.0 y +0.8 V vs. SCE a varios niveles de potencial. Se analizaron los espectros de impedancia utilizando un circuito eléctrico equivalente para ajustarlos a los datos experimentales. El circuito correspondiente que se ajusta con éxito a los espectros tiene dos constantes de tiempo: la primera corresponde a los atributos de la capa pasiva compacta y la segunda a las características de la capa pasiva porosa. Los resultados muestran que el dopado de la aleación CoCrFeMoNi con 0,36 at. % de Ti reduce la capacidad de la aleación para resistir la corrosión, ya que la aleación puede reaccionar más rápidamente con el ambiente circundante lo que provoca una disminución de la resistencia a la corrosión de la aleación.

---

**TÍTULO : “Impact of Ti Doping on the Microstructure and  
Mechanical Properties of CoCrFeMoNi High-Entropy**

---

**AUTORES: Santiago Jose Brito-Garcia, Julia Claudia Mirza-Rosca,  
Cristina Jimenez-Marcos y Ionelia Voiculescu**

---

**REVISTA: Metals**

---

**ÍNDICE DE  
IMPACTO: 2.695**

---

**CUARTIL: Q2**

---

**DOI: 10.3390/met13050854**

---

**ISSN: 2075-4701**

---

**EDITORIAL: MDPI**

---

**MES Y AÑO: 04/2023**

---

**VOLUMEN: 13**

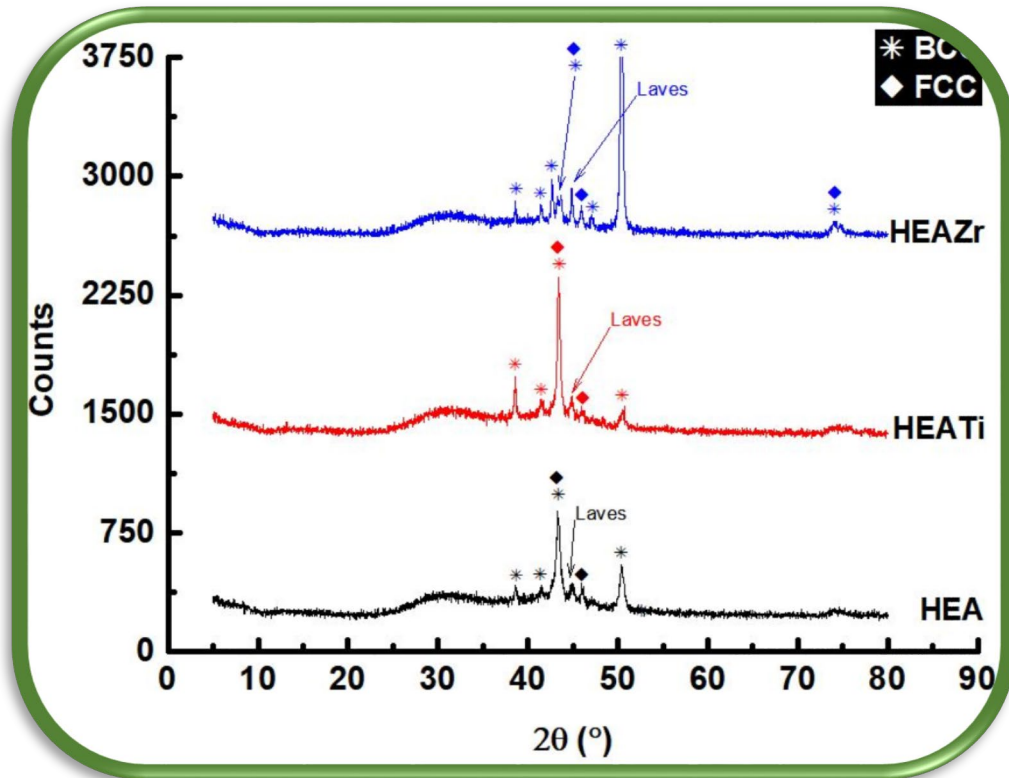
---

**PÁGINAS: 13**

---

El principio de diseño de las aleaciones de alta entropía consiste en mezclar muchos elementos químicos en proporciones iguales o casi iguales para crear nuevas aleaciones con

propiedades únicas y especiales, como alta resistencia, ductilidad y resistencia a la corrosión. Algunas propiedades de las aleaciones de alta entropía pueden ajustarse mediante la introducción de nuevos elementos dopantes, que se seleccionan en función de las condiciones de trabajo. Se examinó la aleación de alta entropía CoCrFeMoNi para determinar el impacto del dopado de Ti en su microestructura, microdureza y módulo elástico. El análisis de la microestructura reveló una estructura central consistente en fases cúbicas centradas en la cara (FCC) y cúbicas centradas en el cuerpo (BCC), junto con la formación de una fase Laves. La adición de Ti hizo que los granos de la aleación fueran más finos y redujo la diferencia de concentración de Mo entre las regiones interdendríticas y dendríticas. Como resultado del dopado con Ti, la microdureza de la aleación aumentó de 369 HV 0,2 a 451 HV 0,2. El dopado con Ti produjo una duplicación del valor de la resistencia a la rotura, aunque no se observaron cambios significativos en el módulo elástico de la aleación CoCrFeMoNi.





---

### 3. Publicaciones

3.1 *Mechanical and corrosion behavior of Zr-doped high entropy alloy from CoCrFeMoNi system*

---

**TÍTULO :** “Mechanical and Corrosion Behavior of Zr-Doped High-Entropy Alloy from CoCrFeMoNi System”

---

**AUTORES:** Santiago Brito-Garcia; Julia Mirza-Rosca; Victor Geanta; Ionelia Voiculescu

---

**REVISTA:** Materials

---

**ÍNDICE DE IMPACTO:** 3.748

---

**CUARTIL:** Q1

---

**DOI:** 10.3390/ma16051832.

---

**ISSN:** 1996-1944

---

**EDITORIAL:** MDPI

---

**MES Y AÑO:** 02/2023

---

**VOLUMEN:** 16

---

**PÁGINAS:** 14

---



## Article

# Mechanical and Corrosion Behavior of Zr-Doped High-Entropy Alloy from CoCrFeMoNi System

Santiago Brito-Garcia <sup>1</sup>, Julia Mirza-Rosca <sup>1,\*</sup> , Victor Geanta <sup>2</sup> and Ionelia Voiculescu <sup>2</sup> <sup>1</sup> Mechanical Engineering Department, Las Palmas de Gran Canaria University, 35017 Tafira, Spain<sup>2</sup> Faculty of Industrial Engineering and Robotics, Politehnica University of Bucharest, 313 Splaiul Independentei, 060042 Bucharest, Romania

\* Correspondence: julia.mirza@ulpgc.es

**Abstract:** The aim of the paper is to study the Zr addition effect on the mechanical properties and corrosion behavior of a high-entropy alloy from the CoCrFeMoNi system. This alloy was designed to be used for components in the geothermal industry that are exposed to high temperature and corrosion. Two alloys, one Zr-free (named Sample 1) and another one doped with 0.71 wt.% Zr (named Sample 2), were obtained in a vacuum arc remelting equipment from high-purity granular raw materials. Microstructural characterization and quantitative analysis by SEM and EDS were performed. The Young modulus values for the experimental alloys were calculated on the basis of a three-point bending test. Corrosion behavior was estimated by linear polarization test and by electrochemical impedance spectroscopy. The addition of Zr resulted in a decrease in the value of the Young modulus but also in a decrease in corrosion resistance. The beneficial effect of Zr on the microstructure was the grain refinement, and this ensured a good deoxidation of the alloy.

**Keywords:** HEA; CoCrFeMoNiZr; microstructure; corrosion; EIS; Young modulus



**Citation:** Brito-Garcia, S.; Mirza-Rosca, J.; Geanta, V.; Voiculescu, I. Mechanical and Corrosion Behavior of Zr-Doped High-Entropy Alloy from CoCrFeMoNi System. *Materials* **2023**, *16*, 1832. <https://doi.org/10.3390/ma16051832>

Academic Editors: Jeong Min Park and Jongun Moon

Received: 12 January 2023

Revised: 8 February 2023

Accepted: 20 February 2023

Published: 23 February 2023



**Copyright:** © 2023 by the authors. Licensee MDPI, Basel, Switzerland. This article is an open access article distributed under the terms and conditions of the Creative Commons Attribution (CC BY) license (<https://creativecommons.org/licenses/by/4.0/>).

## 1. Introduction

Since 2004, when Yeh et al. [1] and Cantor et al. [2] published the results of multicomponent equiatomic alloys, eventually called high-entropy alloys (HEAs), combinations of many components have been developed due to their improved properties compared to classic alloys (of a main element with more than 50 at.%). Yeh et al. defined these alloys as containing a minimum of five components that account for between 5% and 35% by atomic weight.

Cantor was the first to create an equiatomic alloy from the CoCrFeMnNi system, and it was observed that the mechanical characteristics of high-entropy alloys rely on chemical composition and microstructure [2,3]. If certain thermomechanical treatments are applied to this alloy, its mechanical properties can be considerably improved. For example, after treatment, the yield strength reaches up to 1834 MPa and the ultimate tensile strength rises to 2069 MPa, with uniform elongation of 1.4% and total elongation of 7.4% at room temperature. This alloy has high fracture resistance and low-temperature ductility, although there have been only few investigations on how it react to corrosion. In some chemical conditions, such as those containing chlorides, the corrosion resistance of this alloy is not noticeably higher even if the amount of Cr and Ni is higher than that of stainless steels (such as AISI 304) [4–6].

The elements selected for the CoCrFeMnNi alloy belong to the 3d and 4d transition metal groups. In Fe-base alloys, Cr is a passivating element [7,8]; together with Ni, it provides good corrosion behavior in line with the main elements in stainless steels. By increasing the Cr content from 4.76 at.% to 33.36 at.% in AlCrCoFeNi alloy, the hardness increases from 390 to 551 HV0.1, and a good combination of strength and ductility is obtained [9–11]. Co also improves the high-temperature resistance and tensile properties [12–15]. The high ultimate tensile strength (UTS) of multielement CoCrNi alloy is about

740 MPa; however, after grain size refinement, it can reach 1000 MPa. Furthermore, the elongation at fracture of this alloy is about 50%. The yield strength can be increased to about 1 GPa in the case of the CoCrNi–3W alloy, which is almost double compared to the CoCrNi alloy (400–500 MPa) [16]. The energy threshold for the mobility of Mn atoms is usually lower than that of Co and Ni atoms, which allows it to diffuse more easily [17] but the corrosion resistance decreases [18]. The alloying of CoCrFeNi with Nb and Mo allows to obtain of yield strength of 426 MPa and a fracture strength of 714 MPa, with elongation of 17.4% [19].

We decided to modify the alloy recipe proposed by Cantor using another element instead of Mn, such as Mo, to increase the yield strength, ultimate strength, and hardness. Some researchers used metalloids, such as Si and Ge, to simultaneously increase the yield strength, ultimate strength, and ductility, due to the supplementary covalent bonding and reinforcement effect of solid solution [20–22].

The replacement of Mn with tungsten, reported for the CoCrFeNiW<sub>x</sub> alloy, caused an increase in hardness proportional to the W concentration [23].

It was found that, by reducing the Mn concentration (to 5 at.% Mn), the CoCrFeMnNi alloy acquires higher yield strength values after annealing at 1117 K (from 387 to 477 MPa) due to the grain refinement effect (from 4.4 to 2.61 μm) [10]. Mn also shows a rapid evaporation effect during melting processes; hence, in our study, this element was replaced by Mo, which could improve the resistance to high temperatures [24]. Co–Cr–Mo alloy is widely used for manufacturing of vanes and gas turbines due to its excellent fatigue behavior and wear resistance [25–28]. In such alloys, molybdenum has a beneficial effect on passivation capacity, contributing to the formation of a protective surface layer that allows pitting corrosion to be limited [29,30]. Studies were conducted to estimate the effects on the microstructure and properties of alloys with different Mo contents [31–33]. Such alloys have been designed for the manufacture of furnace casings and chemical tanks used in high-temperature and corrosion conditions [34], for components used in the geothermal industry [35,36], or to obtain high-performance coatings [37].

The addition of Zr to multielement alloys allows the improvement of some mechanical properties [38]; thus, in TiMoNbZr<sub>x</sub> alloy, Zr determined the improvement of wear resistance, due to the formation of an oxide film that acts as a lubricant [39]. In terms of corrosion resistance, grain refinement plays a great role, and a small addition of Zr can contribute to grain refinement [40]. Thus, our study focuses on the use of the Mo and Zr in an HEA for the manufacture of mechanical parts used in the geothermal industry at high temperature and in corrosive media.

The impact of Zr addition on the CoCrFeNiMo high-entropy alloy's microstructure, elastic modulus, and corrosion characteristics is examined in this work. In order to analyze the microstructure of the samples with and without Zr, optical microscopy, scanning electron microscopy (SEM), and energy-dispersive X-ray spectroscopy (EDS) are employed, microhardness tests are performed, a three-point bending test is used to evaluate the modulus of elasticity and linear polarization (LP), and electrochemical impedance spectroscopy (EIS) is applied to examine electrochemical responses, corrosion kinetics, and interface parameters.

## 2. Materials and Methods

### 2.1. Material Preparation

On the basis of the CoCrFeNiMn combination, Mn was replaced by Mo, and a high-entropy alloy was created, generating Sample 1. To improve the mechanical properties, this alloy was then doped with Zr in a proportion of 0.71% by weight, creating Sample 2. The elements utilized to create these alloys were 99.00% pure, and the resulting alloys contained the weight percentages and atomic percentages given in Table 1.

The ingots of each alloy were prepared at LAMET laboratory, Romania, with VAR (vacuum arc melting) model MRF ABJ 900 VAR (Allenstown, Merrimack, NH 03275, USA), under a protective argon atmosphere, and six remelting operations were performed for complete homogenization.

**Table 1.** Chemical composition of the experimental alloys.

Element	wt.%		at.%	
	Sample 1	Sample 2	Sample 1	Sample 2
Co	20.67	20.34	21.52	21.15
Cr	19.99	19.80	23.58	23.33
Fe	19.88	20.23	21.84	22.20
Mo	20.20	19.18	12.92	12.25
Ni	19.27	19.74	20.14	20.60
Zr	-	0.71	-	0.48

The samples were prepared from ingots after cutting and embedding in epoxy resin. The specimens were ground using emery discs on a Tegrapol-11 Struers (Copenhagen, Denmark) polishing machine, and then each sample was polished applying a 0.1  $\mu\text{m}$  alumina suspension on a polishing cloth until it yielded a mirror-like surface, without scratches. Following an ethanol wash, the samples were rinsed with distilled water. The electrical contact between the sample and the potentiostat connection clamp was established using a copper wire.

Using ImageJ, version 1.53 k (public domain), each sample's surface area  $S$  was calculated; for this, 10 measurements each were taken. For each alloy, the equivalent weight  $E_w$  (in g/eq) and density  $\rho$  (in  $\text{g}/\text{cm}^3$ ) values were also computed (see Table 2).

**Table 2.** Data of surface area, density and equivalent weight of specimens.

	$S$ ( $\text{cm}^2$ )	$\rho$ ( $\text{g}/\text{cm}^3$ )	$E_w$ (g/eq)
Sample 1	$0.567 \pm 0.002$	8.635	23.694
Sample 2	$0.676 \pm 0.002$	8.602	23.814

In this case, the equivalent weight of each sample was calculated using the atomic weight of each element ( $M_i$ ), its valence number ( $n_i$ ), and  $C_i$  (its weight percentage), as shown in the following equation:

$$E_w = \sum_{i=1}^k \frac{M_i}{n_i} \cdot C_i \quad (1)$$

The alloy density was calculated as follows:

$$\rho = \sum_{i=1}^k \rho_i \cdot C_i \quad (2)$$

where  $\rho_i$  ( $\text{g}/\text{cm}^3$ ) is the density of each element, and  $C_i$  is its weight percentage.

## 2.2. Microstructural Characterization

The microstructure of the alloys was analyzed using an environmental scanning electron microscope (ESEM) model Fei XL30 ESEM (MTM, Leuven, Belgium) equipped with a LaB6 cathode coupled to an energy-dispersive X-ray electron probe analyzer (EDAX Sapphire) used to determine the chemical composition of the samples. Prior to microstructural characterization, the samples were prepared according to ASTM E3-11 (2017) standard for metallography [41]. Phase analysis was characterized using an X-ray diffractometer (XRD) with an Empyrean diffractometer (Malvern-Panalytical). For the analysis  $\text{CuK}\alpha$  radiation (1.5406  $\text{\AA}$ ) in the range of  $2\theta = 30^\circ$ – $100^\circ$  with a step size of  $0.04^\circ$  at a power of 45 kV was used.

## 2.3. Modulus of Elasticity and Microhardness

A three-point bending test was performed to obtain the modulus of elasticity of the material. For this purpose, the samples were cut with an IsoMet<sup>®</sup> 4000 Buehler precision

linear saw (BUEHLER, Lake Bluff, IL, USA), which is capable of achieving minimal distortion of the material. Ten specimens were selected from each alloy to obtain a weighted average of the results; the specimens had the shape of rectangular section filaments of variable dimensions due to the irregular shape of the ingot obtained in the casting of the alloy. The support spacing (L) in the test for Sample 1 and Sample 2 was 12.70 mm and 8.95 mm, respectively.

Once the samples were obtained, a three-point bending test was performed using the Electroforce 3100 equipment (BOSE Corporation, Eden Prairie, Minnesota, USA), until material breakage was reached or until the maximum equipment load of 22 N was applied, all in compliance with ISO 7438:2020 [42].

Microhardness tests were performed at 24 °C and 48% humidity using a Shimadzu HMV 2T microhardness equipment (Tokyo, Japan). According to ISO 14577-1:2015 [43], 10 indentations were made for each sample, and a load of 1.96 N was applied.

#### 2.4. Electrochemical Measurements

Sample 1 and Sample 2 were subjected to corrosion tests in a 3.5% NaCl solution using Biologic SP-150 potentiostat (Seyssinet-Pariset, France). For the execution of the techniques and the establishment of the process parameters, the EC-Lab<sup>®</sup> v-9.55 program was employed, which also allows the plotting of the data obtained, as well as the calculation of the polarization resistance ( $R_p$ ), the Tafel coefficients, and the remaining electrochemical parameters.

The tests were carried out in a standard electrochemical cell with three electrodes, consisting of the sample to be tested as a working electrode, a saturated calomel electrode (SCE) as the reference electrode, and a platinum electrode as the counter electrode. Previously, the open-circuit potential was recorded by immersing the samples for 24 h in the salt solution. These tests were performed three times to ensure reasonably reproducible quality.

The linear polarization test establishes the linear relationship between the applied polarization and the current response in the vicinity of the corrosion potential ( $E_{\text{corr}}$ ). In this case, the potential range of  $25 \text{ mV} \pm 1$  versus  $E_{\text{corr}}$  and a sweep rate of 0.166 mV/s were used, and the polarization resistance was calculated. For potentiodynamic polarization curves, a scan of potential from  $-1.2 \text{ V vs. SCE}$  to  $+1.2 \text{ V vs. SCE}$  was performed.

Additionally, the EIS test was performed using single sine wave measurements at frequencies in the range of  $10^{-1}$  to  $10^5$  Hz for the two alloys. From this test, it was possible to relate the chemical and physical properties of the prepared alloys to the electrochemical process taking place by analyzing the spectra obtained. Therefore, the ZSimpWin 3.22 program (AMETEC, Princeton, NJ, USA), which allows the interpretation of the EIS data, was used to obtain and analyze the spectra. In addition, from the obtained data, an equivalent circuit was fitted in order to interpret the behavior of the electrolyte/sample interface and the state of the surface layer.

### 3. Results and Discussion

#### 3.1. Microstructural Characterization

Representative SEM images of the two HEAs are presented in Figure 1a,b, both of which showed a compact microstructure, without cracks. The microstructure of both alloys was dendritic, with a grain refinement tendency in the case of Sample 2. A semi-quantitative analysis was performed in order to reveal the chemical composition of the investigated samples on the micro-areas labeled Area 1 and Area 2. Table 3 presents the quantified values and estimated uncertainties of the elements found in the alloys' composition. From the EDS analysis, it can be observed that the dendritic zone, labeled Area 1 in both samples, was rich in Ni, Fe, and Co. Area 2, corresponding to the interdendritic space, was made up of alloy rich in Cr and Mo, with the concentration of elements such as Co, Fe, and Ni being slightly lower. Low concentrations of Zr were identified in Sample 2, with slightly higher concentrations in the interdendritic areas. A comparative analysis of the microstructure of the two alloys highlights that the volume fraction of the interdendritic zones decreased when Zr was added to the CoCrFeMoNi alloy. In this type of alloy, the  $\sigma$  phase frequently

appeared alongside the FCC structure. The addition of Mo to the CoCrFeNi system caused the formation of eutectic containing intermetallic phases ( $\sigma$  and  $\mu$ ) in the FCC phase. The eutectic microstructure influences the mechanical properties, determining the increase in hardness and yield strength [44]. The key elements favoring the appearance of the  $\sigma$  phase are Mo and Cr, whose concentrations are higher in the interdendritic zone [44]. In the high-entropy alloy CoCrFeNiMo, about 14% Cr- and Mo-rich  $\sigma$  phase was identified [19]. In our alloys, the addition of 0.48 at.% Zr caused the Mo concentration to decrease from 20 at.% to 17 at.% in the interdendritic zones, while the Cr concentration remained almost unchanged, at approximately 25 at.%. In this way, the tendency to form the sigma phase was diminished.

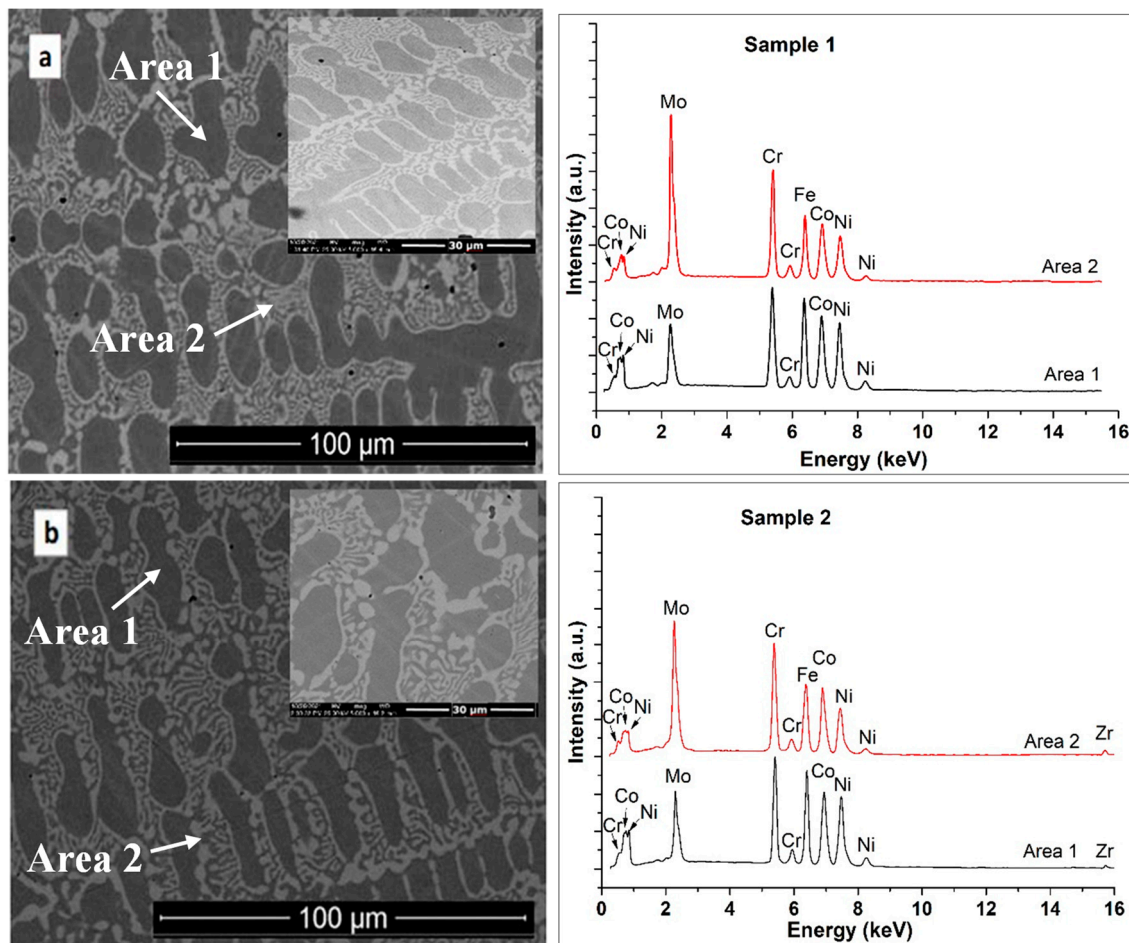


Figure 1. SEM micrographs and corresponding EDS spectra for sample 1 (a) and sample 2 (b).

Table 3. EDS quantification results.

	Sample 1				Sample 2			
	Area 1		Area 2		Area 1		Area 2	
El.	wt.%	at.%	wt.%	at.%	wt.%	at.%	wt.%	at.%
Mo	13.86	8.85	30.55	20.61	13.64	8.51	26.07	17.13
Cr	19.23	22.07	20.42	25.12	19.28	22.2	20.58	24.96
Fe	22.02	23.53	16.29	18.66	22.21	23.81	17.97	20.29
Co	22.49	22.78	18.34	19.91	21.74	22.09	18.92	20.25
Ni	22.41	22.78	14.40	15.69	22.54	22.99	15.55	16.82
Zr	-	-	-	-	0.59	0.39	0.80	0.55

Table 3 shows the chemical composition determined using the EDS method, where a higher concentration of Mo and Zr in the interdendritic areas can be noted. The X-

ray diffraction patterns for both investigated samples are shown in Figure 2. The alloys presented an FCC solid solution with some weak peaks, in addition to the (111) high-intensity peak. Thus, the lower-intensity peaks were attributed to the secondary  $\sigma$  phase, corresponding to the rich Cr- and Mo-rich areas determined in the EDS investigations.

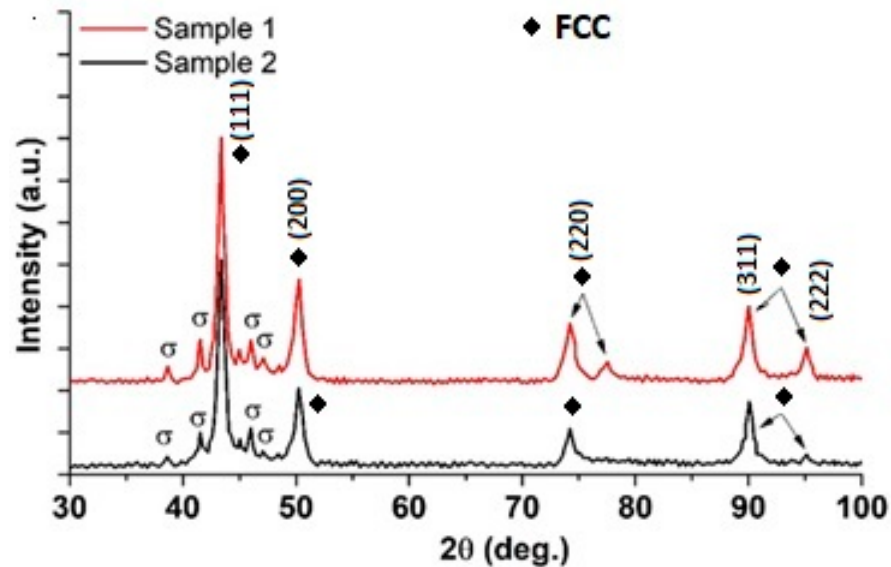


Figure 2. XRD patterns of the investigated alloys.

### 3.2. Modulus of Elasticity and Microhardness

The load–displacement diagrams were obtained for the two samples using the three-point bending test. Figure 3 shows one of the graphs for each specimen (10 samples of each alloy were tested) and the straight-line results within the elastic limit of the alloy (i.e., when the sample recovers its initial shape after deformation). The gradient of this line is

$$\frac{dF}{dw} = \frac{48EI}{L^3}, \quad (3)$$

where  $E$  is the Young's modulus of the sample of length  $L$ , which rests on two roller supports and is subject to a concentrated load  $F$  at its center having a central deflection  $w$ .  $I$  is the second moment of area, defined by

$$I = \frac{a^3b}{12}, \quad (4)$$

where  $a$  is the sample's depth, and  $b$  is the sample's width. Thus, the average value of the modulus of elasticity of each of the proposed alloys was calculated. The obtained results highlight that the alloy without Zr had a higher modulus of elasticity than that to which Zr was added, as presented in Table 4.

It was found that the value obtained for Sample 1 was 20.5% higher than the value reached by the Sample 2; the addition of Zr produced a decrease in the modulus of elasticity and, therefore, in its stiffness.

The microhardness values HV0.2 and the standard deviation for the 10 measurements of each sample are presented in Table 4. It can be observed that the addition of Zr improved the average microhardness of HEAs. The SEM images of the fracture surfaces of the two alloys are presented in the Figure 4; it can be observed that that a brittle fracture occurred in both samples. A cleavage-like fracture plane can also be observed.

### 3.3. Electrochemical Measurements

The samples were immersed in 3.5% NaCl solution, and the open-circuit potential (OCP) was recorded as a function of time up to 24 h. The OCP values changed continuously,

fluctuating more rapidly during the first hours of immersion and reaching relatively stationary values only after 24 h. Was observed that the OCP values after 24 h of immersion were negative for both Sample 1 ( $-342 \pm 63$  mV vs. SCE) and Sample 2 ( $-458 \pm 43$  mV vs. SCE). This negative shift was related to the alteration of the film from the sample surface. The steady-state potentials corresponding to the corrosion potential ( $E_{\text{corr}}$ ) were obtained. Then, the linear polarization test in a potential range of  $25 \text{ mV} \pm 1$  versus  $E_{\text{corr}}$  was performed, and the polarization resistance  $R_p$  was obtained. Tafel measurements were started from the cathodic to anodic direction in the range of  $-1.2 \text{ V}$  to  $+1.2 \text{ V}$  vs. SCE in order to obtain the Tafel slopes.

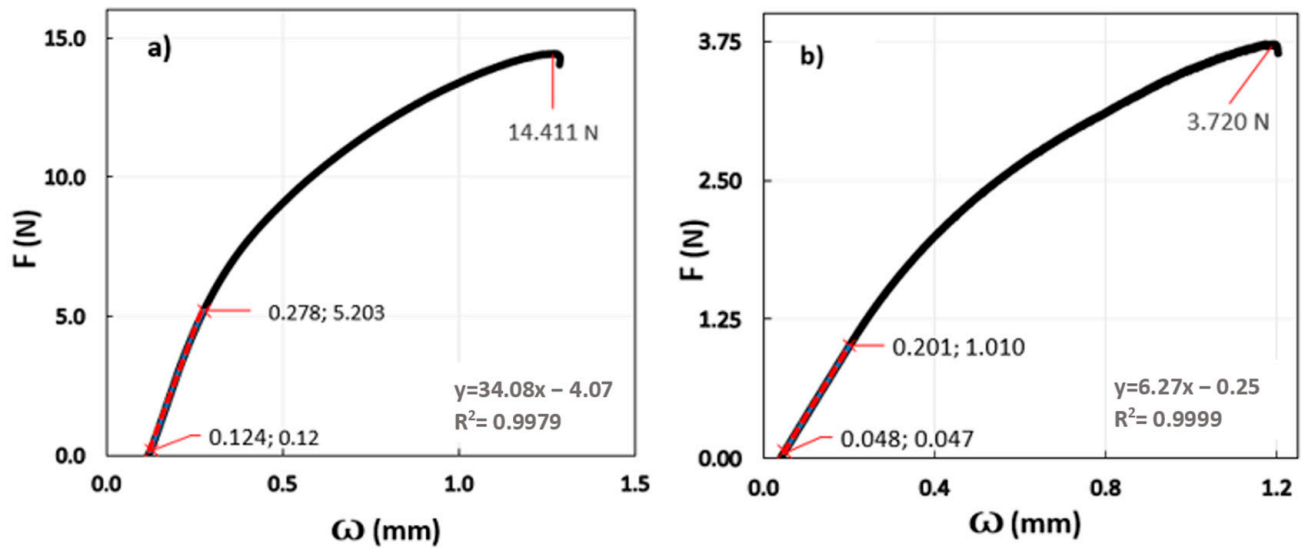


Figure 3. Three-point flexural test diagrams: (a) Sample 1 and (b) Sample 2.

Table 4. Modulus of elasticity and hardness values for Sample 1 and Sample 2.

Alloy	Modulus of Elasticity (GPa)	Microhardness (HV0.2)
Sample 1	$173.99 \pm 4.25$	$369.2 \pm 0.6$
Sample 2	$144.33 \pm 5.38$	$402.6 \pm 0.7$

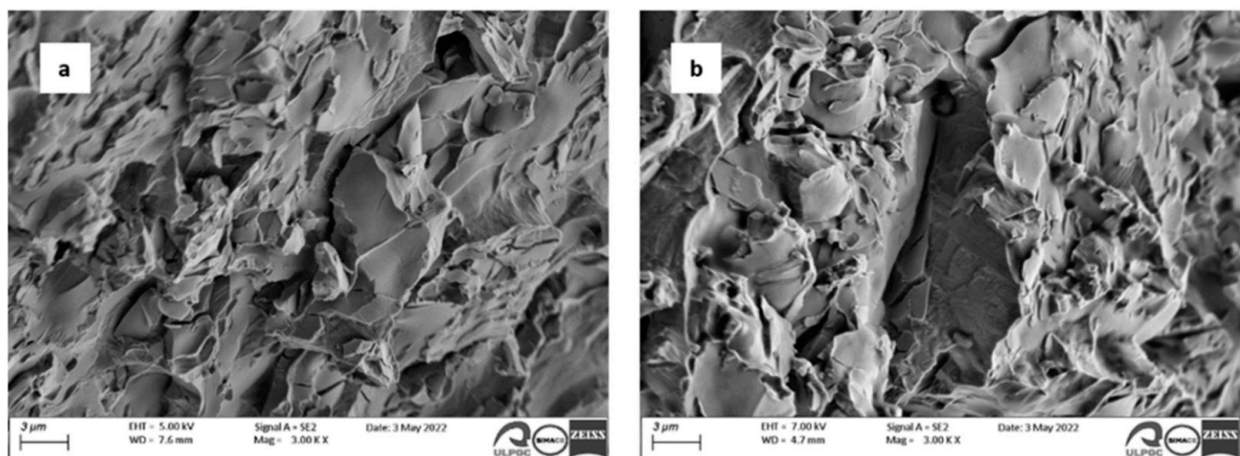
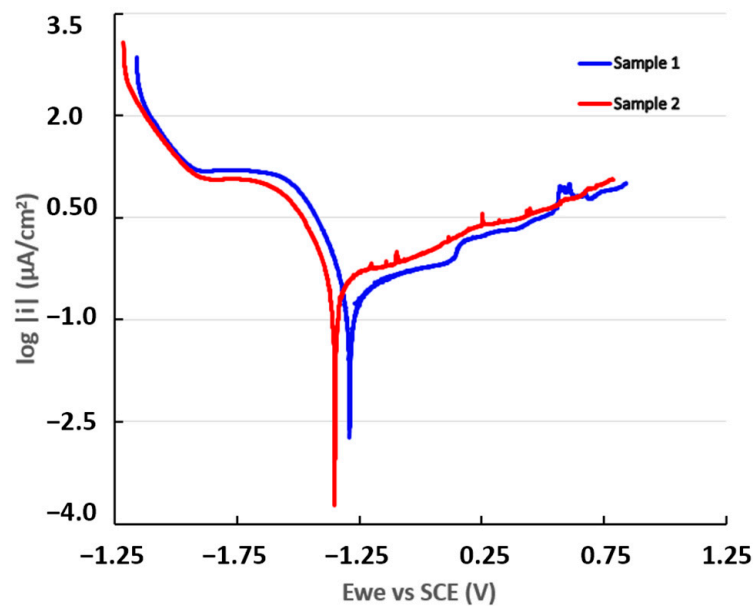


Figure 4. SEM images of the fracture after three-point bending test: (a) Sample 1 and (b) Sample 2.

The potentiodynamic polarization curves were obtained during the tests carried out to estimate the corrosion rate (CR) of the samples. The current values are presented on a semi-logarithmic scale in Figure 5.



**Figure 5.** Potentiodynamic polarization curves for Sample 1 and Sample 2.

The potentiodynamic polarization curves showed an increase in anodic current densities with the addition of zirconium to Sample 2, indicating a decrease in corrosion resistance in the conditions of simulated seawater used in experimental tests. In the anodic range of both curves, small increases of the current were observed, suggesting the acceleration of the oxidation reaction due to local corrosion and repassivation processes.

The value of the cathodic current density decreased with the addition of zirconium. Consequently, this implies that, in the simulated environment used for testing, the zirconium acted as an inhibitor of the cathodic reaction, restricting the hydrogen evolution process.

The corrosion rate was calculated as follows:

$$CR = \frac{I_{corr}KE_w}{\rho A}, \quad (5)$$

where  $I_{corr}$  is the corrosion current (A),  $K$  is the constant that defines the units of corrosion rate (3272 m/A·cm·year),  $E_w$  is the equivalent weight (g/equivalent),  $\rho$  is the density (g/cm<sup>3</sup>), and  $A$  is the sample area (cm<sup>2</sup>).

Table 5 shows the electrochemical values obtained with these curves. The calculated CR data show values ranging from  $2.44 \times 10^{-3}$  mmpy for Sample 1 to  $2.80 \times 10^{-3}$  mmpy for Sample 2, representing a ~16-fold increase compared to Sample 1.

**Table 5.** Electrochemical parameters obtained from Tafel curves.

	$E_{corr}$ [mV]	$i_{corr}$ [μA/cm <sup>2</sup> ]	$\beta_c$ [mV/dec]	$\beta_a$ [mV/dec]	$R_p$ [kΩ·cm <sup>2</sup> ]	CR [mmpy]
Sample 1	$-288 \pm 1$	$0.142 \pm 0.012$	$104 \pm 3$	$335 \pm 5$	$150 \pm 16$	$2.44 \times 10^{-3}$
Sample 2	$-346 \pm 3$	$0.210 \pm 0.032$	$121 \pm 4$	$338 \pm 2$	$113 \pm 12$	$2.80 \times 10^{-3}$

A more positive corrosion potential value can be observed for Sample 1 than for Sample 2. The corrosion current ( $i_{corr}$ ) is representative of the degree of oxidation of the alloy. A higher polarization resistance ( $R_p$ ) denotes that the alloy is more resistant to corrosion; thus, Sample 1 was more resistant to corrosion than Sample 2.

The Tafel slopes ( $\beta_a$  and  $\beta_c$ ) were obtained through an analysis of the curve plotted in an interval of  $\pm 250$  mV versus the open-circuit potential (OCP). Sample 1 showed a tendency toward passivation because it had a value of  $\beta_a$  greater than  $\beta_c$ , while Sample 2 presented a corrosion tendency because the anodic slope was lower than the cathodic slope.

The characteristics of the oxide layer formed on an alloy surface can be estimated by means of the impedance technique, also known as electrochemical impedance spectroscopy (EIS). The graphs obtained from the EIS tests are presented as Nyquist plots in Figure 6 and Bode plots in Figure 7.

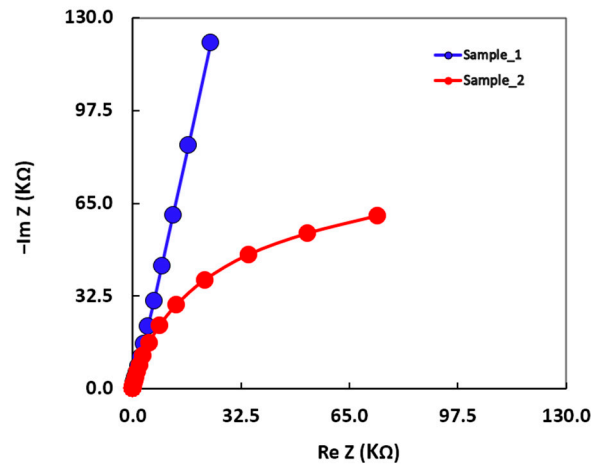


Figure 6. Nyquist diagrams for Sample 1 and Sample 2.

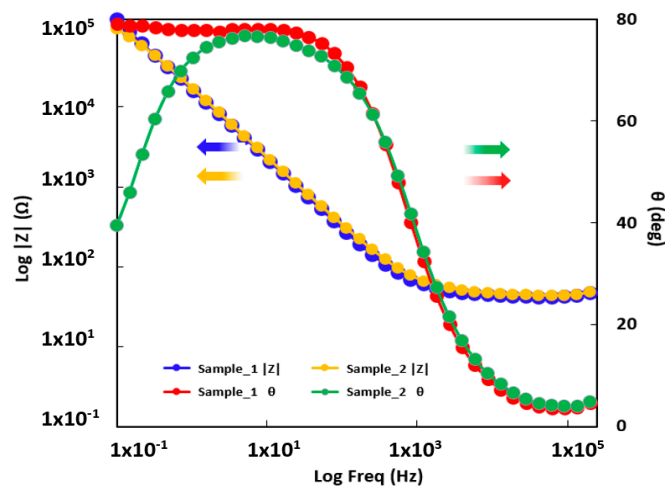


Figure 7. Bode diagrams for Sample 1 and Sample 2.

As can be observed in the Nyquist plots (see Figure 6), the radius of the semicircle for Sample 2 was smaller than that for Sample 1, indicating a low polarization resistance (a low corrosion resistance) for Sample 2.

In the Bode vs.  $|Z|$  plot (see Figure 7), a slight shift toward a higher value of the impedance module at the lowest frequency can be observed for Sample 1, indicating a slightly increased corrosion resistance of this alloy. In the Bode phase plots shown in Figure 6, a specific performance of the growth of a passive film can be observed for both alloys. This passive layer had a capacitive behavior with a phase angle approaching  $90^\circ$ . In the case of Sample 1, the higher phase angle was constant in a wide frequency band, a phenomenon related to an increase in the effective surface area.

After analyzing the shapes of the impedance diagrams, the experimental results could be fitted to an appropriate physical pattern consisting of an equivalent electrical circuit (EC). This circuit consists of several series or parallel configurations of resistors, capacitors, Warburg elements, etc. and provides the most relevant corrosion parameters of the substrate/electrolyte system. The equivalent circuit is similar to that proposed for  $Ti-xMo$ ,  $Al_xCoCrFeNi$  alloys,  $TiO_2$  nanofibers, and polymer electrolytes [45–47].

The equivalent circuit used to fit the experimental impedance data is presented in Figure 7, and the values of the corresponding elements are shown in Table 5.

Within the circuit presented in Figure 8, the ohmic resistance of the simulated seawater is labeled  $R_1$ , the resistance of the passive layer is labeled  $R_2$ , and the capacitance of the passive layer is represented as  $Q_2$ . As a consequence of the heterogeneous thin oxide film built up on the surface of the HEA alloys and the remarkable deviations of the Bode diagrams, it was required to replace the “ideal” capacitance by a constant-phase element (CPE) [48], the impedance of which is given [49] by  $Z = (j\omega)^{-n}Y^0$ , where  $j$  is an imaginary number ( $j^2 = -1$ ),  $\omega$  is the angular frequency ( $\text{rad}\cdot\text{s}^{-1}$ ),  $Y^0$  is the constant of the CPE [ $\text{S}(\text{s}\cdot\text{rad}^{-1})^n$ ],  $n$  is the power number denoting the drift from ideal performance,  $n = \alpha(\pi/2)$ , and  $\alpha$  is the constant-phase angle of the CPE (rad). Therefore, one of the parameters obtained when modeling the process is the ideality coefficient “ $n$ ”, in such a way that the answer of the real process is more similar to the ideal as the value of  $n$  gets closer to unity and, consequently, the surface is more uniform. Thus, for  $n = 1$ , the CPE element is reduced to a capacitor with a capacitance  $Y^0$  and, if  $n = 0$ , to a simple resistor [50].

$$\frac{1}{Z_{eq}} = \frac{1}{Z_{R_2}} + \frac{1}{Z_{Q_2}}. \quad (6)$$

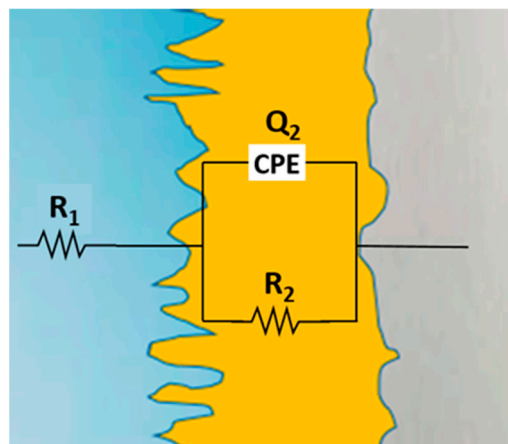


Figure 8. Equivalent circuit to fit the impedance data.

With the aim of estimating the total impedance of the equivalent circuit, we computed the admittance of the parallel arrangement ( $R_2Q_2$ ) as follows [51]:

Although a constant-phase element was used to fit the experimental results, the achieved value was considered as the capacity in the following equation:

$$\frac{1}{Z_{eq}} = \frac{1}{R_2} + j\omega C_2. \quad (7)$$

Multiplying by  $R_2$ , we get

$$Z_{eq} = \frac{R_2 - j(\omega C_2 R_2^2)}{1 + (\omega C_2 R_2)^2}. \quad (8)$$

Once the electrolyte ohmic resistance is added, the resulting impedance is

$$Z_{eq} = R_1 + \frac{R_2 - j(\omega C_2 R_2^2)}{1 + (\omega C_2 R_2)^2}. \quad (9)$$

$R_2$  was taken as the corrosion resistance of the analyzed HEAs. The  $R_2$  values calculated by fitting the experimental data with the simulated results of the corresponding equivalent circuit are given in Table 6.

**Table 6.** Fitted EIS parameters using the equivalent circuit model presented in Figure 8.

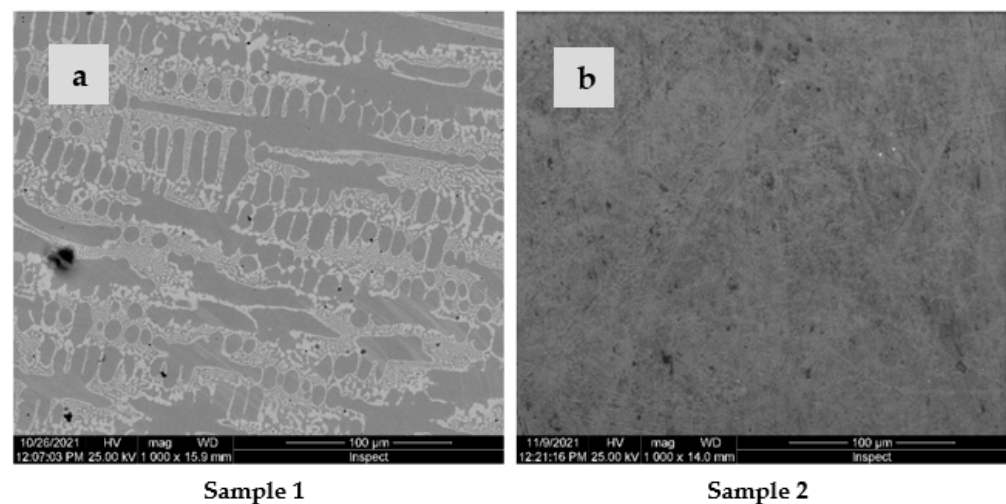
	Sample 1	Error %	Sample 2	Error %
$R_1$ ( $k\Omega \cdot \text{cm}^2$ )	42.70	0.96	45.09	1.22
$Q, Y^0$ ( $S \cdot S^n / \text{cm}^2$ )	$1.20 \times 10^{-5}$	1.23	$1.12 \times 10^{-5}$	1.72
$Q, n$	0.88	0.28	0.87	0.38
$R_2$ ( $k\Omega \cdot \text{cm}^2$ )	$2.57 \times 10^7$	5.40	$1.47 \times 10^5$	4.75
$\chi^2$	$1.18 \times 10^{-3}$		$1.87 \times 10^{-3}$	

This decrease in  $R_2$  (and, consequently, in corrosion resistance) when adding Zr was due to the fact that the passive film formed on the surface of the HEAs changed its properties as a result of this addition and became thicker ( $Y^0$  decreased with Zr addition).

It can be noted that the passive film resistance  $R_2$  decreased with the addition of Zr because of the increase in the number of defective spots in the film. Without Zr, the passive film formed on the surface of the alloy was more compact and protective (see values of  $Y^0$  in the Table 6).

Doping with oversized atoms, such as zirconium, obstructs the grain coarsening of HEA, creating a supersaturated solid solution. Tekin et al. [38] observed the in situ formation of  $\text{ZrO}_2$  through TEM analysis; in contrast, in our XRD, although we had the peaks of the phases, these were not effective because the volume fraction of  $\text{ZrO}_2$  was below the detection limit of XRD. The formation of  $\text{ZrO}_2$  explained the high corrosion rate of Sample 2 with zirconium in comparison to Sample 1 without zirconium.

After performing the corrosion tests, the surface was covered with a thin layer of oxide, which was subjected to SEM analyses, and the results are presented in Figure 9. The surface of both samples was covered with a very thin and transparent layer of oxide due to the chemical reactions during immersion in the corrosive solution. In the case of Sample 2 alloy, the oxide layer was thicker and further blurred the surface microstructure.

**Figure 9.** SEM image of the surface after performing the corrosion tests: (a) Sample 1 and (b) Sample 2.

On the surface of Sample 1, a dendritic microstructure under the oxide layer and some corrosion pits were visible.

#### 4. Conclusions

The effects of alloying with zirconium on the microstructure, elastic modulus, and corrosion properties of a high-entropy alloy, from the CoCrFeNiMo system, were investigated. A simulated corrosive solution (3.5% NaCl) was used to characterize the corrosion behavior of these materials using electrochemical techniques.

- A brittle fracture with a cleavage-like fracture plane could be observed for both alloys.

- The alloy without zirconium was more resistant to corrosion, with a very low corrosion rate ( $2.44 \times 10^{-3}$  mmpy in comparison with  $2.80 \times 10^{-3}$  mmpy for the sample with Zr).
- The resistance of the passive film decreased with the addition of Zr (from  $2.57 \times 10^7$  k $\Omega$ ·cm<sup>2</sup> to  $1.47 \times 10^5$  k $\Omega$ ·cm<sup>2</sup>) due to the increased number of defects points in the film.
- Doping with 0.71 wt.% Zr produced grain refinement and increased the hardness but did not increase the modulus of elasticity or corrosion resistance of the CoCrFeNiMo alloy.

**Author Contributions:** S.B.-G., writing—original draft preparation, investigation, and management; J.M.-R., conceptualization and validation; V.G., investigation, writing—review and editing, and financing; I.V., methodology, investigation, and data curation. All authors have read and agreed to the published version of the manuscript.

**Funding:** This work was supported by the Romanian National Authority for Scientific Research, CNDI-UEFISCDI, through project number PN-III-P2-2.1-PED-2019-3953, contract 514PED2020: “New ceramic layer composite material processed by laser techniques for corrosion and high temperature applications—LASCERHEA”, within PNCDI III, and by Cabildo de Gran Canaria, project number CABINFR2019-07, by the Spanish Ministry of Universities, and by European Union Maria Zambrano, project number SI-1821.

**Data Availability Statement:** For the data supporting reported results can be asked the authors.

**Conflicts of Interest:** The authors declare no conflict of interest.

## References

1. Yeh, J.W.; Chen, S.K.; Lin, S.J.; Gan, J.Y.; Chin, T.S.; Shun, T.T.; Tsau, C.H.; Chang, S.Y. Nanostructured high-entropy alloys with multiple principal elements: Novel alloy design concepts and outcomes. *Adv. Eng. Mater.* **2004**, *6*, 299–303. [[CrossRef](#)]
2. Cantor, B.; Chang, I.T.H.; Knight, P.; Vincent, A.J.B. Microstructural development in equiatomic multicomponent alloys. *Mater. Sci. Eng. A* **2004**, *375*, 213–218. [[CrossRef](#)]
3. Wang, X.; De Vecchis, R.R.; Li, C.; Zhang, H.; Hu, X.; Sridar, S.; Wang, Y.; Chen, W.; Xiong, W. Design metastability in high-entropy alloys by tailoring unstable fault energies. *Sci. Adv.* **2022**, *8*, 7333. [[CrossRef](#)]
4. Yeh, J.W. Recent progress in high-entropy alloys. *Eur. J. Control* **2006**, *31*, 633–648. [[CrossRef](#)]
5. Ye, Y.F.; Wang, Q.; Lu, J.; Liu, C.T.; Yang, Y. High-entropy alloy: Challenges and prospects. *Mater. Today* **2016**, *19*, 349–362. [[CrossRef](#)]
6. López Ríos, M.; Socorro Perdomo, P.P.; Voiculescu, I.; Geanta, V.; Crăciun, V.; Boerasu, I.; Mirza Rosca, J.C. Effects of nickel content on the microstructure, microhardness and corrosion behavior of high-entropy AlCoCrFeNi alloys. *Sci. Rep.* **2020**, *10*, 1–11. [[CrossRef](#)]
7. Tang, Z.; Huang, L.; He, W.; Liaw, P.K. Alloying and processing effects on the aqueous corrosion behavior of high-entropy alloys. *Entropy* **2014**, *16*, 895–911. [[CrossRef](#)]
8. Qiu, Y.; Gibson, M.A.; Fraser, H.L.; Birbilis, N. Corrosion characteristics of high entropy alloys. *Mater. Sci. Technol.* **2015**, *31*, 1235–1243. [[CrossRef](#)]
9. Voiculescu, I.; Geanta, V.; Stefanoiu, R.; Patrop, D.; Binchiciu, H. Influence of the chemical composition on the microstructure and microhardness of alcrfeconi high entropy alloy. *Rev. Chim.* **2013**, *64*, 1441–1444.
10. Geantă, V.; Voiculescu, I.; Istrate, B.; Vranceanu, D.M.; Ciocoiu, R.C.; Cotruț, C.M. The Influence of Chromium Content on the Structural and Mechanical Properties of AlCrFeCoNi High Entropy Alloys. *Int. J. Eng. Res. Afr.* **2018**, *37*, 23–28. [[CrossRef](#)]
11. Fang, W.; Yu, H.; Chang, R.; Zhang, X.; Ji, P.; Liu, B.; Li, J.; Qu, X.; Liu, Y.; Yin, F. Microstructure and mechanical properties of Cr-rich Co-Cr-Fe-Ni high entropy alloys designed by valence electron concentration. *Mater. Chem. Phys.* **2019**, *238*, 121897. [[CrossRef](#)]
12. Wei, D.; Li, X.; Jiang, J.; Heng, W.; Koizumi, Y.; Choi, W.M.; Lee, B.J.; Kim, H.S.; Kato, H.; Chiba, A. Novel Co-rich high performance twinning-induced plasticity (TWIP) and transformation-induced plasticity (TRIP) high-entropy alloys. *Scr. Mater.* **2019**, *165*, 39–43. [[CrossRef](#)]
13. Wei, D.; Li, X.; Heng, W.; Koizumi, Y.; He, F.; Choi, W.-M.; Lee, B.-J.; Kim, H.S.; Kato, H.; Chiba, A. Novel Co-rich high entropy alloys with superior tensile properties. *Mater. Res. Lett.* **2019**, *7*, 82–88. [[CrossRef](#)]
14. Coury, F.G.; Santana, D.; Guo, Y.; Copley, J.; Otani, L.; Fonseca, S.; Zepon, G.; Kiminami, C.; Kaufman, M.; Clarke, A. Design and in-situ characterization of a strong and ductile co-rich multicomponent alloy with transformation induced plasticity. *Scr. Mater.* **2019**, *173*, 70–74. [[CrossRef](#)]
15. Coury, F.G.; Zepon, G.; Bolfarini, C. Multi-principal element alloys from the CrCoNi family: Outlook and perspectives. *J. Mater. Res. Technol.* **2021**, *15*, 3461–3480. [[CrossRef](#)]
16. Wu, Z.; Guo, W.; Jin, K.; Poplawsky, J.D.; Gao, Y.; Bei, H. Enhanced strength and ductility of a tungsten-doped CoCrNi medium-entropy alloy. *J. Mater. Res.* **2018**, *33*, 3301–3309. [[CrossRef](#)]

17. Mavros, N.; Larimian, T.; Esquivel, J.; Gupta, R.K.; Contieri, R.; Borkar, T. Spark plasma sintering of low modulus titanium-niobium-tantalum-zirconium (TNTZ) alloy for biomedical applications. *Mater. Des.* **2019**, *183*, 108163. [[CrossRef](#)]
18. Wang, C.; Yu, J.; Yu, Y.; Zhao, Y.; Zhang, Y.; Han, X. Comparison of the corrosion and passivity behavior between CrMnFeCoNi and CrFeCoNi coatings prepared by argon arc cladding. *J. Mater. Res. Technol.* **2020**, *9*, 8482–8496. [[CrossRef](#)]
19. Fan, R.; Wang, L.; Zhao, L.; Wang, L.; Zhao, S.; Zhang, Y.; Cui, B. Synergistic effect of Nb and Mo alloying on the microstructure and mechanical properties of CoCrFeNi high entropy alloy. *Mater. Sci. Eng. A* **2022**, *829*, 142153. [[CrossRef](#)]
20. Wei, D.; Wang, L.; Zhang, Y.; Gong, W.; Tsuru, T.; Lobzenko, I.; Jiang, J.; Harjo, S.; Kawasaki, T.; Bae, J.W.; et al. Metalloid substitution elevates simultaneously the strength and ductility of face-centered-cubic high-entropy alloys. *Acta Mater.* **2022**, *225*, 117571. [[CrossRef](#)]
21. Wei, D.; Gong, W.; Tsuru, T.; Lobzenko, I.; Li, X.; Harjo, S.; Kawasaki, T.; Do, H.-S.; Bae, J.W.; Wagner, C.; et al. Si-addition contributes to overcoming the strength-ductility trade-off in high-entropy alloys. *Int. J. Plast.* **2022**, *159*, 103443. [[CrossRef](#)]
22. Lizárraga, R.; Li, X.; Wei, D.; Vitos, L.; Li, X. The effect of Si and Ge on the elastic properties and plastic deformation modes in high- and medium-entropy alloys. *Appl. Phys. Lett.* **2021**, *119*, 141904. [[CrossRef](#)]
23. Li, X.; Wei, D.; Vitos, L.; Lizárraga, R. Micro-mechanical properties of new alternative binders for cemented carbides: CoCrFeNiWx high-entropy alloys. *J. Alloys Compd.* **2020**, *820*, 153141. [[CrossRef](#)]
24. Rodriguez, A.A.; Tylczak, J.H.; Gao, M.C.; Jablonski, P.D.; Detrois, M.; Ziomek-Moroz, M.; Hawk, J.A. Effect of Molybdenum on the Corrosion Behavior of High-Entropy Alloys CoCrFeNi<sub>2</sub> and CoCrFeNi<sub>2</sub>Mo<sub>0.25</sub> under Sodium Chloride Aqueous Conditions. *Adv. Mater. Sci. Eng.* **2018**, *2018*, 3016304. [[CrossRef](#)]
25. Wei, D.; Anniyaer, A.; Koizumi, Y.; Aoyagi, K.; Nagasako, M.; Kato, H.; Chiba, A. On microstructural homogenization and mechanical properties optimization of biomedical Co-Cr-Mo alloy additively manufactured by using electron beam melting. *Addit. Manuf.* **2019**, *28*, 215–227. [[CrossRef](#)]
26. Wei, D.; Koizumi, Y.; Chiba, A.; Ueki, K.; Ueda, K.; Narushima, T.; Tsutsumi, Y.; Hanawa, T. Heterogeneous microstructures and corrosion resistance of biomedical Co-Cr-Mo alloy fabricated by electron beam melting (EBM). *Addit. Manuf.* **2018**, *24*, 103–114. [[CrossRef](#)]
27. Yan, X.; Cao, W.; Li, H. Biomedical Alloys and Physical Surface Modifications: A Mini-Review. *Materials* **2021**, *15*, 66. [[CrossRef](#)]
28. Zaman, H.A.; Sharif, S.; Idris, M.H.; Kamarudin, A. Metallic Biomaterials for Medical Implant Applications: A Review. *Appl. Mech. Mater.* **2015**, *735*, 19–25. [[CrossRef](#)]
29. Wei, C.; Luo, L.; Wu, Z.; Zhang, J.; Su, S.; Zhan, Y. New Zr-25Ti-xMo alloys for dental implant application: Properties characterization and surface analysis. *J. Mech. Behav. Biomed. Mater.* **2020**, *111*, 104017. [[CrossRef](#)]
30. Wei, D.; Li, X.; Schönecker, S.; Jiang, J.; Choi, W.M.; Lee, B.J.; Kim, H.S.; Chiba, A.; Kato, H. Development of strong and ductile metastable face-centered cubic single-phase high-entropy alloys. *Acta Mater.* **2019**, *181*, 318–330. [[CrossRef](#)]
31. Niu, Z.; Wang, Y.; Geng, C.; Xu, J.; Wang, Y. Microstructural evolution, mechanical and corrosion behaviors of as-annealed CoCrFeNiMox (x = 0, 0.2, 0.5, 0.8, 1) high entropy alloys. *J. Alloys Compd.* **2020**, *820*, 153273. [[CrossRef](#)]
32. Qiu, X. Microstructure and mechanical properties of CoCrFeNiMo high-entropy alloy coatings. *J. Mater. Res. Technol.* **2020**, *9*, 5127–5133. [[CrossRef](#)]
33. Liu, Y.; Xie, Y.; Cui, S.; Yi, Y.; Xing, X.; Wang, X.; Li, W. Effect of Mo Element on the Mechanical Properties and Tribological Responses of CoCrFeNiMox High-Entropy Alloys. *Metals* **2021**, *11*, 486. [[CrossRef](#)]
34. Sui, Q.; Wang, Z.; Wang, J.; Xu, S.; Liu, B.; Yuan, Q.; Zhao, F.; Gong, L.; Liu, J. Additive manufacturing of CoCrFeNiMo eutectic high entropy alloy: Microstructure and mechanical properties. *J. Alloys Compd.* **2022**, *913*, 165239. [[CrossRef](#)]
35. Geambazu, L.E.; Cotruț, C.M.; Miculescu, F.; Csaki, I. Mechanically alloyed CoCrFeNiMo<sub>0.85</sub> high-entropy alloy for corrosion resistance coatings. *Materials* **2021**, *14*, 3802. [[CrossRef](#)]
36. Karlsdottir, S.N.; Geambazu, L.E.; Csaki, I.; Thorhallsson, A.I.; Stefanioiu, R.; Magnus, F.; Cotrut, C. Phase Evolution and Microstructure Analysis of CoCrFeNiMo High-Entropy Alloy for Electro-Spark-Deposited Coatings for Geothermal Environment. *Coatings* **2019**, *9*, 406. [[CrossRef](#)]
37. Dong, Z.; Sergeev, D.; Dodge, M.F.; Fanicchia, F.; Müller, M.; Paul, S.; Dong, H. Microstructure and thermal analysis of metastable intermetallic phases in high-entropy alloy CoCrFeMo<sub>0.85</sub>Ni. *Materials* **2021**, *14*, 1073. [[CrossRef](#)]
38. Tekin, M.; Polat, G.; Kotan, H. An investigation of abnormal grain growth in Zr doped CoCrFeNi HEAs through in-situ formed oxide phases. *Intermetallics* **2022**, *146*, 107588. [[CrossRef](#)]
39. Chen, G.; Xiao, Y.; Ji, X.; Liang, X.; Hu, Y.; Cai, Z.; Liu, J.; Tong, Y. Effects of Zr content on the microstructure and performance of TiMoNbZrx high-entropy alloys. *Metals* **2021**, *11*, 1315. [[CrossRef](#)]
40. Shimizu, H.; Yuasa, M.; Miyamoto, H.; Edalati, K. Corrosion Behavior of Ultrafine-Grained CoCrFeMnNi. *Materials* **2022**, *15*, 1007. [[CrossRef](#)] [[PubMed](#)]
41. ASTM E3-11(2017); Standard Guide for Preparation of Metallographic Specimens. ASTM International: West Conshohocken, PA, USA, 2017.
42. International Organization for Standardization ISO 7438:2020 Metallic Materials—Bend Test. 2020. Available online: <https://www.iso.org/standard/72187.html> (accessed on 26 July 2022).
43. ISO 14577-1:2015; Metallic Materials—Instrumented Indentation Test for Hardness and Materials Parameters—Part 1: Test Method. ISO: Geneva, Switzerland, 2015.
44. Shun, T.T.; Chang, L.Y.; Shiu, M.H. Microstructure and mechanical properties of multiprincipal component CoCrFeNiMox alloys. *Mater. Charact.* **2012**, *70*, 63–67. [[CrossRef](#)]

45. Perdomo, P.P.S.; Suárez, N.R.F.; Verdú-Vázquez, A.; Rosca, J.C.M. Comparative EIS study of titanium-based materials in high corrosive environments. *Int. J. Surf. Sci. Eng.* **2021**, *15*, 152–164. [[CrossRef](#)]
46. Socorro-Perdomo, P.P.; Florido-Suárez, N.R.; Voiculescu, I.; Mirza-Rosca, J.C. Comparative eis study of alxcocrfeni alloys in ringer's solution for medical instruments. *Metals* **2021**, *11*, 928. [[CrossRef](#)]
47. Abd El-Lateef, H.M.; Khalaf, M.M.; Dao, V.D.; Mohamed, I.M.A. Electrochemical Impedance Investigation of Dye-Sensitized Solar Cells Based on Electrospun TiO<sub>2</sub> Nanofibers Photoanodes. *Materials* **2022**, *15*, 6175. [[CrossRef](#)] [[PubMed](#)]
48. Ibriş, N.; Mirza Rosca, J.C. EIS study of Ti and its alloys in biological media. *J. Electroanal. Chem.* **2002**, *526*, 53–62. [[CrossRef](#)]
49. Boukamp, B.A. A nonlinear least squares fit procedure for analysis of immittance data of electrochemical systems. *Solid State Ion.* **1986**, *20*, 31–44. [[CrossRef](#)]
50. Lasia, A. Electrochemical impedance spectroscopy and its applications. *Electrochem. Impedance Spectrosc. Its Appl.* **2014**, 9781461489, 1–367. [[CrossRef](#)]
51. Scully, J.; Silverman, D.; Kendig, M. *Electrochemical Impedance: Analysis and Interpretation*; ASTM International: West Conshohocken, PA, USA, 1993.

**Disclaimer/Publisher's Note:** The statements, opinions and data contained in all publications are solely those of the individual author(s) and contributor(s) and not of MDPI and/or the editor(s). MDPI and/or the editor(s) disclaim responsibility for any injury to people or property resulting from any ideas, methods, instructions or products referred to in the content.



---

3.2 *EIS study of doped high entropy alloy*

---

**TÍTULO :** “EIS Study of Doped High-Entropy Alloy”

---

**AUTORES:** Santiago Jose Brito-Garcia; Julia Claudia Mirza-Rosca;  
Cristina Jimenez-Marcos; Ionelia Voiculescu

---

**REVISTA:** Metals

---

**ÍNDICE DE  
IMPACTO:** 2.695

---

**CUARTIL:** Q2

---

**DOI:** 10.3390/met13050883

---

**ISSN:** 2075-4701

---

**EDITORIAL:** MDPI

---

**AÑO:** 2023

---

**VOLUMEN:** 13

---

**PÁGINAS:** 17

---



Article

# EIS Study of Doped High-Entropy Alloy

Santiago Jose Brito-Garcia <sup>1</sup>, Julia Claudia Mirza-Rosca <sup>1,2,\*</sup> , Cristina Jimenez-Marcos <sup>1</sup> and Ionelia Voiculescu <sup>3</sup> 

<sup>1</sup> Mechanical Engineering Department, University of Las Palmas de Gran Canaria, 3500 Las Palmas de Gran Canaria, Spain

<sup>2</sup> Materials Engineering, and Welding Department, Transilvania University of Brasov, 500036 Brasov, Romania

<sup>3</sup> Faculty of Industrial Engineering and Robotics, Politehnica University of Bucharest, 060042 Bucharest, Romania

\* Correspondence: julia.mirza@ulpgc.es

**Abstract:** The promising results obtained in the research of high-entropy alloys are increasingly encouraging new configurations of these alloys. Our research was conducted on the high-entropy CoCrFeMoNi alloy and the Ti-doped CoCrFeMoNi alloy. Electrochemical impedance spectroscopy (EIS) measurements were performed on samples with and without Ti-doped CoCrFeMoNi high-entropy alloys in order to evaluate the influence of voltage on their behavior in a simulated aggressive environment. The impedance spectra were measured between  $-1.0$  and  $+0.8$  V vs. SCE at various potential levels. Using an electrical equivalent circuit to match the experimental data, the impedance spectra were analyzed. The corresponding circuit that successfully fits the spectra has two time constants: the first one is for the attributes of the compact passive layer and the second one is for the features of the porous passive layer. The results show that doping CoCrFeMoNi alloy with 0.36 at.% Ti reduces the alloy's ability to resist corrosion, as the alloy can react more quickly to the surrounding environment and cause a decrease in the corrosion resistance of the alloy.

**Keywords:** high-entropy alloys; Ti doping; EIS; equivalent circuit; corrosion resistance



**Citation:** Brito-Garcia, S.J.; Mirza-Rosca, J.C.; Jimenez-Marcos, C.; Voiculescu, I. EIS Study of Doped High-Entropy Alloy. *Metals* **2023**, *13*, 883. <https://doi.org/10.3390/met13050883>

Academic Editor: Sundeep Mukherjee

Received: 27 March 2023

Revised: 28 April 2023

Accepted: 29 April 2023

Published: 2 May 2023



**Copyright:** © 2023 by the authors. Licensee MDPI, Basel, Switzerland. This article is an open access article distributed under the terms and conditions of the Creative Commons Attribution (CC BY) license (<https://creativecommons.org/licenses/by/4.0/>).

## 1. Introduction

High-entropy alloys (HEAs) are a new class of materials that have received a lot of attention recently due to their special qualities and promising applications in many areas [1–3]. HEAs are made up of multiple metallic elements, typically five or more, mixed together in roughly equal proportions. This results in a random atomic arrangement, which gives rise to exceptional properties, such as high strength, high ductility, excellent corrosion resistance, and high-temperature stability.

HEAs have gained widespread interest in the scientific community due to their potential to revolutionize the design of structural materials, particularly in aerospace [4], energy [5–8], and biomedical industries [9–12]. Researchers are exploring various aspects of HEAs, including synthesis, characterization, and mechanical behavior, to better understand their fundamental properties and optimize their performance.

In this field of high-entropy alloys, CoCrFeMoNi has been reported to have remarkable mechanical qualities, such as high strength and superior ductility, even at cryogenic temperatures [13]. In particular, the high-temperature strength and ductility of CoCrFeMoNi HEA make it a promising candidate for high-temperature structural applications [14], such as in gas turbines and nuclear reactors, and with Nb and different concentrations of Mo, has improved corrosion resistance of the load-bearing parts of marine equipment [15]. An ion sulfurizing technique was applied to CoCrFeMoNi HEA, and the tribological properties were improved greatly due to the fabrication of lubricant phases during sulfurization [13].

Doping refers to the intentional addition of small amounts of one element to another material in order to modify its properties [16]. When metals are used as dopants, they can have various effects on the material's properties, depending on the specific metal and the material being doped.

For example, doping metals such as titanium, vanadium, or chromium into steels can improve their mechanical properties, such as strength, ductility, and toughness [17–19]. This is because these metals can form strong carbides or nitrides, which act as strengthening agents and can also improve wear and corrosion resistance. Similarly, doping copper into aluminum [20] can improve its electrical conductivity, while doping aluminum into copper [21] can improve its strength and corrosion resistance. Doping with other metals such as magnesium, zinc, or nickel [22,23] can also modify the properties of aluminum alloys, depending on the specific application. Despite the fact that boriding has been studied particularly for steels in several areas, including morphology, thickness, performance, and kinetics, the boronization of HEAs is still in its early stages [24]. After the boronizing technique was used on several types of HEA, its effects on the materials' mechanical and tribological characteristics were examined. According to reports, boronization increased the surface hardness of high-entropy alloys by more than three times [25,26] and the wear resistance of HEA by twelve times [27]. Overall, Ti doping is a versatile strategy for modifying the properties of various materials [28], and it is an active area of research in many fields. It has been reported that, in coatings, Ti provides high wear and corrosion resistance and a low friction coefficient, depending on the uniformity, hardness, elastic modulus, and coating layer's thickness [29], thanks to its high hardness, good substrate adhesion, and inert structure [30]. Electrochemical impedance spectroscopy (EIS) is a powerful analytical technique used to study the behavior of electrochemical systems [31–33]. It involves the application of a low amplitude alternating current (AC) signal to the system and analyzing the voltage response that results. By controlling the frequency of the AC signal over a range of values, the technique allows the measurement of impedance as a function of frequency.

EIS can provide information about the electrical properties of the system, such as its resistance, capacitance, and inductance, as well as its electrochemical properties, such as the charge transfer resistance, double-layer capacitance, and diffusion coefficient [34]. The technique can also be used to study the kinetics and mechanisms of electrochemical reactions, the adsorption of species on the electrode surface, and the behavior of complex electrochemical systems. Its non-invasive and non-destructive nature, along with its ability to provide information about both the electrical and electrochemical properties of a system, make it a valuable tool for the characterization and understanding of electrochemical systems.

Thus, the purpose of the present study was to evaluate, using EIS, the influence of the potential on the behavior of samples without Ti and with Ti-doped CoCrFeMoNi high-entropy alloys in a simulated aggressive environment. There is no data available about this particular doped high-entropy alloy manufactured using the vacuum arc remelting technique.

## 2. Materials and Methods

### 2.1. Sample Preparation

Investigations were conducted on the high-entropy CoCrFeMoNi alloy (HEA) and on the Ti-doped CoCrFeMoNi alloy (HEATi). The samples were obtained by the ERAMET Laboratory at Politehnica University of Bucharest using an MRF ABJ 900 vacuum arc remelting (VAR) system. The laboratory took into account the potential losses from vaporization as well as the anticipated degree of chemical element incorporation during melting in order to design the metallic charge.

For Co, Cr, Fe, Mo, Ni, and Ti, high-purity raw materials with purity values of at least 99.7% were used. To attain sufficient homogeneity, the obtained alloys underwent 8 cycles of flipping and remelting in VAR equipment (4 times for each part).

The elemental information of the HEA and doped HEA was determined using energy dispersive X-ray analysis (EDS) using a Fei XL30 ESEM (MTM, Leuven, Belgium) scanning electron microscope equipped with EDAX Sapphire detector. The atomic composition (at%)

of the HEA is Co (21.52), Cr (23.58), Fe (21.84), Mo (12.98), and Ni (20.14); for the HEATi, it is Co (21.09), Cr (22.67), Fe (21.37), Mo (14.26), Ni (20.24), and Ti (0.36).

The resulting ingots, which were transversally cut for additional analysis, were rods about 10 centimeters long and 1 cm in diameter. The samples experienced a three-stage surface processing procedure in order to conduct assessments of structure, composition, and electrochemistry. They were first embedded in a cylinder made of phenolic resin (see Figure 1 hot-mounting step) and after that, polished with SiC abrasive papers with progressively finer grain sizes varying from 240 to 2000 grit. Immediately after, following a final polish with 0.1 m alpha alumina paste, they were washed with ultrasonic deionized water [35]. All the steps of the sample's preparation and the posterior tests are presented in Figure 1.

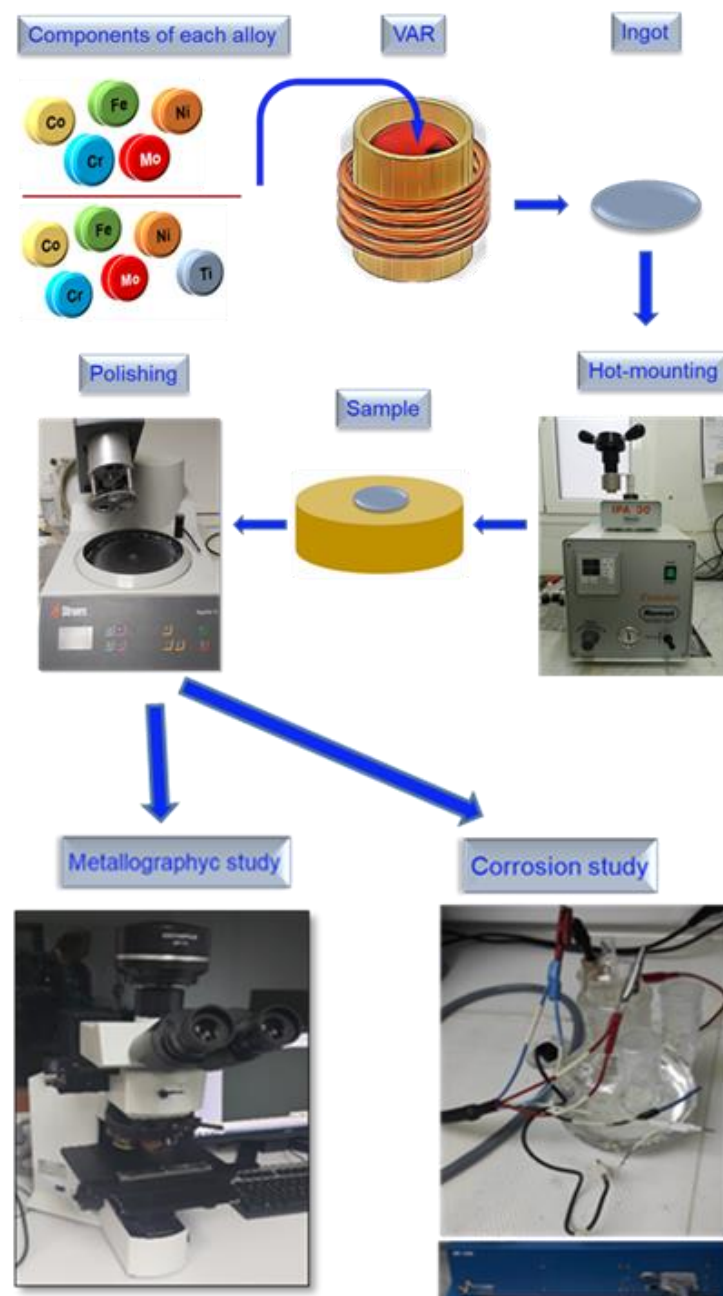


Figure 1. Samples' preparation and posterior tests.

## 2.2. Microstructural Characterization

An investigation was conducted on the microstructure of high-entropy alloys utilizing optical microscopy. To examine the surface of the samples, they were immersed in a 10% oxalic acid solution and subjected to a 5 V current for 5 to 25 s via electrochemical etching. The OLYMPUS PME 3 microscope (Olympus Corp., Tokyo, Japan) was used for optical observations of the etched surface. To investigate the microstructure and the segregation of chemical constituents of the samples, an energy-dispersive X-ray electron probe analyzer EDAX Sapphire (Ametek, Berwyn, PA, USA) was connected to an environmental scanning electron microscope (ESEM) type Fei XL30 ESEM outfitted with a LaB6 cathode (STS, North Billerica, MA, USA).

## 2.3. Electrochemical Measurements

### 2.3.1. Electrodes and Electrolyte

For all electrochemical measurements, a conventional electrochemical cell consisting of three electrodes, namely a working electrode, a reference electrode, and a counter electrode, was employed. The working electrode is formed by the alloy where the electrochemical reaction of interest takes place and is made of the material being studied (sample 1 and sample 2). The reference electrode is used as a reference point to measure the potential of the working electrode. It is a stable electrode with a well-known potential, a saturated calomel electrode (SCE). The counter electrode is an inert electrode that completes the circuit and balances the flow of electrons. It is made of a material that does not participate in the electrochemical reaction, in our case, platinum. During the electrochemical reaction, the electrolyte solution serves as the medium for the flow of current from the working electrode to the counter electrode. The potential difference between the working electrode and the reference electrode is measured to determine the electrochemical properties of the system. The three-electrode setup allows for precise measurements of the electrochemical behavior of the system, while the reference electrode ensures accurate potential measurements. To simulate the seawater environment, 3.5% NaCl solution was used.

### 2.3.2. Potentiodynamic Polarization

Potentiodynamic polarization is a technique used to study the corrosion behavior of a material. In this technique, the potential of the sample is varied over a range of values (starting at  $-1.5$  V till  $+0.8$  V vs. SCE) following the ASTM standard [36] while the current passing through the electrode is monitored. By plotting the resulting current as a function of the electrode potential, a polarization curve can be generated. Potentiodynamic polarization (PD) was performed with a scan rate of approx.  $300 \mu\text{V} / 1807.2 \text{ ms}$  [37].

### 2.3.3. Potentiostatic Electrochemical Impedance Spectroscopy (PEIS)

The PEIS experiment performed impedance tests into potentiostatic configuration in employing a sinusoidal round a potential  $E$  that was adjusted to a constant value (from  $-1.0$  V to  $+0.8$  V with a step of 200 mV). The potential was set to the fixed value for 30 min to wait for cell current stabilization [38], and during this period, no impedance measurements were undertaken. At each potential value, a scan from 100 kHz to 100 mHz with 6 points per decade was performed with a peak-to-peak amplitude of 10 mV.

### 3. Results and Discussions

#### 3.1. Microstructural Characterization

Optical images of the microstructure can be seen in Figure 2 for both analyzed alloys. These images show a dense microstructure that is free of cracks. In both alloys, the microstructure is dendritic, but the HEATi exhibited a tendency towards grain refinement.

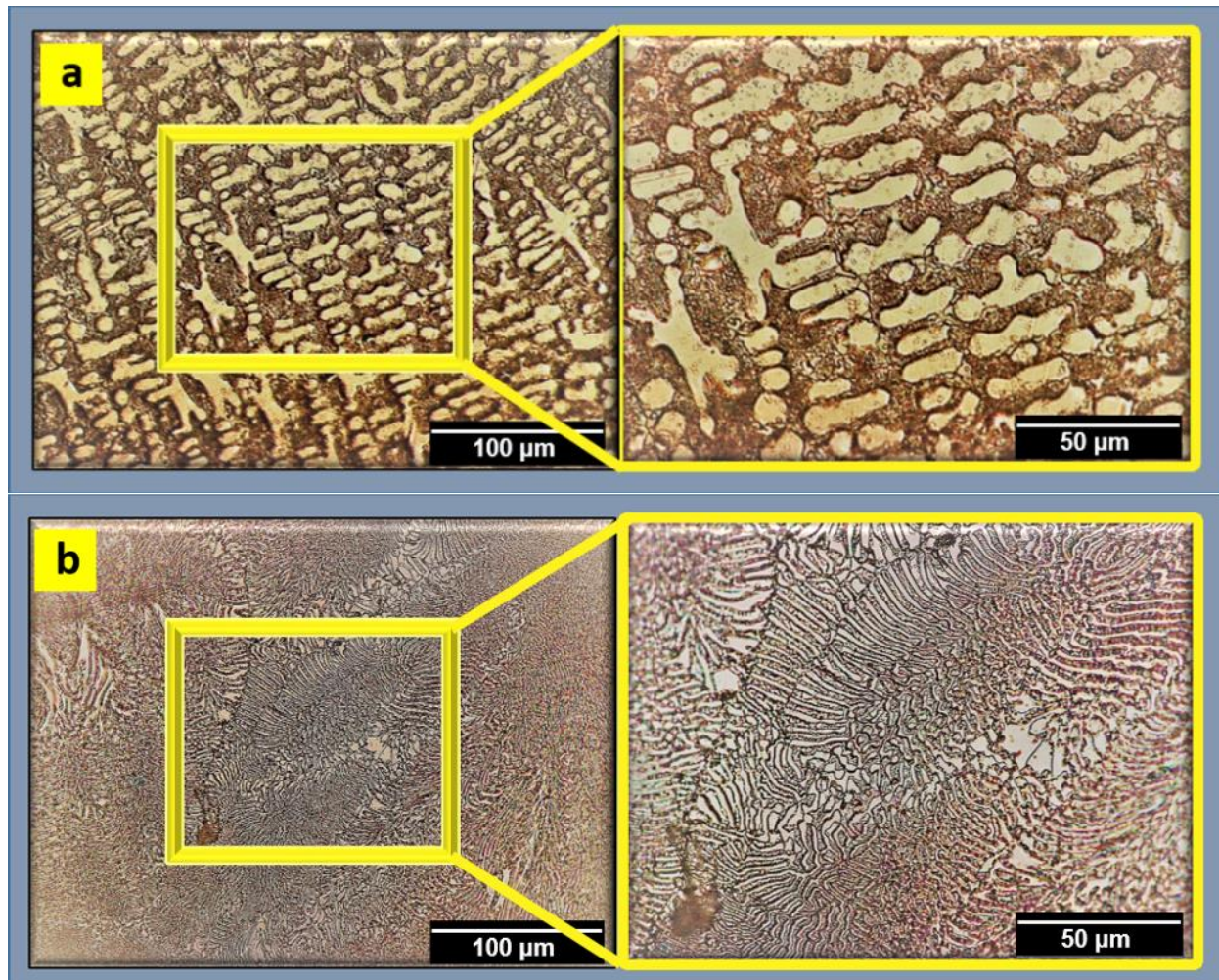


**Figure 2.** Metallographic structure of (a) HEA and (b) HEATi.

The SEM images of the samples with the corresponding maps and spectra are presented in Figure 3. It can be observed that the influence of iron increased as Ti doping was applied, and Ti showed a distinct difference in the two regions. The segregation ratios of cobalt, iron, and molybdenum all increased, but the segregation ratio of nickel decreased. This suggests that these elements precipitated less or generated fewer intermetallic complexes. Chromium's segregation ratio remained basically unaltered. It may be claimed that Ti doping increased the solubility limit of the solid phase for molybdenum and titanium while decreasing it for nickel, cobalt, and iron. Chromium remained mostly unaffected.

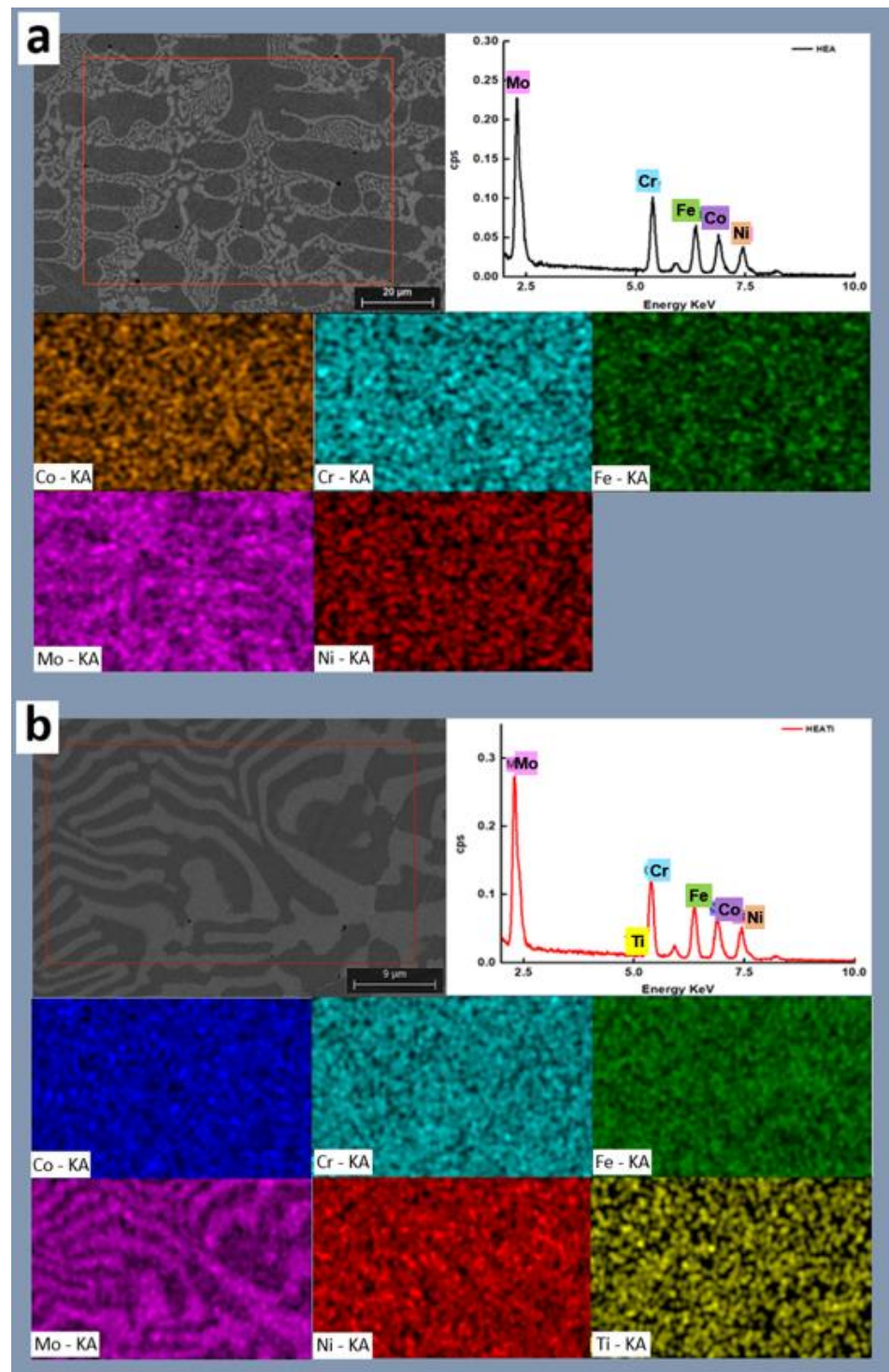


**Figure 3.** SEM micrographs and corresponding EDS maps and spectra for (a) HEA and (b) HEATi.

### 3.2. Electrochemical Measurements

The open circuit potential (OCP) is the potential difference between a metal electrode and a reference electrode when there is no current flowing between them. This potential is affected by the chemical environment surrounding the metal and can change over time as the metal corrodes. By measuring the OCP over time, the OCP diagram is obtained, which shows how the potential changes as a function of time. In a corrosive environment, the OCP of a metal can be affected by a number of factors, including the concentration of

dissolved oxygen, pH, and the presence of corrosive ions. The OCP diagrams of the HEA and HEATi are presented in Figure 4.

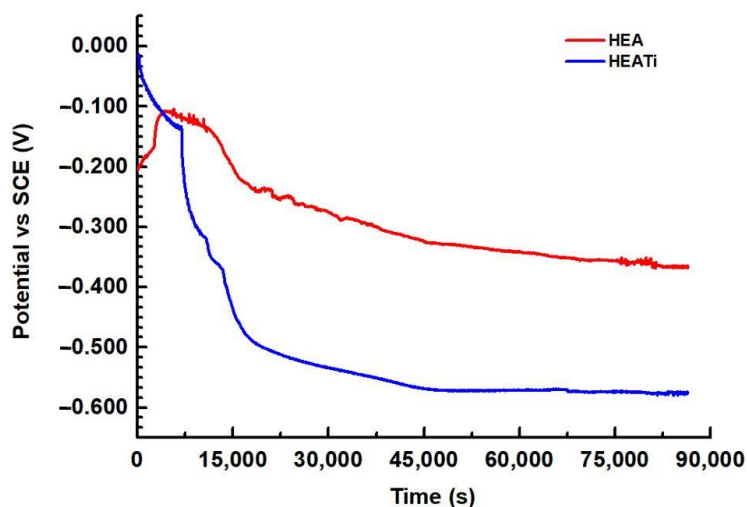


Figure 4. Open circuit potential for HEA and HEATi during 24 h in 3.5% NaCl.

It can be observed that for both samples the potential fluctuates and decreases over time; this suggests that the samples are susceptible to corrosion, and a corrosion product layer is formed on the surface. After about 12 h, the OCP diagram shows a stable potential over time, and this indicates that the alloys are not actively corroding and are, therefore, relatively resistant to corrosion in these conditions.

The shape of the polarization curve can provide important information about the electrochemical behavior of the metal. Figure 5 presents the polarization curves for the HEA and HEATi samples. The fit of the curves is based on the Stern and Geary equation, which states that the difference between the applied potential and the open circuit potential immediately correlates with the logarithm of the current measured during an electrochemical reaction [39]. The default positions for the fit are  $\pm 20$  mV and  $\pm 250$  mV around potential at zero current. Through these curves, the Tafel slopes were determined, being  $\beta_a = 775.9$  mV/decade and  $\beta_c = 119$  mV/decade for the HEA and  $\beta_a = 746.2$  mV/decade and  $\beta_c = 338.7$  mV/decade.

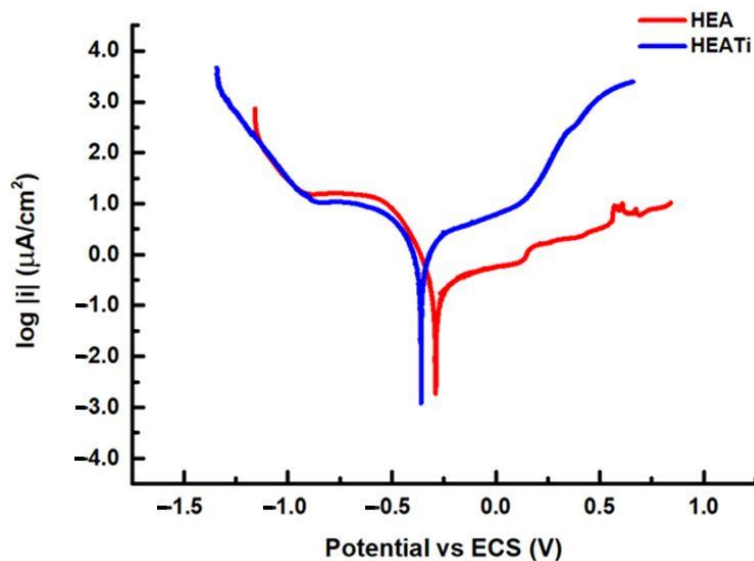


Figure 5. Linear polarization curves of the analyzed samples.

The Tafel slopes are used to calculate the Tafel constant  $B$ :

$$B = \frac{\beta_a \beta_c}{2.303(\beta_a + \beta_c)} \quad (1)$$

The corrosion rate is determined using the corresponding weight, density, and surface area.

The following equation is used to determine the corrosion rate (CR) [37]:

$$CR = \frac{I_{corr} K E_w}{\rho A} \quad (2)$$

The corrosion current is denoted as  $I_{corr}$  and is measured in amperes (A). The constant  $K$  is used to determine the units of the corrosion rate. The equivalent weight ( $E_w$ ) is measured in grams per equivalent, and the density ( $d$ ) is measured in grams per cubic centimeter ( $\text{g}/\text{cm}^3$ ). The sample area ( $A$ ) is measured in square centimeters ( $\text{cm}^2$ ).

The HEA sample has a corrosion rate of  $2.38 \times 10^{-3}$  mmpy, while for the HEATi, the corrosion rate is  $21.70 \times 10^{-3}$  mmpy, almost 10 times more. Similar results were obtained when the CoCrFeNiMo high-entropy alloy was doped with 0.48 at.% Zr [40], and it was reported that this doping produced grain refinement and increased the hardness but did not increase the modulus of elasticity or corrosion resistance of the CoCrFeNiMo high-entropy alloy.

The surface of the samples HEA and HEATi were examined using SEM/EDS methods after 24 h of immersion in a 3.5% NaCl corrosive solution. For each sample, EDS analysis was performed both on the dendrites and inter-dendritic areas.

The microstructure of sample LAS 1 (see Figure 6a) is composed of dendrites (Cr-, Co-, Fe-, and Ni-rich), surrounded by inter-dendritic zones (Mo-rich, 19.50–15.56 at% Mo). Measuring spots 1 to 4 are located on the dendrites, while spots 5 to 8 are located on the inter-dendritic areas. As a result of EDS analysis (see Figure 6b), small quantities of Na and Cl were observed on the sample's surface. The maximum quantity of Cl was measured only on the dendritic areas (0.05–0.14 at% Cl), while Na was present mainly on the inter-dendritic areas (0.28–0.73 at% Na).

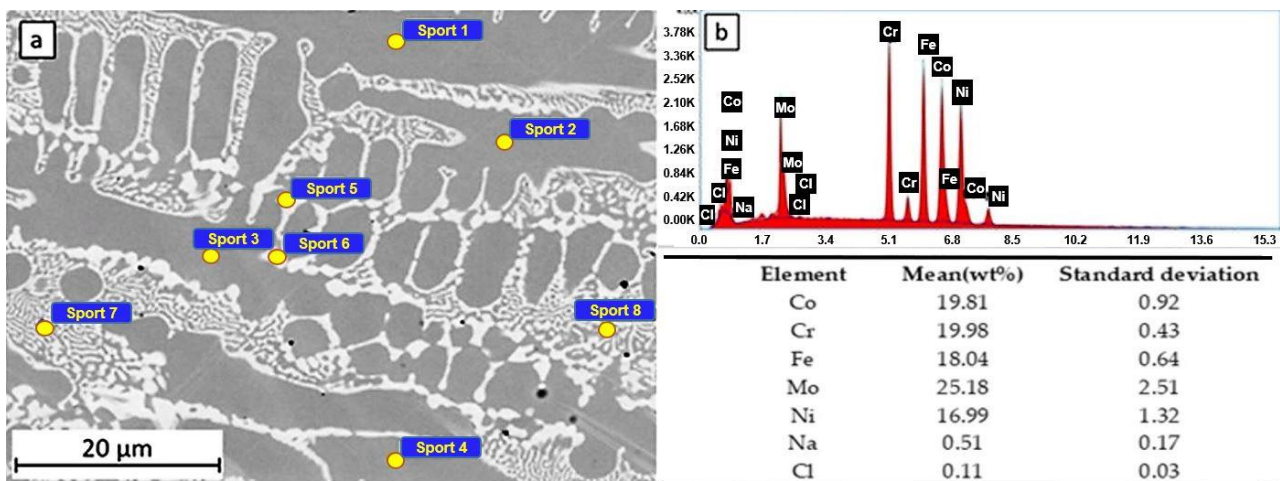


**Figure 6.** SEM observation (a) and EDS spectra and composition (b) of the HEA sample after 24 h of immersion in 3.5% NaCl.

In the SEM observations and EDS measurements of the HEATi samples (see Figure 7), Ti also appears in the chemical composition of the alloy, and in this case, the areas rich in Mo are the inter-dendritic ones (12.92–13.76 at% Mo). The Cl concentration was maximal

on these areas (0.13–0.15 at% Cl), while the maximal Na concentration (0.90 at%) was measured on an inter-dendritic zone.

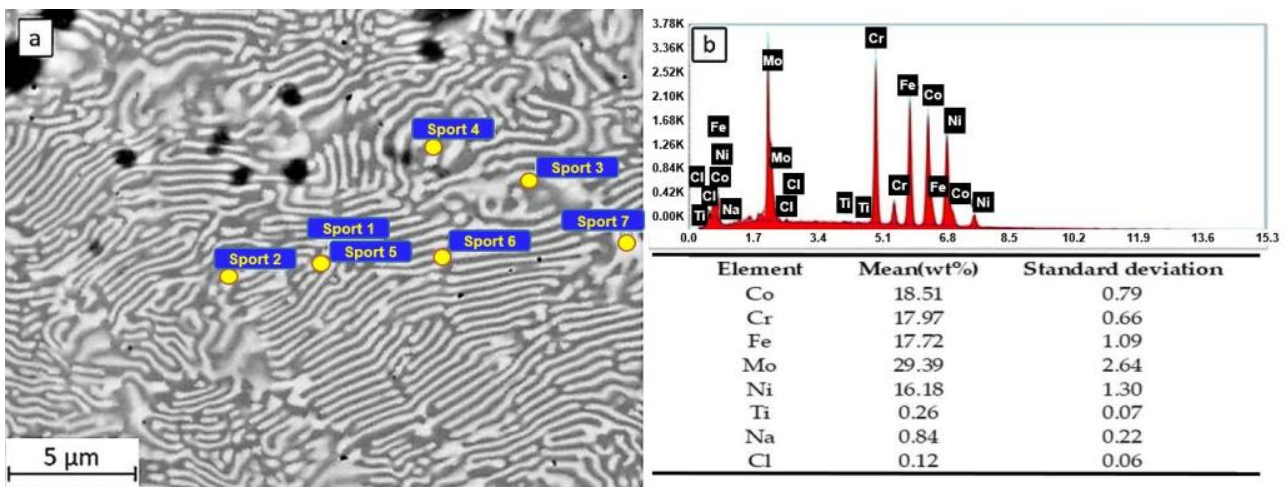
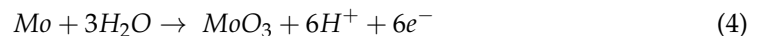
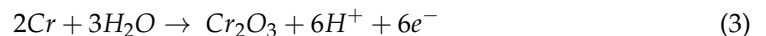


**Figure 7.** SEM observation (a) and EDS spectra and composition (b) of the HEATi sample after 24 h of immersion in 3.5% NaCl.

The XPS results [41] suggest that the passive film mainly consists of  $\text{Cr}_2\text{O}_3$  and  $\text{MoO}_3$ , according to the reactions [42]:



The impedance data were utilized to assess the behavior of the samples. When examining the Nyquist plots, it becomes evident that all samples exhibit three distinct regions. The first region corresponds to an area of low impedances at high frequencies, while the second region corresponds to an area of medium impedances with a ratio greater than that of the high-frequency region. Finally, the third region consists of a line of high impedances at low frequencies. This pattern clearly indicates that at least two frequency-dependent processes with different time constants are contributing to the feedback.

In the Nyquist plot of the HEATi (see Figure 8d), an inductive behavior can be observed at 400 mV. Inductance is a property of electrical circuits that describes the ability of a circuit to store energy in a magnetic field when an electric current flows through it. In electrochemical impedance spectroscopy (EIS), inductance is one of the three main components of impedance, along with resistance and capacitance.

In EIS measurements, inductance can have a significant effect on the data obtained. Inductance causes a phase shift between the applied AC voltage and the resulting AC, which can be observed in the phase angle of the impedance data. The magnitude of the inductance is also reflected in the frequency dependence of the impedance, with higher inductance leading to a greater deviation from the ideal behavior of a purely resistive or capacitive system. The Bode phase plot exhibits phase displacement in relation to frequency for distinct potentials versus the reference electrode. The presence of a solitary phase shift peak within the range of potentials between  $-1.0$  V and  $-0.2$  V suggests that any time constants tied to the corrosion process must be relatively close in frequency. As the potential increases, the maximum phase shifts systematically to lower frequencies. This change is a sign of increased polarization resistance and can take place without any shift in interfacial capacitance (see Figure 9a,c). It can be observed from the curves at 0.4 V, 0.6 V, and 0.8 V of the HEATi (see Figure 9d) that phase Z changes sharply in the low-frequency region, which means that the sample undergoes pitting corrosion (as can also be observed in Figure 5

when the potential exceeds about 0.25 V). The reason for pitting corrosion in the HEATi alloy can be explained by the preferential dissolution of iron ions into the electrolyte due to the increase in the Fe segregation ratio when the high-entropy alloy was doped with Ti. Due to the low stability of iron species compared to Cr, Mo, Ni, and Co substances, previous investigations [43,44] on stainless steels demonstrated that Fe was primarily prone to selective dissolution.

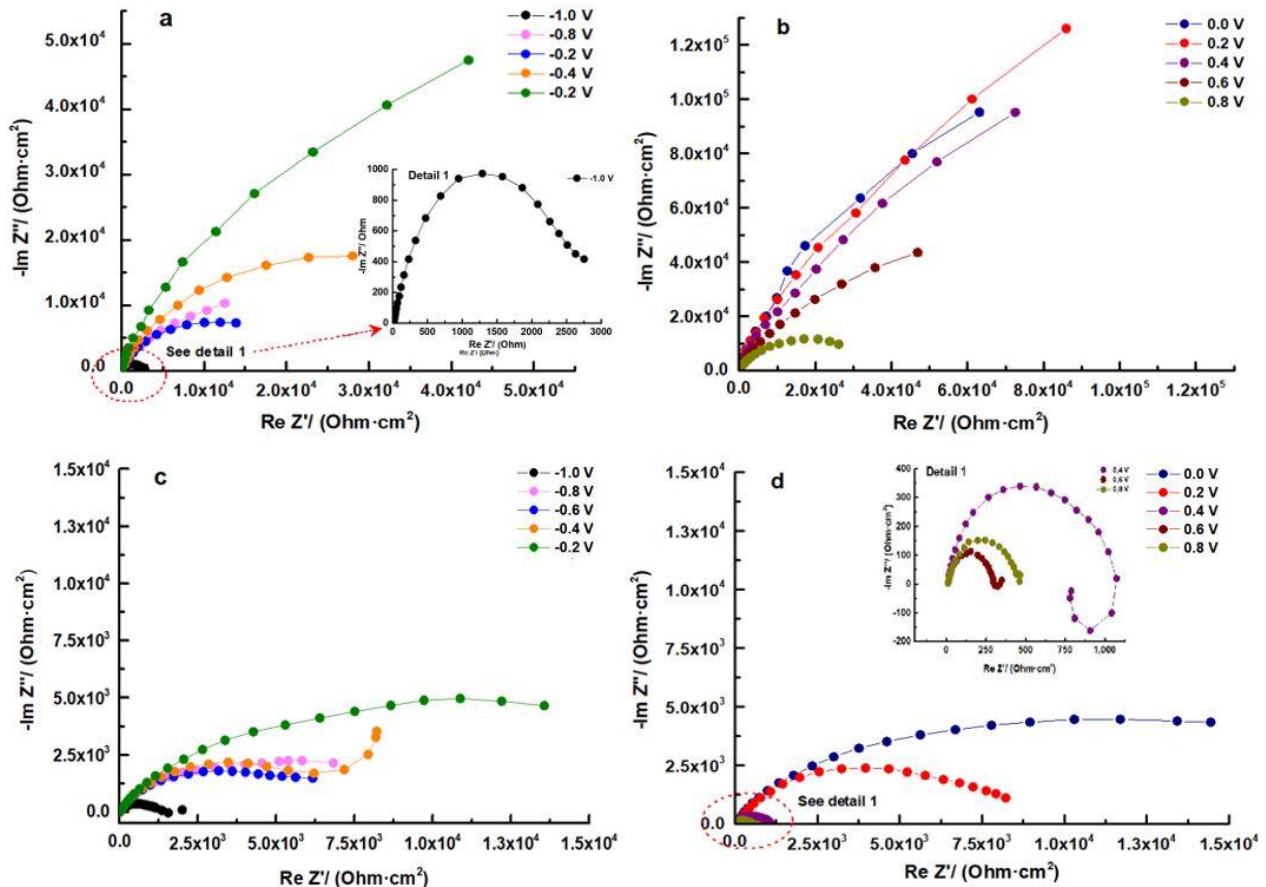


**Figure 8.** Nyquist plots for HEA (a,b) and for HEATi (c,d).

In the Bode–IZI plots (refer to Figure 10), the impedance spectra for both samples display overlapping curves at high and mid frequencies. There is a notable decline between  $-0.2$  and  $0.0$  V that persists throughout the duration of the experiment, with the film resistance being reduced by over 10 times for all samples. Within the potential range of  $0.0$  V to  $0.8$  V, the phase data demonstrate the emergence of a second, low-frequency phase peak. It is clear from this that the spectrum can be resolved into two nearly identical time constants, suggesting the presence of a two-step mechanism of the electrochemical reaction which occurs at the interface of the electrolyte/alloy.

The impedance of the low-frequency flat surface is related to the intrinsic characteristics of the film in the Bode–IZI graphs (see Figure 10). This low-frequency zone signifies the total resistance of the passive film, charge transfer resistance, and electrolyte resistance. Given that the last two resistances remain relatively constant for the same sample, any modifications in the low-frequency region can be attributed to alterations in the film, potentially resulting from the conductive pathways through it. The rise in low-frequency impedance with potential indicates a greater corrosion resistance of the layer formed on the HEA surface, with the HEA sample at  $0.2$  V displaying the highest corrosion resistance.

In Figure 8b and d, it can be observed that from  $0.2$  V to  $0.8$  V, a diffusion-controlled process becomes a significant component of total impedance. These findings indicate an ionic conductivity-controlled diffusion process for corrosion [45], with the transfer

resistance dominating film resistance. The pore-filling process in the external layer may be the cause of this inconsistent behavior.

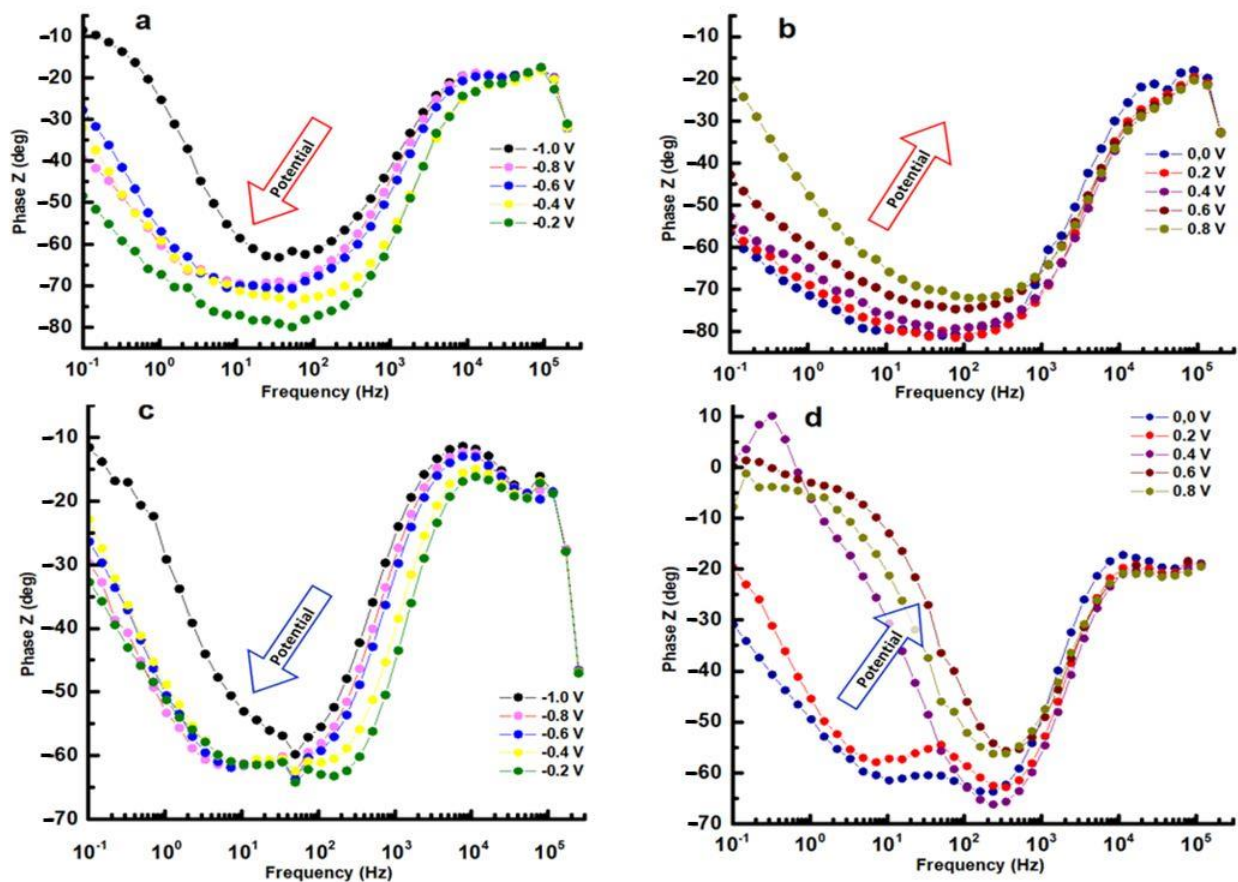


Figure 9. Bode phase for HEA (a,b) and for HEATi (c,d).

The selection of an appropriate equivalent circuit is critical for accurately fitting and interpreting EIS data. The equivalent circuit should be physically meaningful and relevant to the electrochemical system being studied, and it should be as simple as possible while still capturing the important features of the system because adding too many circuit elements can lead to overfitting, which can result in poor model predictions and difficulty in interpreting the fitted parameters. It should provide a good fit to the experimental data, and this can be evaluated by calculating the root mean square error.

The equivalent circuit that shows an appropriate balance between physical relevance and simplicity is represented in Figure 11 and was used to model the corrosion process parameters based on the impedance spectra visual data [46]. To compare the EIS data at all potentials, we did not use the inductance in the circuit because with inductance, only for one area of data (at 0.4V for the HEATi), the fit was better, with all the rest of the data being a good fit with the circuit from Figure 11.

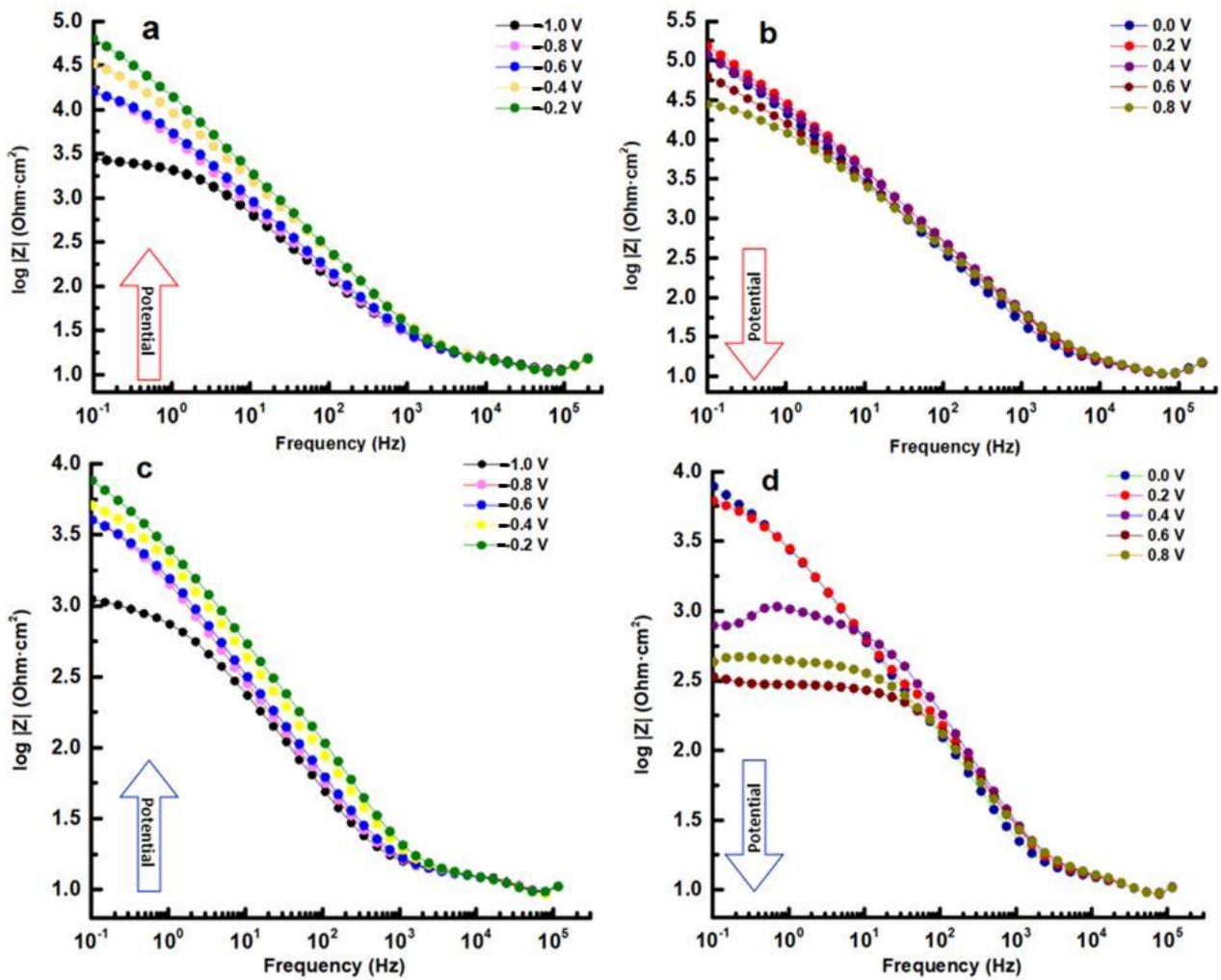


Figure 10. Bode-IZI for HEA (a,b) and for HEATi (c,d).

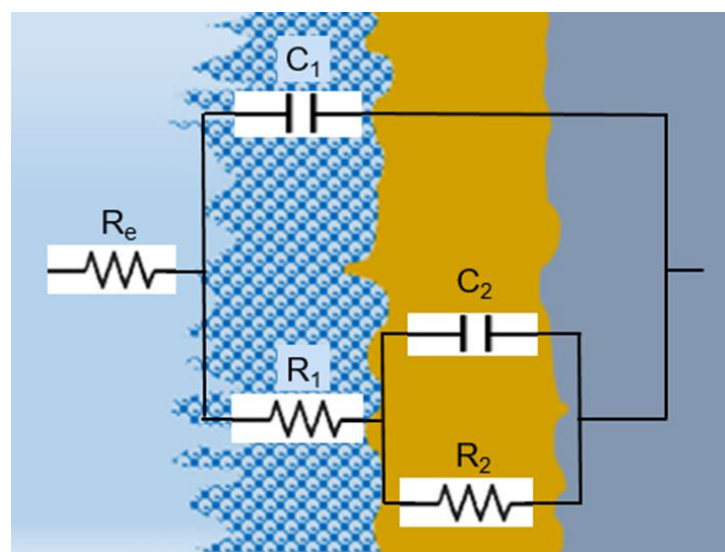


Figure 11. Electrical equivalent circuit used for fitting the experimental EIS data.

The impedance spectra were analyzed using ZSimpWin 3.6 software (Informer Technologies, Los Angeles, CA, USA), and the quality of the fit was evaluated by comparing the experimental data with the simulated data and calculating the chi-square value. A value

of chi-square around  $10^{-5}$  signifies a highly accurate fit with a minimal number of components [47]. All elements in the equivalent circuit were consistent with the data. As the diffusion stage became increasingly important at potentials higher than  $-200$  mV, a better fit was obtained employing an equivalent electrical circuit with two time constants, known as R(C(R(CR))). This circuit takes into consideration the properties of both the interior, compact layer ( $R_2$  is the charge transfer resistance, and  $C_2$  is the double layer capacitance) and the exterior, porous, passive layer (characterized by the resistance  $R_1$  and associated capacitance  $C_1$ ). A capacitor was used instead of a constant phase element in fitting [48] due to the homogeneous interface between the high-entropy alloy and the electrolyte.

For this circuit, the equivalent impedance is:

$$Z_{eq} = R_e + \frac{1}{j\omega C_1 + \frac{1}{R_1 + \frac{1}{\frac{1}{R_2} + j\omega C_2}}} \quad (5)$$

considering:

- R is equal to  $R_1$  plus  $R_2$ ;
- T is the product of  $\tau_1$  and  $\tau_2$ ;
- X is equal to  $\tau_1$  plus  $\tau_2$  plus  $C_1$  times  $R_2$ ;
- Y is equal to  $\tau_2$  times  $R_1$ ;
- $\tau_1$  represents the time constant of the porous layer in seconds;
- $\tau_2$  represents the time constant of the compact layer in seconds.

Basic computations yielded the following equation:

$$Z_{eq} = R_e + \frac{R - \omega^2 RT + \omega^2 XY}{(1 - \omega^2 T)^2 + \omega^2 R^2} + j\omega \frac{Y - RX - \omega^2 TY}{(1 - \omega^2 T)^2 + \omega^2 X^2} \quad (6)$$

The electrolyte resistance ( $R_e$ ) is influenced by the separation among the working and reference electrodes, which remained constant in all experiments. Meanwhile,  $R_1$  stands for the resistance of the pores in the passive film and is linked to the ion conduction within the structure of the passive layer, revealing the degree of protection against corrosion supplied by the passive film to the base alloy. On the other hand,  $R_2$  indicates the polarization resistance at the interface between the alloy and passive film, considering the electrolyte's ability to enter into the pores.

$R_2$  represents the corrosion resistance of the investigated alloys, and its values are presented in Figure 10 after fitting the experimental data with the simulated values using the equivalent circuit. It can be observed that at  $-1000$  mV, the  $R_2$  values of both samples are similar. However, as the potential increases,  $R_2$  also increases and reaches its maximum at  $-200$  mV.

The rise in  $R_2$ , which correlates with the increase in potential, is attributed to changes in the characteristics of the protective layer formed on the sample surface. Specifically, the layer becomes increasingly compact, as evidenced by the nearly 90-degree phase angle, and thicker, as seen in the decrease of capacity  $C_2$  with the increasing potential (refer to Figure 12). The HEA sample exhibits the highest  $R_2$  value, as indicated in Figure 12b.

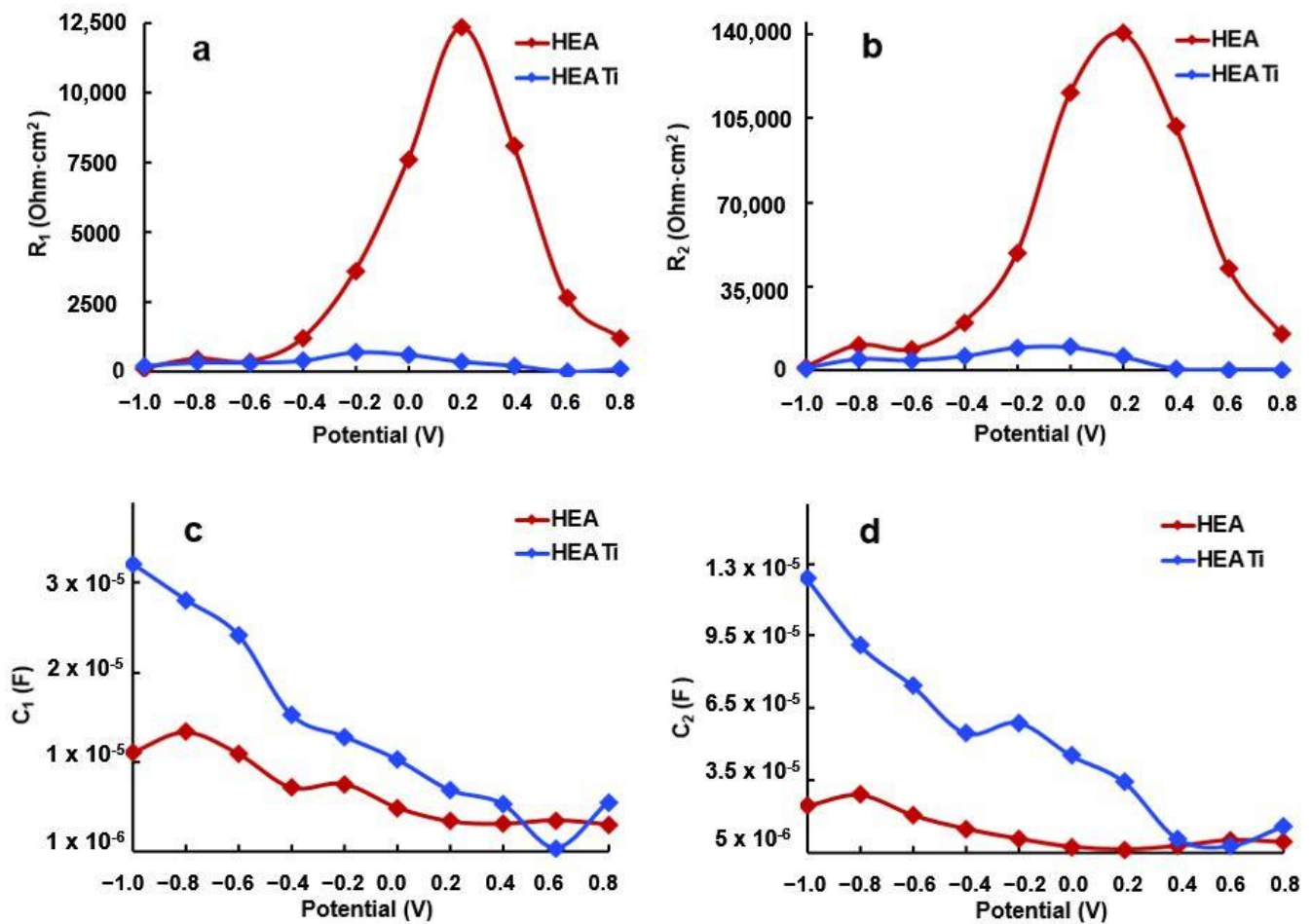


**Figure 12.** Evolution of  $R_1$  (a),  $R_2$  (b),  $C_1$  (c), and  $C_2$  (d) resulting from fitting of the experimental data of HEA and HEATi.

The increase in the  $R_2$  value up to  $-0.2$  V reflects the enhancement of the protective properties of the passive film as the potential rises. However, in the positive potential range, a decrease in  $C_1$  and  $C_2$  (refer to Figure 12c,d) indicates an increased irregularity and non-uniformity of the passive layer compared to the surface of the metal. It is a well-established fact that Ni and Cr are highly resistant to corrosion and form a robust passive film on the surface. During polarization,  $\text{Ni}(\text{OH})_2$  and  $\text{Cr}(\text{OH})_3$  are formed, leading to a uniform and compact passive film that effectively hinders  $\text{Cl}^-$  from coming into contact with the metal surface, thereby lowering the corrosion rate and enhancing the alloy's resistance to corrosion [48].

The decline in resistance at higher positive potentials can be attributed to the thinning and breakdown of the protective film on the sample surface. As the potential is shifted from  $-200$  mV to more positive values,  $R_2$  decreases, indicating a reduction in the corrosion resistance of the alloy. This phenomenon occurs because the protective film formed on the sample surface becomes more permeable, enabling the electrolyte's chloride ions to reach and attack the base metal. This is further evidenced by the decrease in  $C_2$ , which is a result of the pores' increased surface area that is exposed to the electrolyte, as shown in Figure 12d.

At positive potentials, the reduction in  $C_1$  and  $C_2$  suggests that the passive film becomes more uneven and rough compared to the underlying metal surface.

The discrepancies between the outcomes obtained from linear polarization and electrochemical impedance spectroscopy methods are attributed to inaccuracies arising from the initial current spike that distorted the polarization curve, leading to a shift of the zero-

current potential from the Ecorr equilibrium. However, the curve-fitting analysis of the EIS spectra, as demonstrated by the chi-square value, indicates a high degree of conformity between the experimental and simulated data.

#### 4. Conclusions

In the present work, CoCrFeMoNi HEAs and Ti-doped CoCrFeMoNi HEAs were prepared using vacuum arc remelting. Electrochemical impedance spectroscopy (EIS) measurements were performed on samples with and without Ti-doped CoCrFeMoNi high-entropy alloys in order to evaluate the influence of voltage on corrosion behavior in a simulated aggressive environment.

Above 0.25 V vs. SCE, the HEATi sample undergoes pitting corrosion. The reason for the pitting corrosion in the HEATi alloy can be explained by the preferential dissolution of iron ions into the electrolyte due to the increase in the Fe segregation ratio when the high-entropy alloy is doped with Ti.

Doping CoCrFeMoNi alloy with 0.36 at.% Ti reduce the alloy's ability to resist corrosion, as the alloy can react more quickly with the surrounding environment and cause a decrease in the corrosion resistance of the alloy.

**Author Contributions:** S.J.B.-G., writing—original draft preparation, investigation, and management; J.C.M.-R., conceptualization and validation; C.J.-M., investigation, writing—review and editing; I.V., methodology, investigation, and data curation. All authors have read and agreed to the published version of the manuscript.

**Funding:** This work was supported by the Romanian National Authority for Scientific Research, CNDE-UEFISCDI, through project number PN-III-P2-2.1-PED-2019-3953, contract 514PED2020: “New ceramic layer composite material processed by laser techniques for corrosion and high temperature applications—LASCERHEA”, within PNCDI III by Cabildo de Gran Canaria, project number CABINFR2019-07 and by the project ULPGC Excellence, funded by the Department of Economy, Knowledge and Employment of the Canary Islands Government.

**Data Availability Statement:** All data provided in the present manuscript are available to whom it may concern.

**Conflicts of Interest:** The authors declare no conflict of interest.

#### References

1. Chen, J.; Zhou, X.; Wang, W.; Liu, B.; Lv, Y.; Yang, W.; Xu, D.; Liu, Y. A review on fundamental of high entropy alloys with promising high-temperature properties. *J. Alloys Compd.* **2018**, *760*, 15–30. [\[CrossRef\]](#)
2. Miracle, D.B.; Senkov, O.N. A critical review of high entropy alloys and related concepts. *Acta Mater.* **2017**, *122*, 448–511. [\[CrossRef\]](#)
3. Alaneme, K.K.; Bodunrin, M.O.; Oke, S.R. Processing, alloy composition and phase transition effect on the mechanical and corrosion properties of high entropy alloys: A review. *J. Mater. Res. Technol.* **2016**, *5*, 384–393. [\[CrossRef\]](#)
4. Dada, M.; Popoola, P.; Adeosun, S.; Mathe, N. High Entropy Alloys for Aerospace Applications. *Aerodynamics. IntechOpen.* **2021**, 1–16. [\[CrossRef\]](#)
5. Yang, F.; Wang, J.; Zhang, Y.; Wu, Z.; Zhang, Z.; Zhao, F.; Huot, J.; Grobivc Novaković, J.; Novaković, N. Recent progress on the development of high entropy alloys (HEAs) for solid hydrogen storage: A review. *Int. J. Hydrogen Energy* **2022**, *47*, 11236–11249. [\[CrossRef\]](#)
6. Fu, M.; Ma, X.; Zhao, K.; Li, X.; Su, D. High-entropy materials for energy-related applications. *iScience* **2021**, *24*, 102177. [\[CrossRef\]](#)
7. Rios, M.L.; Baldevenites, V.L.; Voiculescu, I.; Rosca, J.M. AlCoCrFeNi High Entropy Alloys as Possible Nuclear Materials. *Microsc. Microanal.* **2020**, *26*, 406–407. [\[CrossRef\]](#)
8. Hussain, I.; Lamiel, C.; Ahmad, M.; Chen, Y.; Shuang, S.; Javed, M.S.; Yang, Y.; Zhang, K. High entropy alloys as electrode material for supercapacitors: A review. *J. Energy Storage* **2021**, *44*, 103405. [\[CrossRef\]](#)
9. Castro, D.; Jaeger, P.; Baptista, A.C.; Oliveira, J.P. An overview of high-entropy alloys as biomaterials. *Metals* **2021**, *11*, 648. [\[CrossRef\]](#)
10. López Ríos, M.; Socorro Perdomo, P.P.; Voiculescu, I.; Geanta, V.; Crăciun, V.; Boerasu, I.; Mirza Rosca, J.C. Effects of nickel content on the microstructure, microhardness and corrosion behavior of high-entropy AlCoCrFeNi alloys. *Sci. Rep.* **2020**, *10*, 1–11. [\[CrossRef\]](#)
11. Socorro-Perdomo, P.; Florido-Suarez, N.; Voiculescu, I.; Mirza-Rosca, J. Biocompatibility of New High-Entropy Alloys with Non-Cytotoxic Elements. *Microsc. Microanal.* **2021**, *27*, 1772–1774. [\[CrossRef\]](#)

12. Feng, J.; Tang, Y.; Liu, J.; Zhang, P.; Liu, C.; Wang, L. Bio-high entropy alloys: Progress, challenges, and opportunities. *Front. Bioeng. Biotechnol.* **2022**, *10*, 1–26. [[CrossRef](#)]
13. Cui, G.; Han, B.; Yang, Y.; Wang, Y.; Chunyang, H. Microstructure and tribological property of CoCrFeMoNi High entropy alloy treated by ion sulfurization. *J. Mater. Res. Technol.* **2020**, *9*, 2598–2609. [[CrossRef](#)]
14. Wang, Z.; Jin, J.; Zhang, G.H.; Fan, X.H.; Zhang, L. Effect of temperature on the passive film structure and corrosion performance of CoCrFeMoNi high-entropy alloy. *Corros. Sci.* **2022**, *208*, 110661. [[CrossRef](#)]
15. Zhou, Z.; Jiang, F.; Yang, F.; Yang, Y.; Liang, P. Novel laser cladding FeCoNiCrNb0.5Mox high-entropy alloy coatings with excellent corrosion resistance. *Mater. Lett.* **2023**, *335*, 133714. [[CrossRef](#)]
16. Zhang, J.; Tse, K.; Wong, M.; Zhang, Y.; Zhu, J. A brief review of co-doping. *Front. Phys.* **2016**, *11*, 117405. [[CrossRef](#)]
17. Wang, F.; Wang, S.; Chen, B.; Ma, W.; Jing, Q.; Zhang, X.; Ma, M.; Wang, Q.; Liu, R. Effect of Ti addition on the mechanical properties and microstructure of novel Al-rich low-density multi-principal-element alloys. *J. Alloys Compd.* **2022**, *891*, 162028. [[CrossRef](#)]
18. Wang, S.; Gao, Z.; Wu, G.; Mao, X. Titanium microalloying of steel: A review of its effects on processing, microstructure and mechanical properties. *Int. J. Miner. Metall. Mater.* **2022**, *29*, 645–661. [[CrossRef](#)]
19. Liu, Y.; Sun, Y.H.; Wu, H. Effect of chromium on the microstructure and hot ductility of Nb-microalloyed steel. *Int. J. Miner. Metall. Mater.* **2021**, *28*, 1011–1021. [[CrossRef](#)]
20. Lin, Y.J.; Huang, C.S.; Tsai, P.C.; Hsiao, Y.L.; Chen, C.Y.; Jou, J.H. Minor Copper-Doped Aluminum Alloy Enabling Long-Lifetime Organic Light-Emitting Diodes. *ACS Appl. Mater. Interfaces* **2022**, *14*, 55898–55904. [[CrossRef](#)]
21. Jing, J.; Gu, X.; Zhang, S.; Sun, J.; Chen, Y.; Sun, T. Doping of aluminum (Al) into copper sulfide (CuS) nanocrystals enhanced their solar spectral selectivity. *CrystEngComm* **2019**, *21*, 4969–4975. [[CrossRef](#)]
22. Missaghian, P. Oxidation of magnesium doped Al-surfaces. *KTH Skolan for Teknikvetenskap* **2020**, *1*, 1–33.
23. Meroueh, L.; Eagar, T.W.; Hart, D.P. Effects of Mg and Si Doping on Hydrogen Generation via Reduction of Aluminum Alloys in Water. *ACS Appl. Energy Mater.* **2020**, *3*, 1860–1868. [[CrossRef](#)]
24. Gunen, A.; Keddani, M.; Sunbul, S.E.; Icin, K.; Doleker, K.M.; Gok, M.S.; Dal, S.; Erdogan, A. Powder-pack boronizing of CoCrFeNiAl<sub>0.5</sub>Nb<sub>0.5</sub> HEA: Modeling of kinetics, microstructural, mechanical, and tribological characterizations. *J. Alloys Compd.* **2022**, *929*, 167310. [[CrossRef](#)]
25. Zhang, Y.; Wu, H.; Chen, Y.; Dong, J.; Yin, S.; Hua, K.; Wang, H. Characterization of the microstructure and self-lubrication properties of a AlCoCrFeNi<sub>2.1</sub> eutectic high-entropy alloy with powder-pack boronizing. *Mater. Charact.* **2022**, *191*, 112118. [[CrossRef](#)]
26. Wu, Y.H.; Yang, H.J.; Guo, R.P.; Wang, X.J.; Shi, X.H.; Liaw, P.K.; Qiao, J.W. Tribological behavior of boronized Al<sub>0.1</sub>CoCrFeNi high-entropy alloys under dry and lubricated conditions. *Wear* **2020**, *460–461*, 203452. [[CrossRef](#)]
27. Hou, J.; Zhang, M.; Yang, H.; Qiao, J.; Wu, Y. Surface strengthening in Al<sub>0.25</sub>CoCrFeNi high-entropy alloy by boronizing. *Mater. Lett.* **2019**, *238*, 258–260. [[CrossRef](#)]
28. Qi, W.; Wang, W.; Yang, X.; Zhang, G.; Ye, W.; Su, Y.; Li, Y.; Chen, S. Effects of Al and Ti co-doping on the strength-ductility-corrosion resistance of CoCrFeNi-AlTi high-entropy alloys. *J. Alloys Compd.* **2022**, *925*, 166751. [[CrossRef](#)]
29. Kurt, B.; Günen, A.; Kanca, Y.; Koç, V.; Gök, M.S.; Kırar, E.; Askerov, K. Properties and Tribologic Behavior of Titanium Carbide Coatings on AISI D2 Steel Deposited by Thermoreactive Diffusion. *JOM* **2018**, *70*, 2650–2659. [[CrossRef](#)]
30. Günen, A.; Soyulu, B.; Karakaş, Ö. Titanium carbide coating to improve surface characteristic, wear and corrosion resistance of spherical graphite cast irons. *Surf. Coatings Technol.* **2022**, *437*, 128280. [[CrossRef](#)]
31. Mareci, D.; Ungureanu, G.; Aelenei, N.; Chelariu, R.; Rosca, J.C.M. EIS diagnosis of some dental alloys in artificial saliva. *Environ. Eng. Manag. J.* **2007**, *6*, 313–317. [[CrossRef](#)]
32. Socorro-Perdomo, P.P.; Florido-Suárez, N.R.; Mirza-Rosca, J.C.; Saceleanu, M.V. EIS Characterization of Ti Alloys in Relation to Alloying Additions of Ta. *Materials* **2022**, *15*, 476. [[CrossRef](#)] [[PubMed](#)]
33. Perdomo, P.P.S.; Suárez, N.R.F.; Verdú-Vázquez, A.; Rosca, J.C.M. Comparative EIS study of titanium-based materials in high corrosive environments. *Int. J. Surf. Sci. Eng.* **2021**, *15*, 152–164. [[CrossRef](#)]
34. González, J.E.G.; Mirza-Rosca, J.C. Study of the corrosion behavior of titanium and some of its alloys for biomedical and dental implant applications. *J. Electroanal. Chem.* **1999**, *471*, 109–115. [[CrossRef](#)]
35. ASTM E3-11; Standard Guide for Preparation of Metallographic Specimens. ASTM International: West Conshohocken, PA, USA, 2017.
36. Material, C.; Databases, P. Standard Reference Test Method for Making Potentiostatic and Potentiodynamic Anodic. *Annu. B. ASTM Stand.* **2004**, *94*, 1–12.
37. ASTM-Standards Standard practice for calculation of corrosion rates and related information from electrochemical measurements. *Astm G 102-89* **1999**, *89*, 1–7.
38. ISO 16773-1-4:2016; Electrochemical Impedance Spectroscopy (EIS) on Coated and Uncoated Metallic Specimens. International Organization for Standardization: Geneva, Switzerland, 2016.
39. Stern, M.; Geary, A.L. Electrochemical Polarization: I. A Theoretical Analysis of the Shape of Polarization Curves. *J. Electrochem. Soc.* **1957**, *104*, 56. [[CrossRef](#)]
40. Brito-Garcia, S.; Mirza-Rosca, J.; Geanta, V.; Voiculescu, I. Mechanical and Corrosion Behavior of Zr-Doped High-Entropy Alloy from CoCrFeMoNi System. *Materials* **2023**, *16*, 1832. [[CrossRef](#)]

41. Wang, W.; Wang, J.; Sun, Z.; Li, J.; Li, L.; Song, X.; Wen, X.; Xie, L.; Yang, X. Effect of Mo and aging temperature on corrosion behavior of  $(\text{CoCrFeNi})_{100-x}\text{Mo}_x$  high-entropy alloys. *J. Alloys Compd.* **2020**, *812*, 152139. [[CrossRef](#)]
42. Pourbaix, M.; Zhang, H.; Pourbaix, A. Presentation of an Atlas of chemical and electrochemical equilibria in the presence of a gaseous phase. *Mater. Sci. Forum* **1997**, *251–254*, 143–148. [[CrossRef](#)]
43. Wang, Z.; Feng, Z.; Zhang, L. Effect of high temperature on the corrosion behavior and passive film composition of 316 L stainless steel in high H<sub>2</sub>S-containing environments. *Corros. Sci.* **2020**, *174*, 108844. [[CrossRef](#)]
44. Wang, Z.; Zhang, L.; Zhang, Z.; Lu, M. Combined effect of pH and H<sub>2</sub>S on the structure of passive film formed on type 316L stainless steel. *Appl. Surf. Sci.* **2018**, *458*, 686–699. [[CrossRef](#)]
45. Scully, R.; Silverman, D.C.; Kendig, M. *Electrochemical Impedance: Analysis and Interpretation*; ASTM: Philadelphia, PA, USA, 1993. [[CrossRef](#)]
46. Lutton, K.; Han, J.; Ha, H.M.; Sur, D.; Romanovskaia, E.; Scully, J.R. Passivation of Ni-Cr and Ni-Cr-Mo Alloys in Low and High pH Sulfate Solutions. *J. Electrochem. Soc.* **2023**, *170*, 021507. [[CrossRef](#)]
47. Boukamp, B.A. A nonlinear least squares fit procedure for analysis of impedance data of electrochemical systems. *Solid State Ion.* **1986**, *20*, 31–44. [[CrossRef](#)]
48. Wang, Z.; Zhang, G.-H.; Fan, X.-H.; Jin, J.; Zhang, L.; Du, Y.-X. Corrosion behavior and surface characterization of an equiatomic CoCrFeMoNi high-entropy alloy under various pH conditions. *J. Alloys Compd.* **2022**, *900*, 163432. [[CrossRef](#)]

**Disclaimer/Publisher’s Note:** The statements, opinions and data contained in all publications are solely those of the individual author(s) and contributor(s) and not of MDPI and/or the editor(s). MDPI and/or the editor(s) disclaim responsibility for any injury to people or property resulting from any ideas, methods, instructions or products referred to in the content.





---

3.3 *Impact of Ti doping on the microstructure and mechanical properties of CoCrFeMoNi high entropy alloy*

---

**TÍTULO :** “Impact of Ti Doping on the Microstructure and Mechanical Properties of CoCrFeMoNi High-Entropy Alloy”

---

**AUTORES:** Santiago Jose Brito-Garcia, Julia Claudia Mirza-Rosca, Cristina Jimenez-Marcos y Ionelia Voiculescu

---

**REVISTA:** Metals

---

**ÍNDICE DE IMPACTO:** 2.695

---

**CUARTIL:** Q2

---

**DOI:** 10.3390/met13050854

---

**ISSN:** 2075-4701

---

**EDITORIAL:** MDPI

---

**MES Y AÑO:** 04/2023

---

**VOLUMEN:** 13

---

**PÁGINAS:** 13

---



## Article

# Impact of Ti Doping on the Microstructure and Mechanical Properties of CoCrFeMoNi High-Entropy Alloy

Santiago Jose Brito-Garcia <sup>1</sup>, Julia Claudia Mirza-Rosca <sup>1,2,\*</sup> , Cristina Jimenez-Marcos <sup>1</sup> and Ionelia Voiculescu <sup>3</sup> 

<sup>1</sup> Mechanical Engineering Department, University of Las Palmas de Gran Canaria, 35001 Las Palmas de Gran Canaria, Spain

<sup>2</sup> Materials Engineering, and Welding Department, Transilvania University of Brasov, 500036 Brasov, Romania

<sup>3</sup> Faculty of Industrial Engineering and Robotics, Politehnica University of Bucharest, 060042 Bucharest, Romania

\* Correspondence: julia.mirza@ulpgc.es

**Abstract:** The design principle of high-entropy alloys is to mix many chemical elements in equal or nearly equal proportions to create new alloys with unique and special properties such as high strength, ductility and corrosion resistance. Some properties of high-entropy alloys can be adjusted via introducing new doping elements, which are selected according to working conditions. The high-entropy alloy CoCrFeMoNi was examined to determine the impact of Ti doping on its microstructure, microhardness and elastic modulus. Microstructure analysis revealed a core structure consisting of both face-centered cubic (FCC) and body-centered cubic (BCC) phases, along with the formation of a Laves phase. The addition of Ti made the alloy grains finer and reduced the Mo concentration difference between the interdendritic and dendritic regions. As a result of Ti doping, the microhardness of the alloy increased from 369 HV 0.2 to 451 HV 0.2. Ti doping produced a doubling of the breaking strength value, although no significant changes were observed in the elastic modulus of the CoCrFeMoNi alloy.

**Keywords:** high entropy alloys; Ti-doping; microstructure; microhardness; three-point bending



**Citation:** Brito-Garcia, S.J.; Mirza-Rosca, J.C.; Jimenez-Marcos, C.; Voiculescu, I. Impact of Ti Doping on the Microstructure and Mechanical Properties of CoCrFeMoNi High-Entropy Alloy. *Metals* **2023**, *13*, 854. <https://doi.org/10.3390/met13050854>

Academic Editors: Robert Bidulský and Jana Bidulská

Received: 30 March 2023

Revised: 22 April 2023

Accepted: 24 April 2023

Published: 27 April 2023



**Copyright:** © 2023 by the authors. Licensee MDPI, Basel, Switzerland. This article is an open access article distributed under the terms and conditions of the Creative Commons Attribution (CC BY) license (<https://creativecommons.org/licenses/by/4.0/>).

## 1. Introduction

Metallic alloys that contain at least five distinct elements in approximately equal proportions are known as high-entropy alloys (HEAs). HEAs contain numerous principal elements in high concentrations, unlike traditional alloys, which usually contain one or two main elements with minor amounts of other elements added to enhance certain properties. The high-entropy concept was introduced in 2004 by two different groups [1,2] and since then, a variety of HEAs have been developed and studied, including alloys containing elements such as nickel [3,4], aluminum [5,6], titanium [7,8] and molybdenum [9]. One of the defining characteristics of HEAs is their high configurational entropy, which is a measure of the degree of disorder in the arrangement of atoms within a material. Some potential applications of HEAs include high-temperature materials for use in jet engines or nuclear reactors [9,10], lightweight alloys for use in the aerospace or automotive industries [11,12] and corrosion-resistant coatings for use in harsh environments [13–15]. Recently, high-entropy alloys have been created for potential use in extremely effective electrochemical devices that efficiently and sustainably transform fuel energy into electricity [16]. While HEAs are a relatively new class of materials, research in this area is rapidly expanding, and there is significant interest in exploring their potential properties and applications.

The field of high-entropy alloys has found that CoCrFeMoNi possesses exceptional mechanical properties, including impressive strength and flexibility even when exposed to extremely low temperatures [17,18]. These properties, particularly its high-temperature strength and ductility, make CoCrFeMoNi a promising material for use in high-temperature structures such as gas turbines and nuclear reactors [19]. Additionally, adding Nb and

varying concentrations of Mo [20] has been found to enhance the corrosion resistance of load-bearing parts used in marine equipment.

Doping of high-entropy alloys (HEAs) refers to the intentional addition of other chemical elements, in small amounts [21], to the base alloy composition which can influence the physical and mechanical properties of the alloy. Overall, the effect of doping on HEAs depends on the specific elements added, their concentration and the intended application of the alloy. Through carefully adapting the doping strategy, HEAs with properties suitable for certain operating conditions can be obtained.

Ti doping has been extensively studied in a wide range of materials, including semiconductors, ceramics and metals. Ti doping is commonly used to modify the electronic properties of semiconductors. For example, Ti doping in silicon (Si) can lead to an increase in the number of free electrons, which can enhance the electrical conductivity and make Si more suitable for applications such as solar cells and microelectronics [22]. Similarly, Ti doping in gallium nitride (GaN) can enhance the electrical conductivity and improve the performance of GaN-based devices (LEDs) and the mobility of electrons in transistors (HEMTs) [23,24].

Ti doping can also alter the mechanical and chemical properties of ceramics. For instance, Ti doping in alumina ( $\text{Al}_2\text{O}_3$ ) can enhance its hardness, fracture toughness and wear resistance, making it suitable for applications such as cutting tools, biomedical implants and armor materials [25]. Ti doping in barium titanate ( $\text{BaTiO}_3$ ) can modify its ferroelectric properties, leading to improved piezoelectricity and a greater dielectric constant, which can be useful for applications such as sensors and actuators [26].

The mechanical and physical characteristics of metals can also be changed through titanium doping. For example, Ti doping in copper (Cu) can improve its strength, ductility and thermal stability, making it suitable for applications such as electrical interconnects and microelectronic packaging [27]. Similarly, Ti doping in iron (Fe) can enhance its magnetic properties, making it suitable for magnetic storage and sensing applications [28].

Thus, the aim of this research paper was to study the Ti doping effects on the microstructure and mechanical properties of the high-entropy alloy CoCrFeMoNi. Ti was chosen as a doping element due to its grain-refining effect, which allows the improvement of strength and ductility. For now, there are no data available about this particular doping method on high-entropy alloys from this alloying system and which are manufactured using the vacuum arc melting technique.

## 2. Materials and Methods

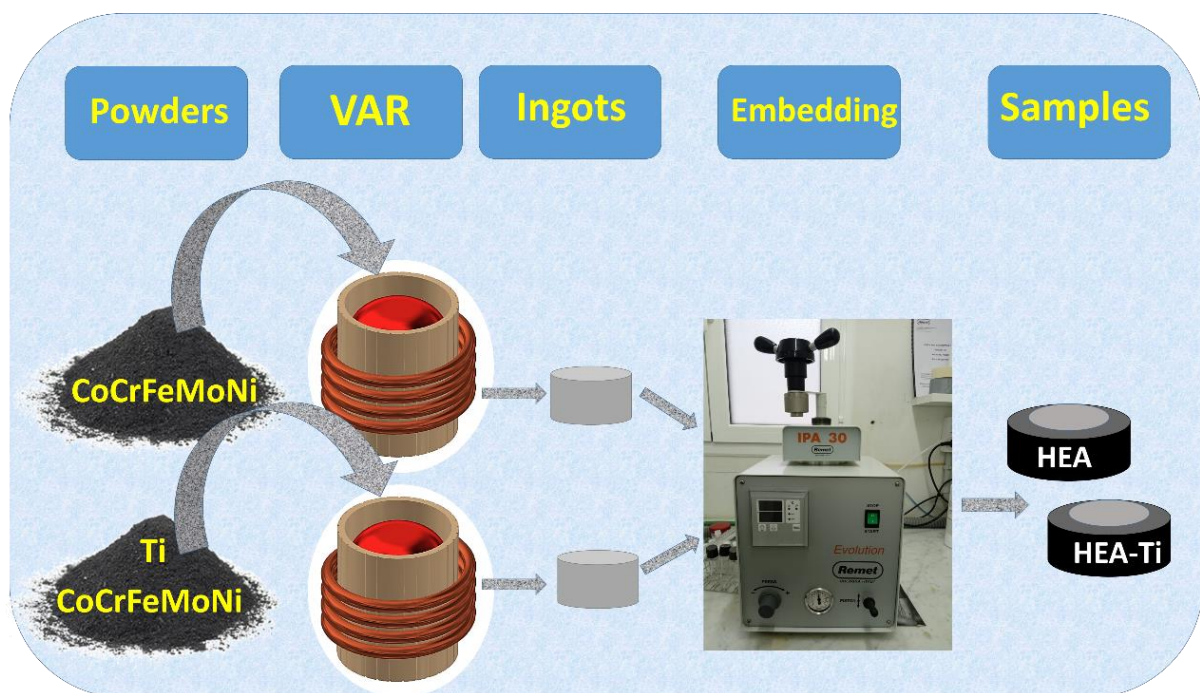
### 2.1. Sample Preparation

The high-entropy CoCrFeMoNi alloy (named HEA) and Ti-doped CoCrFeMoNi alloy (named HEATi) were obtained using a MRF ABJ 900 vacuum arc remelting (VAR) installation from ERAMET Laboratory (UPB, Bucharest, Romania). To design the metallic charge, potential losses from vaporization were considered, as well as the predicted level of chemical element incorporation during melting. Energy dispersive X-ray analysis (EDS) employing a Fei XL30 ESEM (MTM, Leuven, Belgium) scanning electron microscope outfitted with an EDAX Sapphire detector was used to ascertain the elemental composition of the HEA and doped HEATi samples. The results (in wt% and at%) are presented in Table 1.

Raw materials with high purity levels of at least 99.7% for Co, Cr, Fe, Mo, Ni and Ti were utilized. The obtained alloys were subjected to 8 rounds of flipping and re-melting in VAR equipment under an inert Argon atmosphere to achieve adequate homogeneity. The resultant ingots were rods 10 cm in length and 1 cm in diameter. To carry out assessments of the structure, composition and mechanical properties, the samples underwent a three-stage surface processing procedure. First, they were embedded into a phenolic resin cylinder (see Figure 1) and then polished using SiC abrasive papers with increasing grain sizes ranging from 240 to 2000 grit. Following this, they underwent final polishing utilizing a 0.1  $\mu\text{m}$  alpha alumina paste and were ultimately cleaned using ultrasonic-deionized water according to ASTM E3-11(2017) [29].

**Table 1.** Chemical composition of as-cast experimental samples HEA and HEATi.

Element	wt%		at%	
	HEA	HEATi	HEA	HEATi
Co	20.67	20.09	21.52	21.09
Cr	19.99	19.04	23.58	22.67
Fe	19.88	19.29	21.84	21.37
Mo	20.20	22.10	12.98	14.26
Ni	19.27	19.20	20.14	20.24
Ti	-	0.28	-	0.36

**Figure 1.** Sample fabrication for analysis.

## 2.2. Microstructural Characterization

To investigate the microstructure, the prepared cross-sections cut off from the alloy ingots were subjected to electrochemical etching using a 10% oxalic acid solution, with a voltage of 5 V and an immersion time ranging from 5 to 25 s. The microstructure was first examined using an OLYMPUS BX 51 (Olympus Corp., Tokyo, Japan) optical microscope (OM).

The samples' X-ray diffraction data were measured using a Bruker D8 ADVANCE diffractometer (Bruker Corp., Billerica, MA, USA) and used to characterize the phase analysis.  $\text{CuK}\alpha$  radiation ( $\lambda = 1.5418 \text{ \AA}$ ) in the range of  $2\theta = 5\text{--}80^\circ$  with a step size of  $0.02^\circ$  at a power of 40 kV (LYNXEYE XE high-speed position-sensitive detector) in Bragg–Brentano geometry was employed for the analysis.

For SEM observations, a Hitachi TM3030 Scanning Electron Microscope with an EDX spectrometer (Hitachi High-Tech Science Corporation, Tokyo, Japan) was utilized, with voltage set to 15 kV and the working distance set to 10.7 mm.

## 2.3. Microhardness

To determine the microhardness of the samples, an indentation test was conducted using a Shimadzu HMV 2T microhardness tester (Shimadzu, Kyoto, Japan) at  $25^\circ\text{C}$  and 45% humidity. The sample, which had previously been polished to a mirror finish, was examined using an optical microscope before perpendicular microhardness measurements

were taken. Indentations were made at 0.5 mm intervals along the sample diameter, using a load of 1.961 N and a dwell time of 10 s. In accordance with ISO 14577-1:2015 [30], 10 indentations were made for each sample and the Vickers hardness (HV) was then calculated as the average value of each individual sample.

#### 2.4. Three-Point Bending Test

To determine the modulus of elasticity of the material, a three-point bending test was conducted. The specimens were prepared via cutting samples using a BUEHLER IsoMet<sup>®</sup> 4000 precision linear saw (Lake Bluff, IL, USA), from which minimal alteration of the material occurs. The cutting process utilizes a blade speed of 2200 rpm and a feed speed of 13.9 mm/min. A total of ten samples were selected from each alloy to obtain a weighted average of the test results. The test was performed using a BOSE Corporation Electroforce 3100 machine (Bose Corporation, Eden Prairie, MN, USA), applying a maximum load of 22 N until the material fractured or reached the maximum load capacity according to ISO 7438:2020 [31].

### 3. Results and Discussions

#### 3.1. Microstructural Characterization

To study the effect of Ti doping on the microstructure, the base CoCrFeMoNi alloy (Figure 2a,b) and the Ti-doped one (Figure 2c,d) were examined using optical microscopy. The microstructure of both alloys is dense and free of cracks. From the images, it can easily be seen that the dimensions of the dendrites in the case of the Ti-doped alloy are much finer at the same magnification. Over the same surface area, approximately twelve grains of different diameters (bordered by grain boundaries) are observed in the Ti-doped alloy, while in the un-doped alloy there are only two coarse grains.

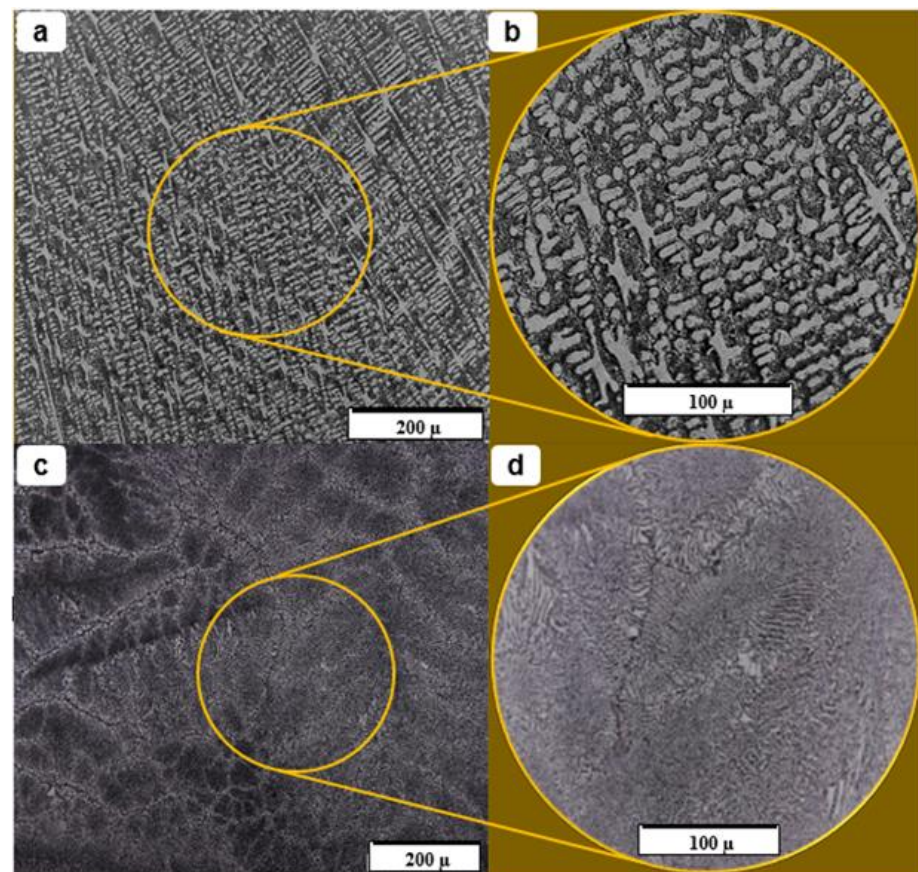


**Figure 2.** Metallographic OM images of HEA (a,b) and HEATi (c,d).

XRD analysis of the CoCrFeMoNi alloy reveals a microstructure consisting of three main phases: an FCC (face-centered cubic) solid solution and a BCC (body-centered cubic) solid solution, in addition to a Laves phase (Figure 3). This result agrees with the result obtained for the equiatomic CoCrFeNi alloy, reported to be multiphase at room temperature [32]. The FCC solid solution is the dominant phase and consists of a mixture of Co, Cr, Fe, Mo and Ni atoms. The BCC solid solution consists mainly of Mo and Fe atoms. The ternary intermetallic hard phase (Laves phase), consisting of Co, Fe, and Mo atoms, is distributed in both phases. The uniform distribution and finer dimensions of Laves phases can contribute to increased mechanical strength properties.

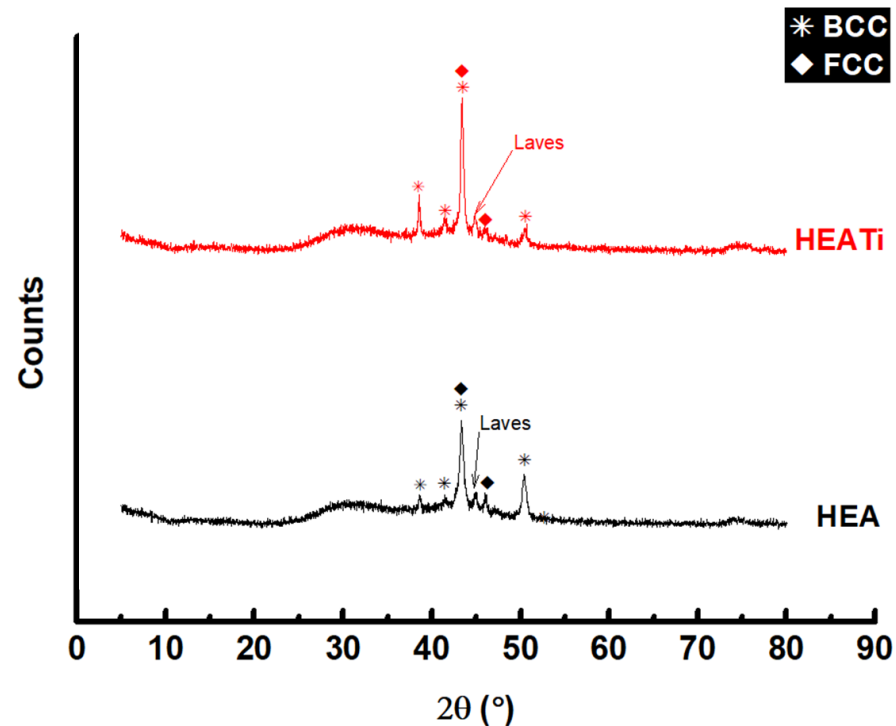


**Figure 3.** XRD patterns of the HEA and HEATi.

Sherrer's equation is used to calculate the size of nanocrystalline materials from the full width at half maximum (FWHM) of a diffraction peak acquired from X-ray diffraction (XRD) research. The equation is as follows:

$$D = \frac{K\lambda}{(\beta \cos \theta)} \quad (1)$$

where:

$D$  denotes the material's average crystallite size in nanometers (nm).

$K$  is a dimensionless form factor that is usually taken as 0.9.

$\lambda$  is the wavelength of the X-ray radiation used for the diffraction measurement, which is usually measured in angstroms (Å).

$\beta$  is the diffraction peak's FWHM in radians.

$\theta$  is the Bragg angle, which is the X-ray beam's angle of incidence on the sample surface.

The equation connects the finite size of crystallites in a material to the widening of diffraction peaks. The diffraction peak becomes wider as the crystallite size decreases. The equation assumes that the crystallites in the sample are spherical and randomly orientated. The results for the HEA and HEATi are presented in Figure 4.

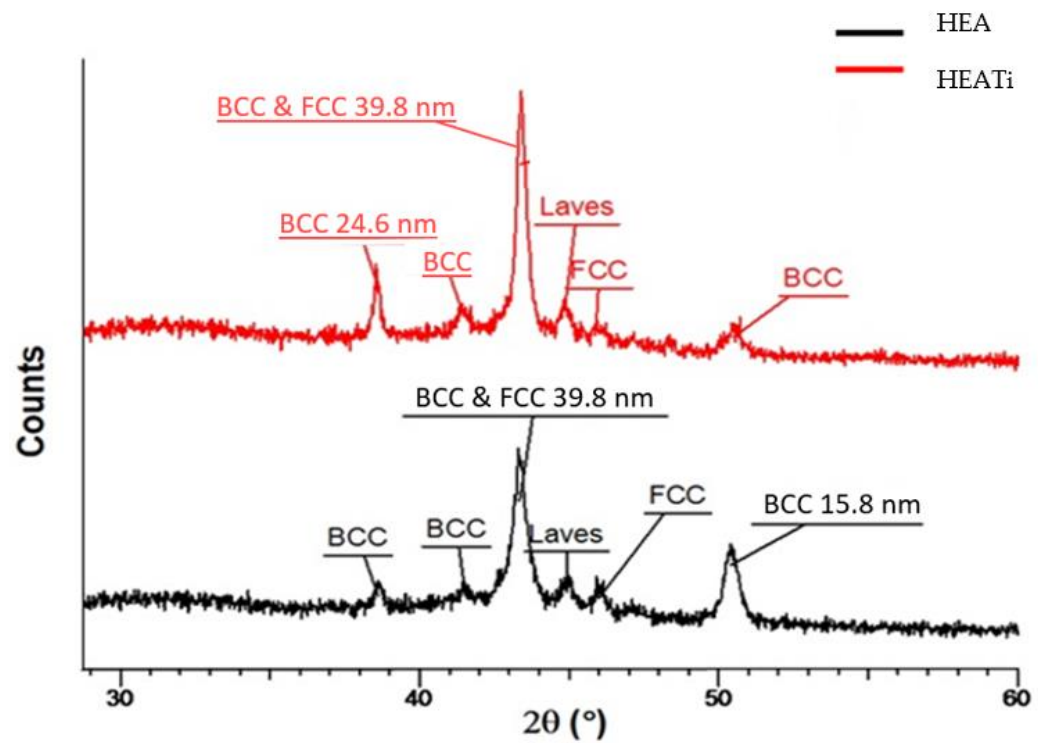


Figure 4. Size of crystallites in HEA and HEATi.

The SEM images and elemental maps of the samples are presented in Figure 5.

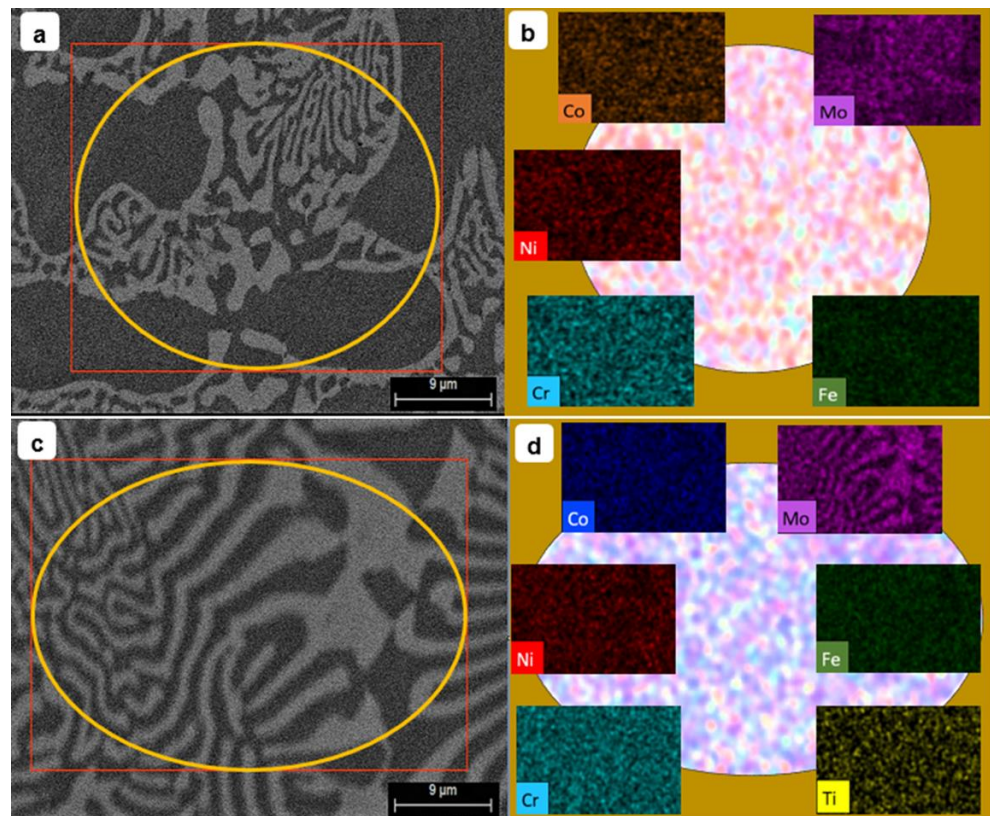


Figure 5. SEM image (a) and elemental maps (b) of HEA sample; SEM image (c) and elemental maps (d) of HEATi sample.

To uncover the chemical composition of the analyzed samples within different micro-areas identified as spectra, a semi-quantitative analysis was performed in ten points located on different phases (see Figures 6 and 7): five in the dendritic zone (D) and five in the interdendritic zone (ID). Then, the mean and standard deviation were calculated. Tables 2 and 3 display the measured concentration values of the elements detected in the respective alloys' composition. An analysis comparing the microstructure of the two alloys revealed that upon introducing Ti to the CoCrFeMoNi alloy, there was a noticeable reduction in the volume fraction of interdendritic zones. It is common to observe the presence of the  $\sigma$  phase in this type of alloy, in addition to the FCC structure [33]. When Mo was added to the CoCrFeNi system, a eutectic structure emerged that contained intermetallic phases ( $\sigma$  and  $\mu$ ) within the FCC phase. This eutectic microstructure had a notable impact on the mechanical properties of the alloy, leading to increased hardness and yield strength. The Mo concentration in the interdendritic zone is the primary factor that contributes to the appearance of the  $\sigma$  phase [34]. The CoCrFeNiMo high-entropy alloy was found to contain an approximately 14% Cr- and Mo-rich  $\sigma$  phase [35]. In the HEA sample, the Mo concentration in the interdendritic zones dropped from 34.4 wt% to 15.6 wt%. In contrast, the Cr concentration remained steady, hovering around 20 wt%. This shift in concentration ultimately resulted in a decrease in the tendency to form a Laves phase.

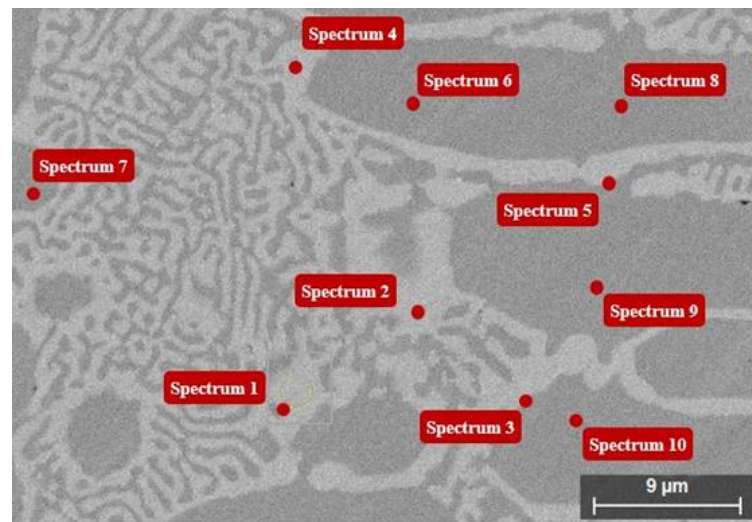


Figure 6. Selected points on the HEA surface for EDS analysis.

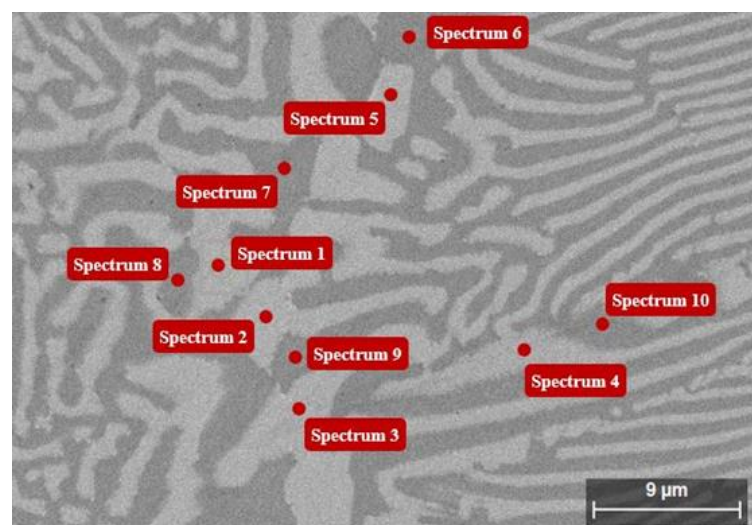


Figure 7. Selected points on the HEATi surface for EDS analysis.

**Table 2.** The HEA sample's EDS analysis results in weight percentage.

Spectrum	Co	Cr	Fe	Mo	Ni
1	17.70	20.52	15.11	34.40	12.27
2	17.43	19.35	16.88	33.12	13.22
3	16.50	21.04	15.29	33.16	14.01
4	16.71	20.46	17.48	33.02	12.33
5	16.39	22.97	16.74	31.24	12.67
6	22.39	19.33	21.58	17.64	19.06
7	23.10	19.68	19.92	15.58	21.72
8	22.68	19.10	19.78	17.37	21.08
9	22.70	19.87	19.45	15.94	22.03
10	22.52	17.52	18.15	20.30	21.51
Mean	19.81	19.98	18.04	25.18	16.99
Standard deviation	0.92	0.43	0.64	2.51	1.32

**Table 3.** The results in weight percentage of EDS analysis of the alloy HEATi.

Spectrum	Co	Cr	Fe	Mo	Ni	Ti
1	17.05	17.84	14.30	37.87	12.67	0.27
2	15.63	18.17	13.80	39.35	13.04	0.00
3	16.80	19.41	13.30	37.92	12.45	0.12
4	14.54	20.96	15.46	37.92	10.58	0.54
5	16.83	19.94	15.51	33.79	13.55	0.38
6	21.93	16.78	19.47	19.72	21.51	0.60
7	20.36	20.00	23.20	18.26	17.77	0.41
8	20.00	17.37	19.43	25.16	18.04	0.00
9	21.30	14.53	21.13	19.30	23.50	0.24
10	20.7	14.73	21.57	24.62	18.70	0.00
Mean	18.51	17.97	17.72	29.39	16.18	0.26
Standard deviation	0.79	0.66	1.09	2.64	1.30	0.07

The segregation factor is a helpful parameter to evaluate an alloy's degree of segregation and to compare the segregation behavior of various alloys. When the SR value is higher, there is more concentration of the element in the alloy's most segregated area, indicating a greater level of segregation.

The segregation factor (see Table 4) can be measured experimentally using various techniques, such as electron microscopy and energy-dispersive X-ray spectroscopy (EDS). These techniques allow the concentration of elements to be measured at different locations within the alloy, providing information on the extent of segregation.

$$S_R = \frac{\text{Element concentration in Dendritic area}}{\text{Element concentration in Interdendritic area}} \quad (2)$$

**Table 4.** Composition average results in D and ID areas and SR values for HEA and HEATi alloys.

Alloy	Parameters	Co	Cr	Fe	Mo	Ni	Ti
HEA	D	22.68	19.10	19.78	17.37	21.08	-
	ID	16.95	20.87	16.30	32.99	12.90	-
	S <sub>R</sub>	1.34	0.92	1.21	0.53	1.63	-
HEATi	D	20.86	16.68	20.96	21.41	19.90	0.25
	ID	16.17	19.26	14.47	37.37	12.46	0.26
	S <sub>R</sub>	1.29	0.87	1.45	0.57	1.60	0.96

Upon conducting nanoscale analysis of the HEA sample, it was found that the dendritic region was abundant in Co, Fe and Ni, but had low levels of Mo. On the other hand, the interdendritic region was rich in Mo but depleted in Co, Fe and Ni. In the HEA alloy, the

element that exhibited no noticeable difference between the D and ID regions, with slightly increase of the concentration observed in the D zone, was chromium.

As Ti doping was introduced, the effect of iron became more prominent, and Ti exhibited a noticeable difference in the two regions. Cobalt, iron, and molybdenum exhibited an increase in their segregation ratios, while nickel showed a decrease in its segregation ratio. This indicates that these elements formed fewer intermetallic compounds or precipitated less. The segregation ratio of chromium remained largely unchanged. It can be said that Ti doping reduced the solubility limit of the solid phase for nickel, cobalt and iron, and increased it for molybdenum and titanium, while chromium was almost unaffected. In our alloys, doping with 0.36 at.% Ti changed the distribution of Mo in the dendritic zones (max. 39.35 wt%, min. 33.79 wt%) compared to the interdendritic zones (max. 29.39 wt%, min. 18.26 wt%).

### 3.2. Mechanical Properties

The analysis of mechanical properties focuses on two specific methods for evaluating toughness: microhardness and three-point bending. Both methods involve preparing samples, which can lead to changes in the material structure due to the cutting process. These changes can create thin layers of altered material that may affect the results of the elastic modulus. Although efforts were made to minimize this effect and verify the accuracy of the conclusions about the underlying material, additional work is needed to eliminate the impact of sample preparation on the results.

#### 3.2.1. Microhardness

Microhardness tests were carried out on the two samples, HEA and HEATi (see Figure 8).

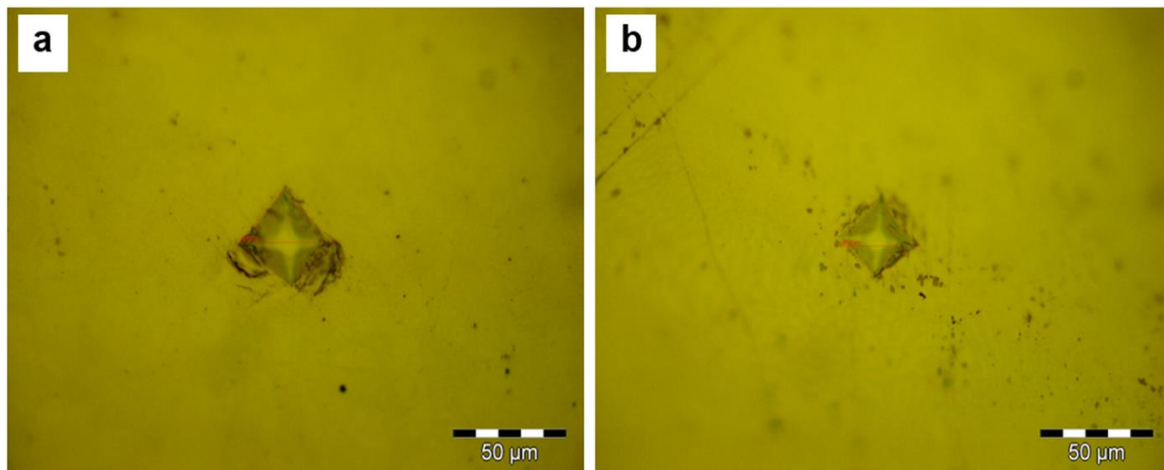


**Figure 8.** Vickers hardness testing on (a) HEA sample and (b) HEATi sample, using a load of 1.961 N and a dwell time of 10 s.

Hardness imprints indicate how the surface of the alloy is deformed through slow progressive pressing with the diamond indenter. Thus, it is possible to observe the deformation planes that appear at the tips of the imprint as well as the deviation from the ideal rhombic shape of the imprint if the material is inhomogeneous in the two directions of deformation. The values of the diagonals of the fingerprints indicate the hardness differences between the two studied alloys. HEA alloy has a larger diameter, which means decreased hardness compared to the HEATi alloy.

Table 5 provides information about the microhardness values in HV 0.2 and standard deviation for the 10 measurements conducted on each sample. The data show that the inclusion of Ti had a positive effect on the average microhardness of HEA. The addition of titanium during the doping process impacted several aspects, including the size of the

grains and their boundaries, distribution of elements and the formation of precipitates. These changes resulted in variations in microhardness and the strengthening mechanisms of the metal [33,36]. The four primary mechanisms for strengthening metals are solid solution, precipitation, dislocation and boundary strengthening. The titanium doping process mainly employs solid solution, precipitation and dislocation strengthening to achieve its effects. The characteristics of the microstructure significantly impacted the properties of the sample that was doped with titanium. As a result, the main strengthening mechanisms were precipitation and dislocation.

**Table 5.** Microhardness values HV 0.2 and standard deviation for HEA and HEATi.

Alloy	HV 0.2
HEA	369.20 ± 0.56
HEATi	450.90 ± 0.50

The process of doping revealed a discrepancy in the concentration of Mo between the dendritic and interdendritic zones, leading to the strengthening mechanisms of dissolution and dislocation. Furthermore, the formation of a Laves phase was beneficial for strengthening via precipitation, which plays a crucial role in enhancing the microhardness of the titanium alloy.

Taking into account that the grain size of the HEA sample is greater than that of HEATi (see metallographic images from Figure 2), the obtained values of microhardness are in accordance with the Hall–Petch relationship, which is based on the idea that the smaller the grains in a metal, the greater the number of grain boundaries per unit volume [37]. These grain boundaries act as barriers to dislocation motion, which is the primary mechanism of plastic deformation in metals. Therefore, a high density of grain boundaries can hinder the movement of dislocations and make it more difficult for the metal to deform plastically, resulting in an increase in microhardness.

### 3.2.2. Three-Point Bending Test

Figures 9 and 10 present load-displacement diagrams obtained through the three-point bending test on two samples. The elastic limit of the alloy was identified as the point at which the sample returned to its original shape after deformation. Within this limit, the graph displayed a linear relationship, and the gradient of this line was calculated using the formula  $d_F/d_\epsilon = 48EI/L^3$ , where E represents the Young's modulus of the sample of length L, supported on two roller supports, and subjected to a concentrated load F at its center with a central deflection  $\epsilon$ . To determine the second moment of area, I, the equation  $I = (a^3 \cdot b)/12$  was utilized, with a representing the sample's depth and b representing its width. Using these calculations, the average modulus of elasticity for each alloy was determined, with results indicating that the alloy lacking Ti had a slightly lower modulus of elasticity than the Ti-containing alloy, as shown in Table 6. Ten samples of each alloy underwent testing.

**Table 6.** Modulus of elasticity values of the two samples, HEA and HEATi.

Alloy	E (GPa)
HEA	173.99 ± 4.25
HEATi	177.89 ± 3.70

It was found that the values obtained for HEA and HEATi are almost the same; the addition of Ti does not modify the modulus of elasticity and, therefore, its stiffness.

Additionally, Figures 9 and 10 display SEM images of the fracture surfaces for both alloys, revealing a brittle fracture in both cases, with a visible cleavage-like fracture plane.

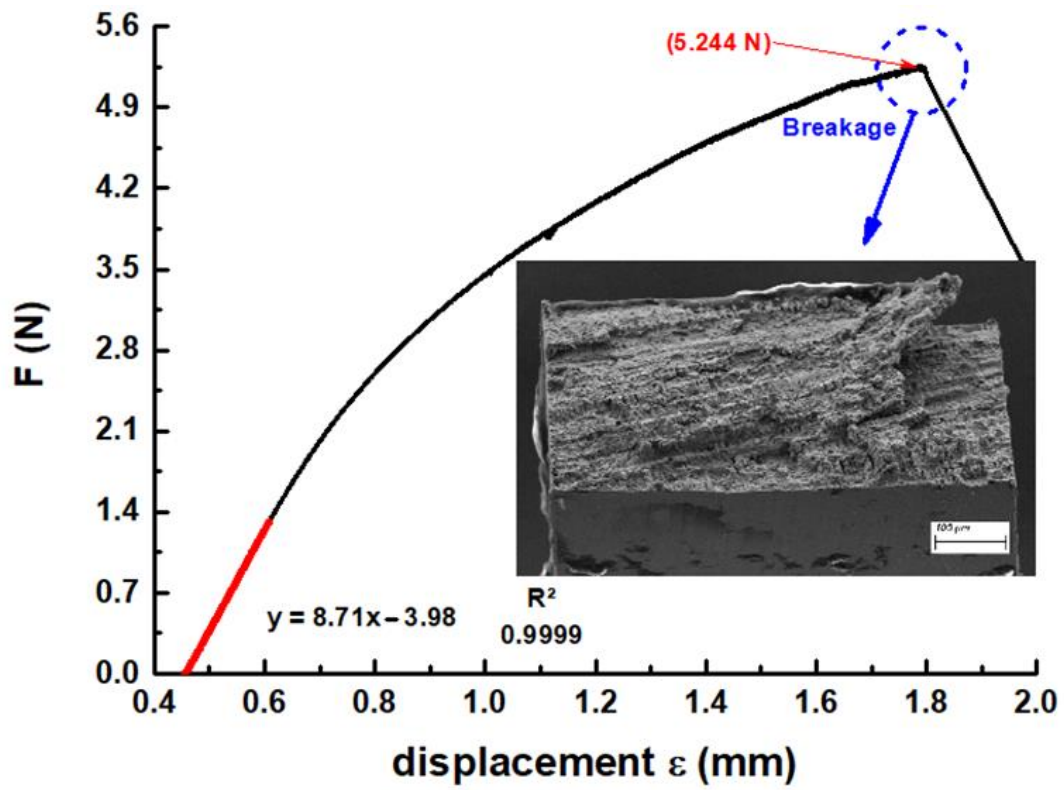


Figure 9. Load-displacement diagrams obtained on HEA.

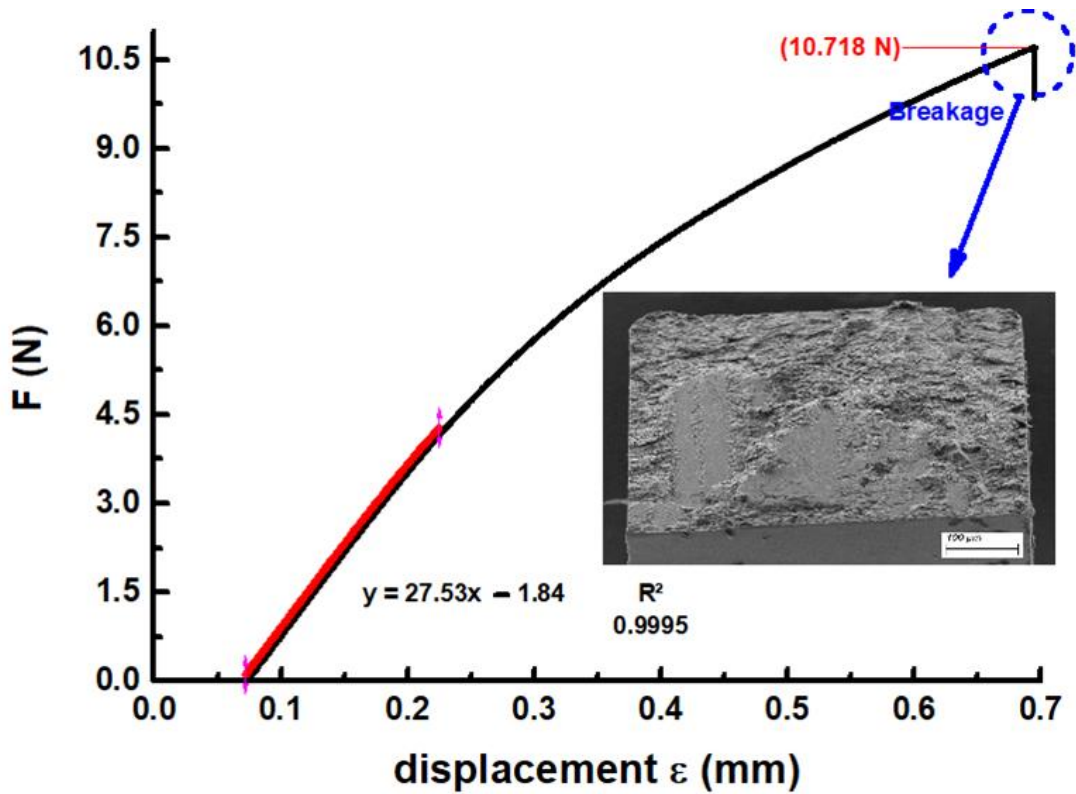


Figure 10. Load-displacement diagrams obtained on HEATi.

#### 4. Conclusions

The CoCrFeMoNi high-entropy alloy was examined to determine the impact of Ti doping on its microstructure and mechanical properties. The microstructure analysis revealed a fundamental matrix that consisted of both face-centered cubic (FCC) and body-centered cubic (BCC) phases, along with the formation of a Laves phase. Upon the addition of Ti doping, there was a noticeable refinement of the grains within the alloy. Additionally, there was a reduction in the disparity between the concentration of Mo within the interdendritic and dendritic regions. The increase in Ti doping also led to a rise in microhardness, which was measured to be 451 HV 0.2, up from 369 HV 0.2. This aspect can be taken into account when designing the alloy for conditions where improved hardness or good wear resistance are required. However, despite the increase in breaking strength and microhardness values, no significant modifications in the elastic modulus of the HEATi alloy were observed.

**Author Contributions:** S.J.B.-G., writing—original draft preparation, investigation and management; J.C.M.-R., conceptualization and validation; C.J.-M., investigation, writing—review and editing; I.V., methodology, investigation and data curation. All authors have read and agreed to the published version of the manuscript.

**Funding:** This work was supported by the Romanian National Authority for Scientific Research, CNDI-UEFISCDI, through project number PN-III-P2-2.1-PED-2019-3953, contract 514PED2020: “New ceramic layer composite material processed by laser techniques for corrosion and high temperature applications—LASCERHEA”, within PNCDI III, by Cabildo de Gran Canaria, project number CABINFR2019-07 and by the project ULPGC Excellence, funded by the Department of Economy, Knowledge and Employment of the Canary Islands Government.

**Data Availability Statement:** All data provided in the present manuscript are available to whom it may concern.

**Conflicts of Interest:** The authors declare no conflict of interest.

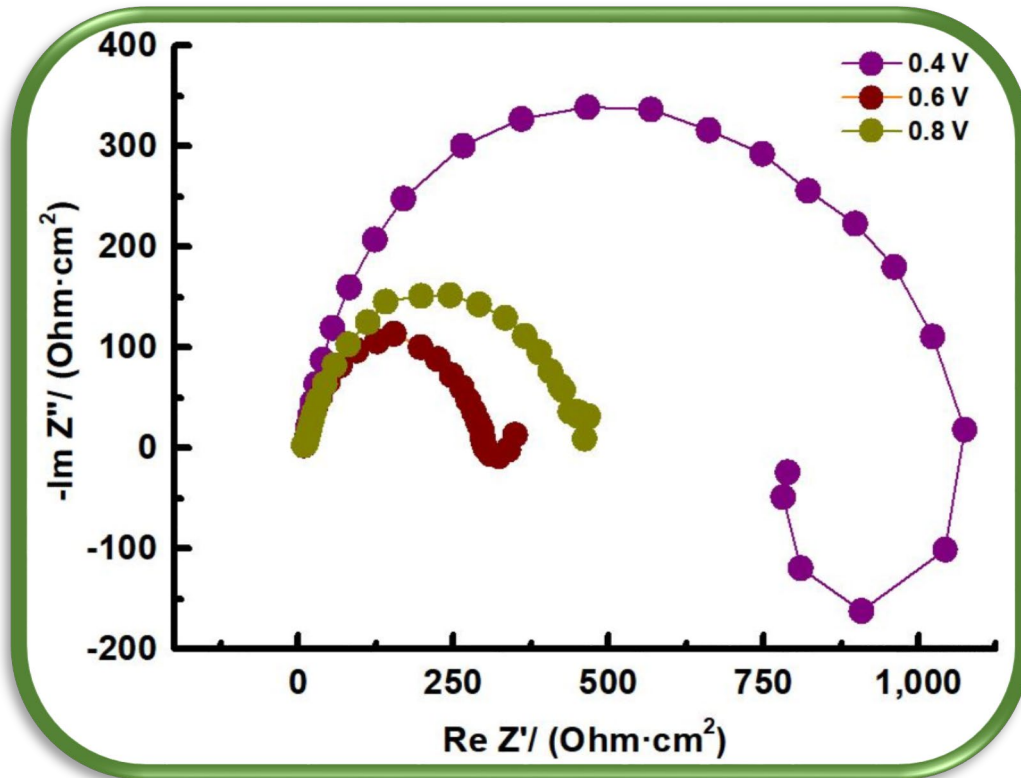
#### References

1. Cantor, B.; Chang, I.T.H.; Knight, P.; Vincent, A.J.B. Microstructural development in equiatomic multicomponent alloys. *Mater. Sci. Eng. A* **2004**, *375–377*, 213–218. [[CrossRef](#)]
2. Yeh, J.W. Recent progress in high-entropy alloys. *Ann. Chim. Sci. Mater.* **2006**, *31*, 633–648. [[CrossRef](#)]
3. López Ríos, M.; Socorro Perdomo, P.P.; Voiculescu, I.; Geanta, V.; Crăciun, V.; Boerasu, I.; Mirza Rosca, J.C. Effects of nickel content on the microstructure, microhardness and corrosion behavior of high-entropy AlCoCrFeNi<sub>x</sub> alloys. *Sci. Rep.* **2020**, *10*, 21119. [[CrossRef](#)] [[PubMed](#)]
4. Florido-Suarez, N.; Socorro-Perdomo, P.; Geanta, V.; Mirza-Rosca, J. Effect of Heat Treatment on the Microstructure and Corrosion Resistance of AlCoCrFeNi High-Entropy Alloy. *Microsc. Microanal.* **2021**, *27*, 3372–3374. [[CrossRef](#)]
5. Socorro-Perdomo, P.P.; Florido-Suárez, N.R.; Voiculescu, I.; Mirza-Rosca, J.C. Comparative eis study of alxcocrfeni alloys in ringer’s solution for medical instruments. *Metals* **2021**, *11*, 928. [[CrossRef](#)]
6. Florido-Suarez, N.; Socorro-Perdomo, P.; Voiculescu, I.; Mirza-Rosca, J. Microstructure and Adjustment in Tensile Strength of Al 0.8 CoCrFeNi Fibers. *Microsc. Microanal.* **2021**, *27*, 3386–3388. [[CrossRef](#)]
7. Wu, G.; Liu, C.; Brognara, A.; Ghidelli, M.; Bao, Y.; Liu, S.; Wu, X.; Xia, W.; Zhao, H.; Rao, J.; et al. Symbiotic crystal-glass alloys via dynamic chemical partitioning. *Mater. Today* **2021**, *51*, 6–14. [[CrossRef](#)]
8. Socorro-Perdomo, P.; Florido-Suarez, N.; Voiculescu, I.; Mirza-Rosca, J. Biocompatibility of New High-Entropy Alloys with Non-Cytotoxic Elements. *Microsc. Microanal.* **2021**, *27*, 1772–1774. [[CrossRef](#)]
9. Li, T.; Wang, D.; Zhang, S.; Wang, J. Corrosion Behavior of High Entropy Alloys and Their Application in the Nuclear Industry—An Overview. *Metals* **2023**, *13*, 363. [[CrossRef](#)]
10. Rios, M.L.; Baldevenites, V.L.; Voiculescu, I.; Rosca, J.M. AlCoCrFeNi High Entropy Alloys as Possible Nuclear Materials. *Microsc. Microanal.* **2020**, *26*, 406–407. [[CrossRef](#)]
11. Li, P.; Tong, Y.; Wang, X.; Sato, Y.S.; Dong, H. Microstructures and mechanical properties of AlCoCrFeNi<sub>2.1</sub>/6061-T6 aluminum-matrix composites prepared by friction stir processing. *Mater. Sci. Eng. A* **2023**, *863*, 144544. [[CrossRef](#)]
12. Ron, T.; Shirizly, A.; Aghion, E. Additive Manufacturing Technologies of High Entropy Alloys (HEA): Review and Prospects. *Materials* **2023**, *16*, 2454. [[CrossRef](#)] [[PubMed](#)]
13. Lin, C.; Yao, Y. Corrosion-Resistant Coating Based on High-Entropy Alloys. *Metals* **2023**, *13*, 205. [[CrossRef](#)]
14. Bhaskaran Nair, R.; Supekar, R.; Morteza Javid, S.; Wang, W.; Zou, Y.; McDonald, A.; Mostaghimi, J.; Stoyanov, P. High-Entropy Alloy Coatings Deposited by Thermal Spraying: A Review of Strengthening Mechanisms, Performance Assessments and Perspectives on Future Applications. *Metals* **2023**, *13*, 579. [[CrossRef](#)]

15. Qi, W.; Wang, W.; Yang, X.; Zhang, G.; Ye, W.; Su, Y.; Li, Y.; Chen, S. Effects of Al and Ti co-doping on the strength-ductility-corrosion resistance of CoCrFeNi-AlTi high-entropy alloys. *J. Alloys Compd.* **2022**, *925*, 166751. [[CrossRef](#)]
16. Pikalova, E.Y.; Kalinina, E.G.; Pikalova, N.S.; Filonova, E.A. High-Entropy Materials in SOFC Technology: Theoretical Foundations for Their Creation, Features of Synthesis, and Recent Achievements. *Materials* **2022**, *15*, 8783. [[CrossRef](#)]
17. Cui, G.; Han, B.; Yang, Y.; Wang, Y.; Chunyang, H. Microstructure and tribological property of CoCrFeMoNi High entropy alloy treated by ion sulfurization. *J. Mater. Res. Technol.* **2020**, *9*, 2598–2609. [[CrossRef](#)]
18. Alloys, M. Cryogenic-Mechanical Properties and Applications of Multiple-Basis-Element Alloys. *Metals* **2022**, *12*, 2075.
19. Wang, Z.; Jin, J.; Zhang, G.H.; Fan, X.H.; Zhang, L. Effect of temperature on the passive film structure and corrosion performance of CoCrFeMoNi high-entropy alloy. *Corros. Sci.* **2022**, *208*, 110661. [[CrossRef](#)]
20. Zhou, Z.; Jiang, F.; Yang, F.; Yang, Y.; Liang, P. Novel laser cladding FeCoNiCrNb0.5Mox high-entropy alloy coatings with excellent corrosion resistance. *Mater. Lett.* **2023**, *335*, 133714. [[CrossRef](#)]
21. Brito-Garcia, S.; Mirza-Rosca, J.; Geanta, V.; Voiculescu, I. Mechanical and Corrosion Behavior of Zr-Doped High-Entropy Alloy from CoCrFeMoNi System. *Materials* **2023**, *16*, 1832. [[CrossRef](#)] [[PubMed](#)]
22. Kippeny, T.; Swafford, L.A.; Rosenthal, S.J. Semiconductor nanocrystals: A powerful visual aid for introducing the particle in a box. *J. Chem. Educ.* **2002**, *79*, 1094–1100. [[CrossRef](#)]
23. Mendoza-Estrada, V.; González-García, A.; López-Pérez, W.; Pinilla, C.; González-Hernández, R. Structural, electronic and magnetic properties of Ti-doped polar and nonpolar GaN surfaces. *J. Cryst. Growth* **2017**, *467*, 12–17. [[CrossRef](#)]
24. Cui, Z.; Ke, X.; Li, E.; Liu, T. Electronic and optical properties of titanium-doped GaN nanowires. *Mater. Des.* **2016**, *96*, 409–415. [[CrossRef](#)]
25. Lee, D.K.; Kim, G.H.; Sohn, H.; Yang, M.K. Ti-doped alumina based reliable resistive switching in sub- $\mu$  A regime. *Appl. Phys. Lett.* **2020**, *116*, 213503. [[CrossRef](#)]
26. Scott, J.F. Applications of modern ferroelectrics. *Science* **2007**, *315*, 954–959. [[CrossRef](#)]
27. Ueki, M.; Hiroi, M.; Ikarashi, N.; Onodera, T.; Furutake, N.; Inoue, N.; Hayashi, Y. Effects of Ti addition on via reliability in Cu dual damascene interconnects. *IEEE Trans. Electron. Devices* **2004**, *51*, 1883–1891. [[CrossRef](#)]
28. Gutfleisch, O.; Willard, M.A.; Brück, E.; Chen, C.H.; Sankar, S.G.; Liu, J.P. Magnetic materials and devices for the 21st century: Stronger, lighter, and more energy efficient. *Adv. Mater.* **2011**, *23*, 821–842. [[CrossRef](#)]
29. ASTM E3-11(2017); Standard Guide for Preparation of Metallographic Specimens. ASTM International: West Conshohocken, PA, USA, 2017.
30. ISO 14577-1:2015; Metallic Materials—Instrumented Indentation Test for Hardness and Materials Parameters—Part 1: Test Method. International Organization for Standardization: Geneva, Switzerland, 2015.
31. ISO 7438:2020; Metallic Materials—Bend Test. International Organization for Standardization: Geneva, Switzerland, 2020.
32. Kini, M.K.; Lee, S.; Savan, A.; Breitbach, B.; Addab, Y.; Lu, W.; Ghidelli, M.; Ludwig, A.; Bozzolo, N.; Scheu, C.; et al. Nanocrystalline equiatomic CoCrFeNi alloy thin films: Are they single phase fcc? *Surf. Coat. Technol.* **2021**, *410*, 126945. [[CrossRef](#)]
33. Qiu, X. Microstructure and mechanical properties of CoCrFeNiMo high-entropy alloy coatings. *J. Mater. Res. Technol.* **2020**, *9*, 5127–5133. [[CrossRef](#)]
34. Shun, T.T.; Chang, L.Y.; Shiu, M.H. Microstructure and mechanical properties of multiprincipal component CoCrFeNiMox alloys. *Mater. Charact.* **2012**, *70*, 63–67. [[CrossRef](#)]
35. Fan, R.; Wang, L.; Zhao, L.; Wang, L.; Zhao, S.; Zhang, Y.; Cui, B. Synergistic effect of Nb and Mo alloying on the microstructure and mechanical properties of CoCrFeNi high entropy alloy. *Mater. Sci. Eng. A* **2022**, *829*, 142153. [[CrossRef](#)]
36. Ast, J.; Ghidelli, M.; Durst, K.; Göken, M.; Sebastiani, M.; Korsunsky, A.M. A review of experimental approaches to fracture toughness evaluation at the micro-scale. *Mater. Des.* **2019**, *173*, 107762. [[CrossRef](#)]
37. Whang, S.H. Introduction. In *Nanostructured Metals and Alloys*; Whang, S.H., Ed.; Woodhead Publishing Series in Metals and Surface Engineering; Woodhead Publishing: Cambridge, UK, 2011; pp. xxi–xxxv; ISBN 978-1-84569-670-2.

**Disclaimer/Publisher’s Note:** The statements, opinions and data contained in all publications are solely those of the individual author(s) and contributor(s) and not of MDPI and/or the editor(s). MDPI and/or the editor(s) disclaim responsibility for any injury to people or property resulting from any ideas, methods, instructions or products referred to in the content.

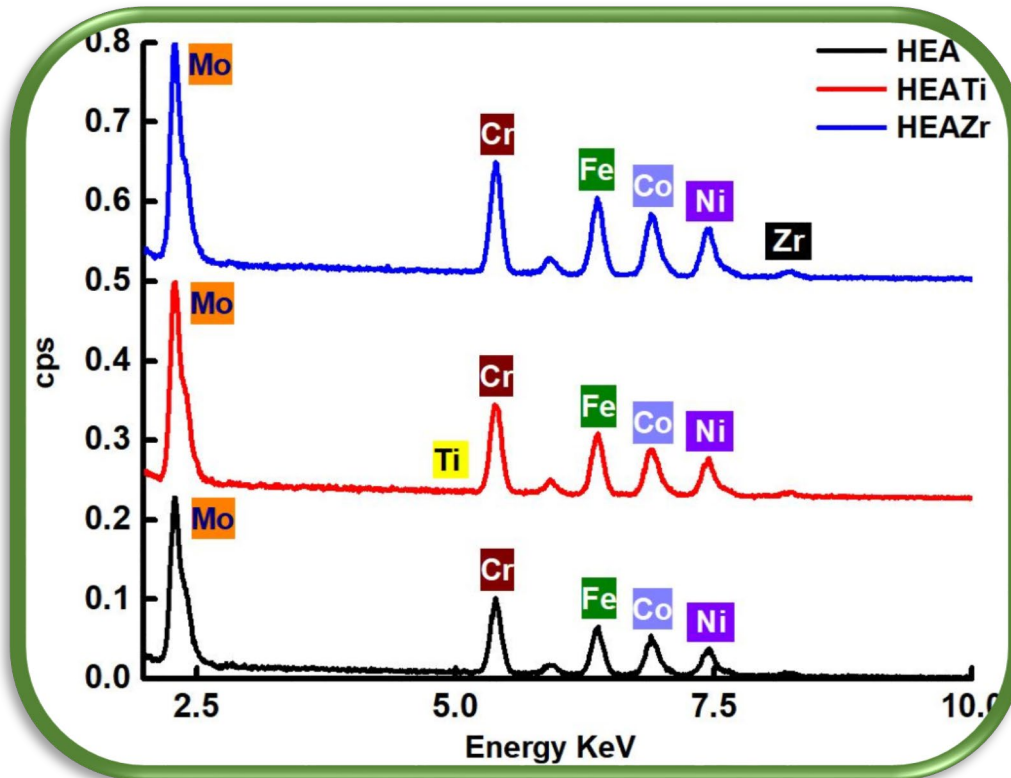




Documento de  
autoría

4





Publicaciones  
co-participadas

5





[www.microscopy.org/MandM/2023](http://www.microscopy.org/MandM/2023)  
for up-to-date meeting information

# CALL FOR PAPERS

Submission Deadline: **February 16, 2023**



**M&M 2023**  
**MICROSCOPY &  
MICROANALYSIS**  
Minneapolis, MN • July 23-27





# Behavior of Ti-doped CoCrFeMoNi High Entropy Alloy

Santiago Brito-García<sup>1</sup>, Cristina Jiménez-Marcos<sup>1</sup>, Julia Mirza-Rosca<sup>1\*</sup> and Ionelia Voiculescu<sup>2</sup>

<sup>1</sup>. NanCorr Laboratory, University of Las Palmas de Gran Canaria, Las Palmas, Spain.

<sup>2</sup>. Department of Materials Technology and Welding, Politehnica University of Bucharest, Romania.

\* Corresponding author: julia.mirza@ulpgc.es

## Introduction

High entropy alloys are an extremely diverse and interesting class of materials as they are promising materials for a wide range of industrial applications because they are very hard, heat resistant and show great variability in their magnetic behavior [1,2].

High entropy alloys or HEAs consist of five or more different metallic elements; since their macroscopic properties are highly dependent on interatomic interactions, it is of great interest to probe the local structure and structural disorder around each individual element [3,4].

In recent years, the well-known Cantor alloy (CoCrFeMnNi) has attracted considerable attention due to its excellent toughness and fracture strength but its corrosion resistance is very low because Mn interferes with the passivation process and therefore, in our study we have considered an HEA in which Mn has been replaced with Mo (CoCrFeMoNi). To further improve the properties, the alloy obtained has been microalloyed with titanium.

## Experimental

The ingots of each alloy are prepared at LAMET laboratory, Romania, by Vacuum Arc Melting (VAR) in a protective argon atmosphere by using the MRF ABJ 900 VAR equipment and eight remelting operations are carried out for complete homogenization.

The raw materials used to form these alloys are 99.00 % pure and the obtained alloys have the composition wt % and at % shown in Table 1. One of the samples, CoCrFeMoNi (named HEA) and that with Ti doping was named (HEATi).

**Table 1.** Chemical composition of the experimental samples

Element	wt %		at %	
	HEA	HEATi	HEA	HEATi
Co	20.67	20.09	21.52	21.09
Cr	19.99	19.04	23.58	22.67
Fe	19.88	19.29	21.84	21.37
Mo	20.20	22.10	12.92	14.26
Ni	19.27	19.20	20.14	20.24
Ti	-	0.28	-	0.36

The samples with and without Ti are compared: their microstructure is analyzed by optical microscopy (Olympus BX5, Japan), SEM and EDS (HITACHI TM3030); the modulus of elasticity of the alloys was

studied by a three-point bending test (Electroforce 3100 BOSE Corporation, USA) and their electrochemical responses, by linear polarization (LP) and electrochemical impedance spectroscopy (EIS) using a SP-150 potentiostat (BioLogic, France). The hardness was measured with Shimadzu HMV2T microhardness apparatus (Tokyo, Japan). The samples preparation and analysis is shown in Figure 1.

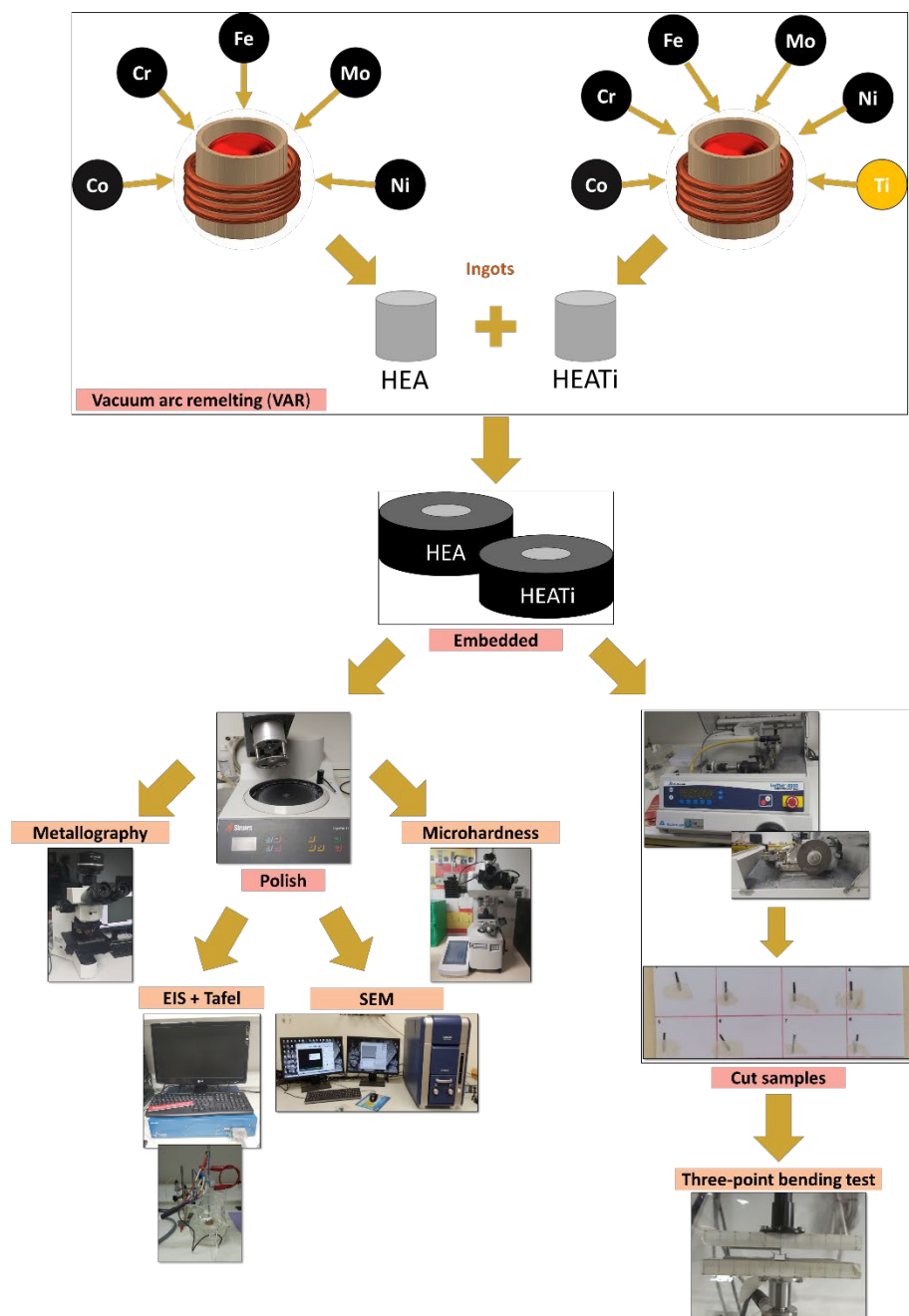


**Figure 1.** Schematic preparation and analysis of the samples.

## Results and discussion

### a) Microstructure

The optical examination after electrochemical etching is shown a dendritic structure for both samples (See Figure 2)

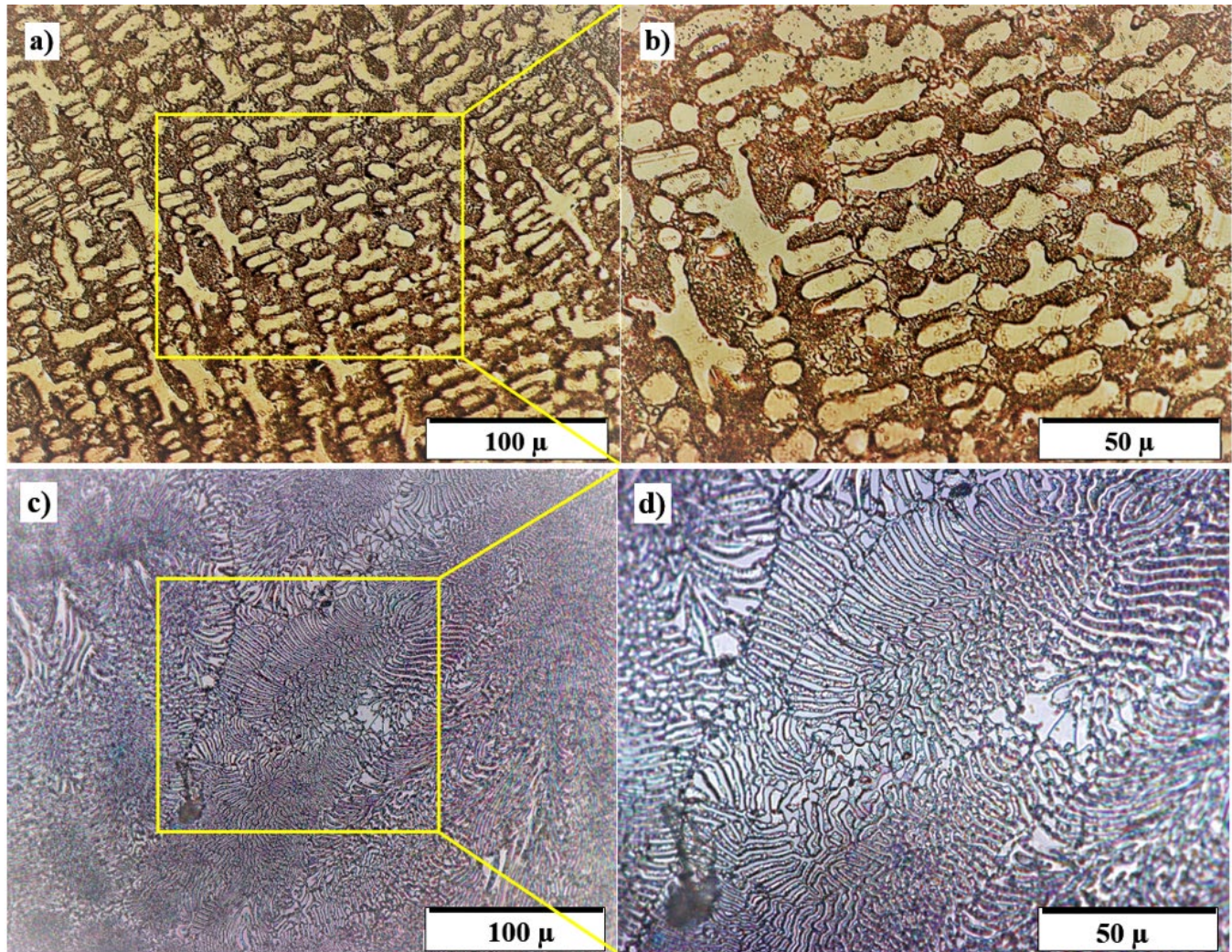


**Figure 2.** a, b) Microstructure of HEA and c,d) HEATi after electrochemical etching.

The microstructures were also analyzed by scanning electron microscopy and the compositions were determined by EDS.

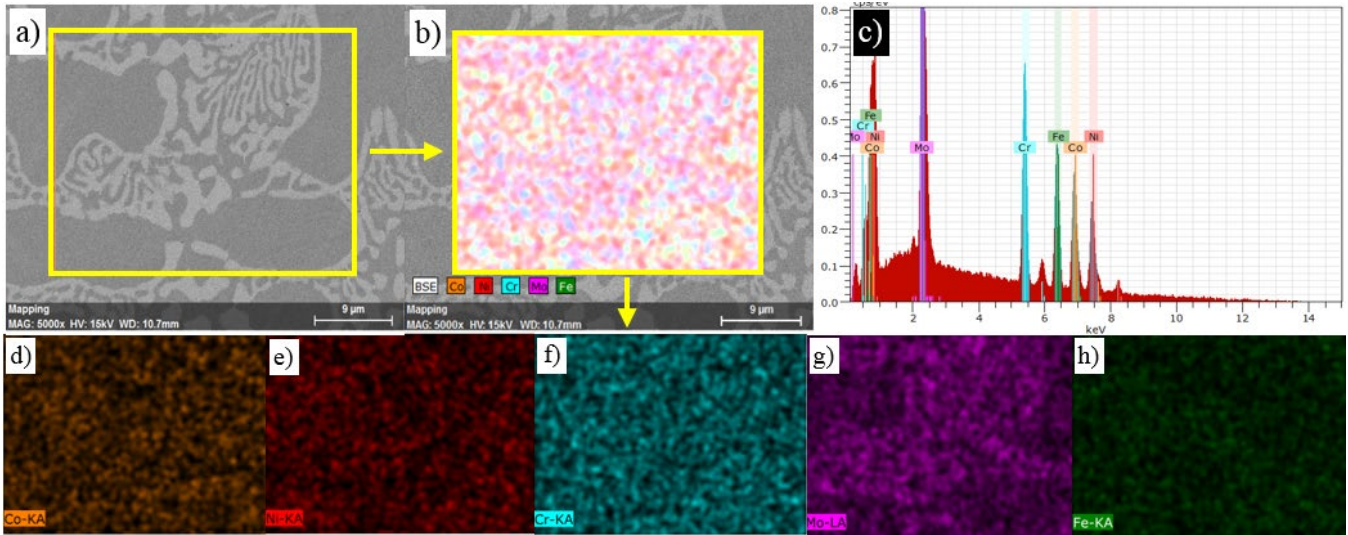


**Figure 3.** Imagen EDS y zona marcada con la selección del mapeo, (a,b), líneas espectrales de los elemento de la aleación (c) e imágenes de mapeo de los elementos de la HEA, (d to h).

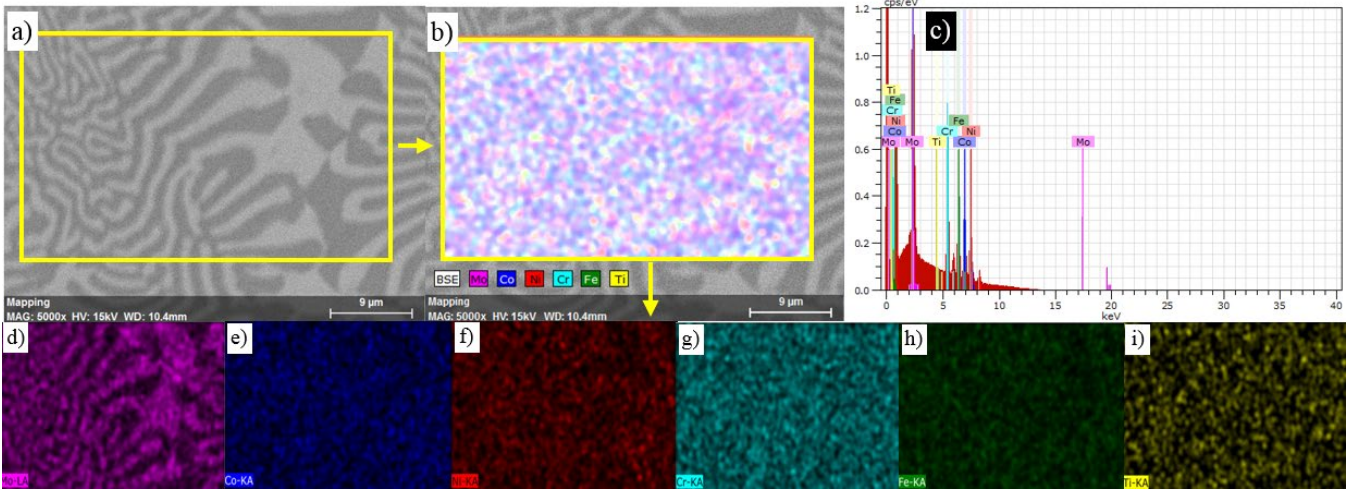


**Figure 4.** Imagen EDS y zona marcada con la selección del mapeo, (a,b), líneas espectrales de los elemento de la aleación (c) e imágenes de mapeo de los elementos de la HEATi, (d to i).

b) Elastic modulus and hardness

The elastic modulus was determined and the hardness of both samples was calculated and the results are shown in Table 2. It can be observed that the elastic modulus is similar, but the hardness of Ti-doped sample is improved.

**Table 2.** Elastic modulus and hardness of the samples

	Elastic modulus (MPa)	Hardness HV0.2
HEA	173.99 ± 4.25	369.20 ± 0.56
HEATi	177.89 ± 3.69	450.90 ± 0.50

b) Electrochemical behavior

Figure 5 illustrates the potentiodynamic polarization curves of HEA and HEATi in 3.5 wt.% NaCl solution at 25°C. The results show that both samples exhibit active dissolution starting at aprox. 0V and almost could not passivate in sodium chloride solution.

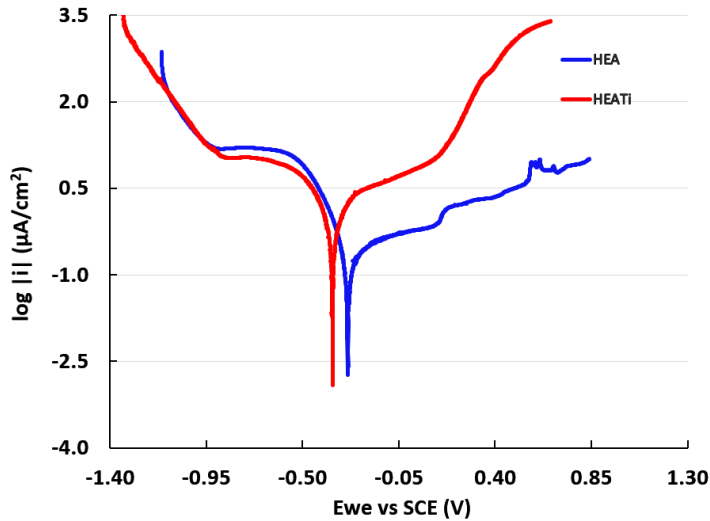


Figure 5. Potentiodynamic polarization curves.

The graphs obtained from the EIS tests are presented in Figure 6 for HEA and in Figure 7 for HEATi. As can be observed in the Nyquist plots presented in Figure 6, and Figure 7, the radius of the semicircle for HEATi is smaller than for HEA, which indicates a low polarization resistance (a low corrosion resistance) for HEATi.

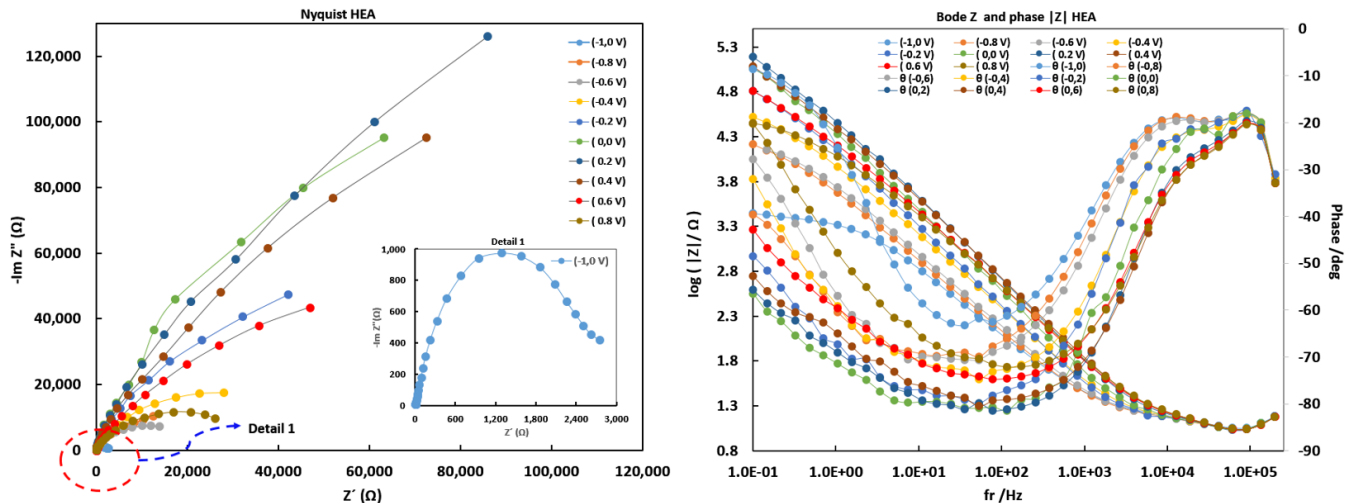
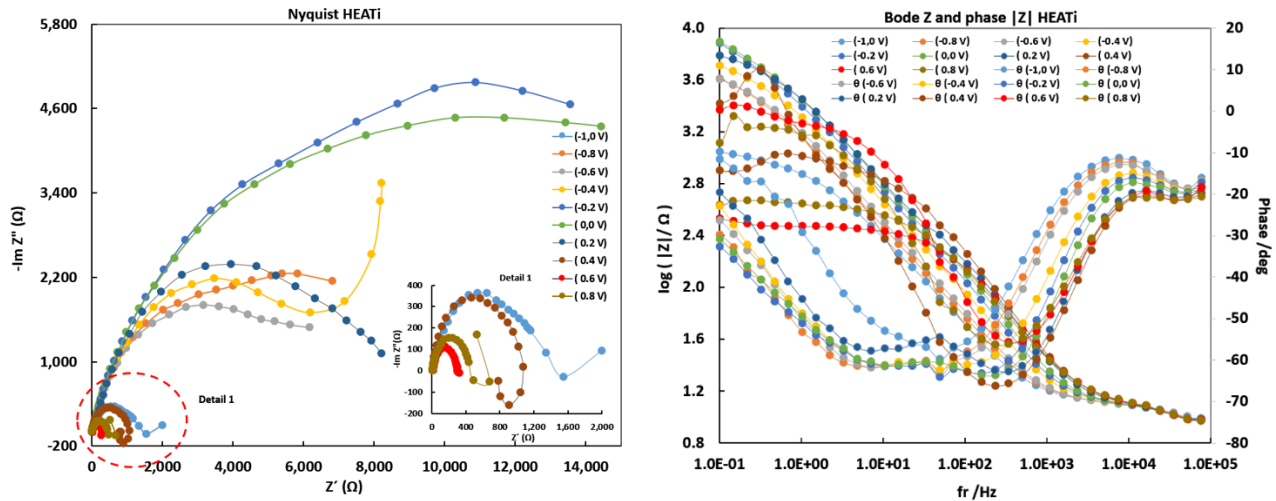


Figure 6. EIS graphs for the HEA sample.



**Figure 7.** EIS graphs for the HEATi sample.

## Conclusions

The effects of titanium doping on the microstructure, elastic modulus, hardness and corrosion properties of CoCrFeNiMo high entropy alloy has been investigated. Simulated corrosive solution of 3.5wt.%NaCl was used to characterize the corrosion behavior of these materials by electrochemical techniques.

- Both alloys exhibited a compact microstructure, with no cracks, porosity or other defects.
- The alloy without titanium is more resistant to corrosion, with a very low corrosion rate.
- The resistance of the passive film decreases with the addition of Ti due to the increasing of the number of defects points in the film. Without Ti the passive layer that forms on the surface of the alloy is more compact and protective.

## Acknowledgements

The research was supported by Cabildo de Gran Canaria, project number CABINFR2019-07.

## References

- [1]. Florido-Suarez, N.; Socorro-Perdomo, P.; Geanta, V.; Mirza-Rosca, J. Static Testing and Fatigue Behavior of Three High-Entropy Alloys. *Microsc. Microanal.* **2021**, *27*, 3270–3271, doi:10.1017/s1431927621011260.
- [2]. Socorro-Perdomo, P.; Florido-Suarez, N.; Voiculescu, I.; Mirza-Rosca, J. Biocompatibility of New High-Entropy Alloys with Non-Cytotoxic Elements. *Microsc. Microanal.* **2021**, *27*, 1772–1774, doi:10.1017/s1431927621006486.
- [3]. López Ríos, M.; Socorro Perdomo, P.P.; Voiculescu, I.; Geanta, V.; Crăciun, V.; Boerasu, I.; Mirza Rosca, J.C. Effects of nickel content on the microstructure, microhardness and corrosion behavior of high-entropy AlCoCrFeNi<sub>x</sub> alloys. *Sci. Rep.* **2020**, *10*, 1–11, doi:10.1038/s41598-020-78108-5.
- [4]. Socorro-Perdomo, P.P.; Florido-Suárez, N.R.; Voiculescu, I.; Mirza-Rosca, J.C. Comparative eis study of alxcoacrfeNi alloys in ringer's solution for medical instruments. *Metals (Basel).* **2021**, *11*, doi:10.3390/met11060928.



[www.microscopy.org/MandM/2023](http://www.microscopy.org/MandM/2023)  
for up-to-date meeting information

# CALL FOR PAPERS

Submission Deadline: **February 16, 2023**



**M&M 2023**  
**MICROSCOPY &  
MICROANALYSIS**  
Minneapolis, MN • July 23-27



# An Investigation of Elastic Modulus in Zr Doped CoCrFeMoNi HEA by Three-Point Bending

Santiago Brito-García<sup>1</sup>, Cristina Jiménez-Marcos<sup>1</sup>, Julia Mirza-Rosca<sup>1\*</sup> and Ionelia Voiculescu<sup>2</sup>

<sup>1</sup>. NanCorr Laboratory, University of Las Palmas de Gran Canaria, Las Palmas, Spain.

<sup>2</sup>. Department of Materials Technology and Welding, Politehnica University of Bucharest, Romania.

\* Corresponding author: julia.mirza@ulpgc.es

## Introduction

In recent years there has been a great interest in high entropy alloys (HEAs) since they have good mechanical properties, high corrosion resistance and good thermal conductivity among others, which makes them interesting for various fields of research. For this reason, it is important to know their behavior in different conditions that allows us to define the possible applications of these HEA's [1–3]. The literature has been confirming the effect of doping with different elements in the improvement of the mechanical properties and corrosion resistance of HEA's [4]. One of the aspects to be considered in the mechanical properties of a HEA is the strength and fracture toughness of the alloy. These mechanical characteristics are related to the value of the modulus of elasticity (E) of the alloy, which provides information on the cohesion of the material as it is related to the binding energy of the atoms. To calculate the modulus of elasticity of the prepared alloys, a three-point bending test is performed on fibers of the material.

## Experimental

A non-equiatomic high entropy alloy is made with the elements: Co, Cr, Fe, Mo and Ni of chemical composition in percent by weight, wt %, of 20.67, 19.99, 19.88, 20.20 and 19.27 respectively, which we call Sample 1. From this alloy a second one, Sample 2, is obtained by doping with 0.71%wt. Zr. Two ingots are manufactured with high purity elements, 99.00%, in an arc melting furnace model MRF ABJ 900 VAR in a protective argon atmosphere. Six remelting operations are carried out on each ingot to achieve a good homogenization. To obtain an average value of the modulus of elasticity, 10 fibers obtained with a Buehler IsoMet® 4000 precision linear saw machine using 0.5 mm thick tungsten disks are made from the specimens. The fibers have a rectangular section with an average thickness of 0.45 mm and variable length. A three-point bending test is performed in an Electroforce 3100 universal testing machine providing a maximum force (F) of 22N. The fibers are placed in the bending test fixture, see Figure 1a, and a vertical force is applied at its midpoint until the strand breaks, as in Figure 1b, or the maximum force is reached. Finally, an analysis of the breakage zones is performed by electron fractography using a Sigma 300 VP field emission scanning electron microscope (FESEM). The observation is performed with the secondary electron detector (SE) at 15 kV at different magnifications.

## Results and discussion

With the data obtained in the three-point bending test, the force (F) displacement (w) graphs are generated (see Figure 2). From the straight line obtained in the elastic zone, we take its slope and calculate the modulus of elasticity as  $dF/dw = 48EI/L^3$ , where E is the modulus of elasticity, I is the moment of inertia of the rectangular section and L is the length between supports.

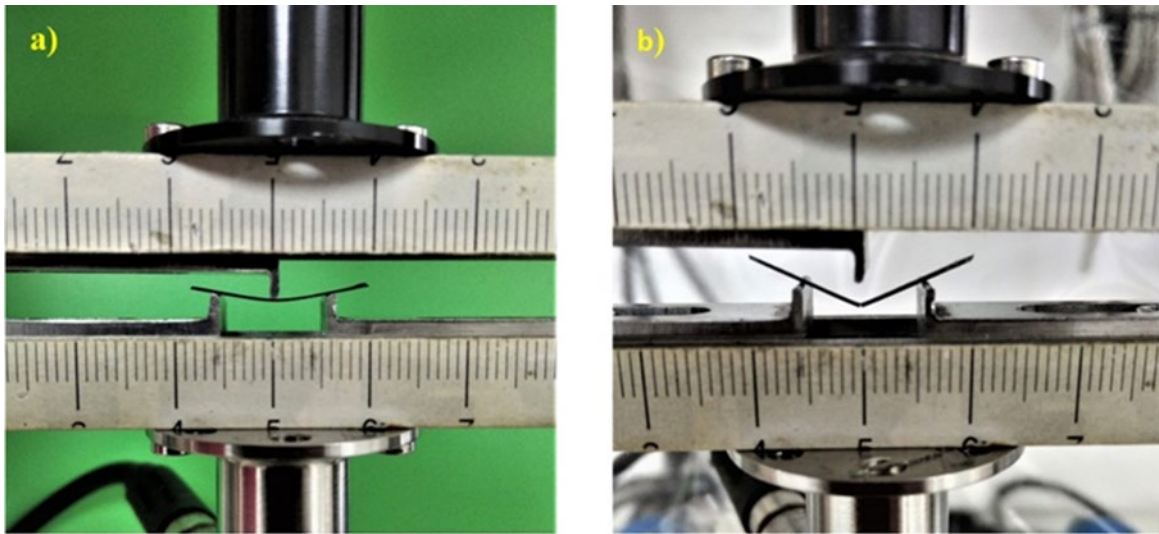


**Figure 1.** a) Three-point bending test of one of the specimens and b) detail of the fracture of one of the specimens.

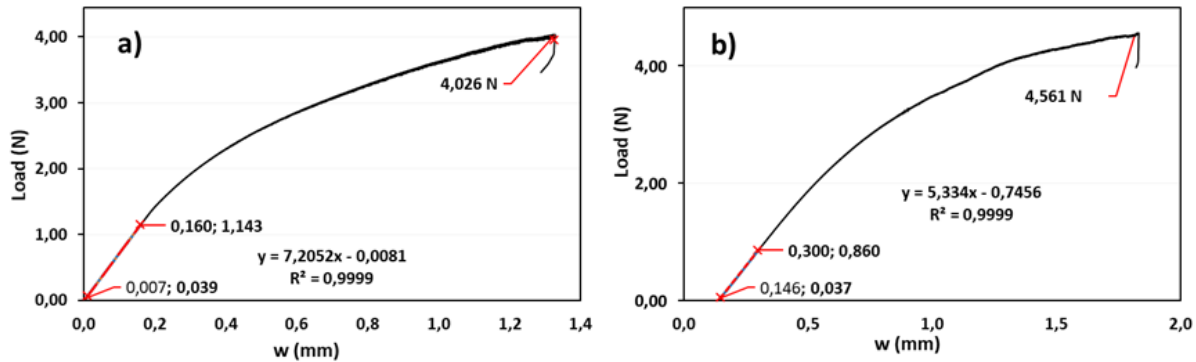


**Figure 2.** Three-point flexural test diagrams for: a) Sample 1 and b) Sample 2.

For Sample 1 a value of E of  $173.99 \pm 4.25$  GPa is obtained and for Sample 2 the calculated value is  $144.33 \pm 5.38$  GPa. The value obtained for the sample with Zr is 20.5% lower than for the sample without the addition of Zr which causes a decrease in the stiffness of the alloy.

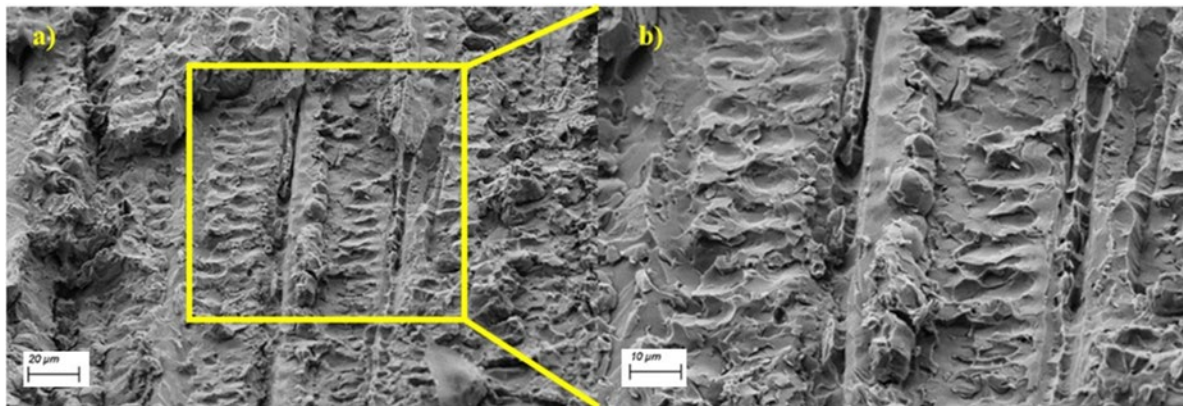


**Figure 3.** FESEM image of the a) fracture surface of Sample1 and b) detail of the marked zone.

In the FESEM micrographs of the samples, Figure 3 and Figure 4, it can be seen how on the surface of Sample 1 there are fracture planes that indicate a brittle fracture of the material and, on contrary, on the surface of Sample 2 there are small dimples characteristic of a material that presents certain ductility.

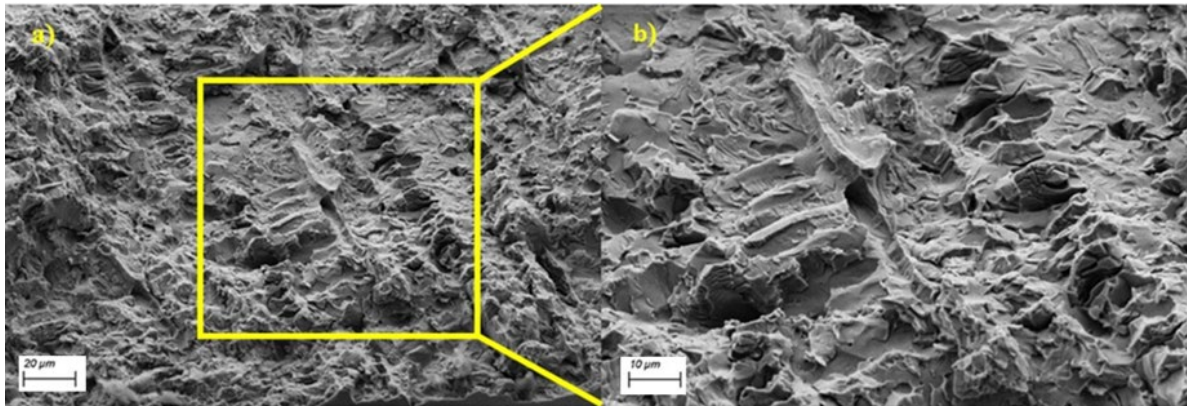


**Figure 4.** FESEM image of the a) fracture surface of Sample1 and b) detail of the marked zone.

## Conclusions

In this work a high entropy alloy from CoCrFeMoNi system and then doped by 0.71 wt% Zr were fabricated by vacuum arc melting. FESEM and three-points bending tests were performed to analyze the fracture surface and to evaluate the elastic modulus. It was determined that the doping with only 0.71 wt% Zr, the elastic modulus decreased with more than 20% and this is associated with great strength, high elasticity and high wear resistance.

## Acknowledgements

The research was supported by Cabildo de Gran Canaria, project number CABINFR2019-07.

## References

- [1] Rios, M.L.; Baldevenites, V.L.; Voiculescu, I.; Rosca, J.M. AlCoCrFeNi High Entropy Alloys as Possible Nuclear Materials. *Microsc. Microanal.* 2020, doi:10.1017/s1431927620014555.
- [2] Socorro-Perdomo, P.P.; Florido-Suárez, N.R.; Voiculescu, I.; Mirza-Rosca, J.C. Comparative eis study of alxcoerfeni alloys in ringer's solution for medical instruments. *Metals (Basel)*. 2021, 11, doi: 10.3390/met11060928
- [3] Geanta, V.; Voiculescu, I.; Vizureanu, P.; Victor Sandu, A. High Entropy Alloys for Medical Applications. *Eng. Steels High Entropy-Alloys 2020*, 4–12, doi:10.5772/intechopen.89318.
- [4] Wang, R.; Tang, Y.; Lei, Z.; Ai, Y.; Tong, Z.; Li, S.; Ye, Y.; Bai, S. Achieving high strength and ductility in nitrogen-doped refractory high-entropy alloys. *Mater. Des.* 2022, 213, 110356, doi:10.1016/j.matdes.2021.110356.



**Uluslararası Bilimsel Araştırmalar ve  
Yenilikçi Çalışmalar Sempozyumu**

**International Symposium of Scientific  
Research and Innovative Studies**



**ÖZET BİLDİRİLER KİTABI  
ABSTRACTS BOOK**

**22-25 ŞUBAT 2021**

**22-25 February 2021**

**ISBN: 978-625-44365-8-1**





**Uluslararası Bilimsel Araştırmalar ve Yenilikçi  
Çalışmalar Sempozyumu**  
**International Symposium of Scientific Research and  
Innovative Studies**



**A STUDY OF METALLIC GLASS  $Al_3Ti_3Cr_2Fe_3$  FOR BIOMEDICAL  
APPLICATIONS**

S.J. Brito-Garcia<sup>1</sup>, P.P. Socorro-Perdomo<sup>1</sup>, N.R. Florido-Suarez<sup>1</sup>, T. Gil-Lopez<sup>2</sup>, J.C. Mirza-Rosca<sup>1\*</sup>

<sup>1</sup>University of Las Palmas de Gran Canaria, Campus Tafira, Edificio Ingeniería, 35017, SPAIN

<sup>2</sup>Madrid Polytechnic University, Department of Building Technology, Madrid 28040, SPAIN

[julia.mirza@ulpgc.es](mailto:julia.mirza@ulpgc.es)

Corresponding Author ORCID: 0000-0003-0623-3318

**ABSTRACT**

**Introduction**

Metallic glasses are those which share the properties of both metals and glasses. As promising materials for different applications, metallic glasses are preferred over metals, ceramics, magnetic and some other types of existing materials due to their enhanced properties. Some of the important reasons for which we consider these glasses for specific application like biomaterials are discussed in this study.

**Purpose**

A study of two samples with the same chemical composition,  $Al_3Ti_3Cr_2Fe_3$ , produced by the "Metal spinning cooling" method but cooled at different speeds of the rotating wheel: one at 1700 rpm (which we call Al - 17) and the other at 2500 rpm (which we call Al - 25), is carried out to evaluate the possible biomedical applications. The thin film samples have thicknesses of less than 20µm and widths of no more than 5mm.

**Experimental**

For their characterization, mechanical and electrochemical tests are carried out, which will allow to know the main properties of the material in order to decide the possible biomedical applications of the alloys. A tensile test will be carried out to calculate the Young's modulus of elasticity and the tensile strength, a metallographic study in order to define the characteristics

of the microscopic structure of the alloys and, finally, corrosion tests, for the corrosion potential and corrosion rate determinations.

## **Results**

To calculate the Young's modulus of elasticity  $E$ , the graphs are obtained with the values of each of the tested specimens. A rectilinear section of the graph is selected and we calculate the linear dispersion equation  $y = ax + b$  where 'a' represents the slope of the line and gives us the  $E$  value. Finally, the coefficient of determination  $R^2$  is calculated to verify the optimality of the model used. In all cases the value of  $R^2$  is above 0.99 so we can say that the model fits more than 99% of the calculated variable. The corrosion tests are performed in Ringer's solution, which simulates the physiological fluid of the human body. An open circuit potential test is performed and the evolution of the potential  $E$  is represented with respect to time and the profile of the obtained curve will allow us to know the tendency to passivation or to corrosion of each sample. A linear polarization is performed on each specimen in the electrolytic cell. The data are processed in the Ec-Lab program obtaining the values of corrosion current  $I_{\text{corr}}$  and the Tafel coefficients  $\beta_a$  and  $\beta_c$  from which the corrosion rate is calculated in mmpy.

## **Conclusions**

The values of the tensile strength  $\sigma_{\text{ten}}$  can be considered low in comparison with other alloys used as titanium-based biomaterials or stainless steels, although in none of the two metallic glass samples studied is this value lower than that of cortical bone (50 - 150 MPa). To highlight the average value obtained for the  $\sigma_{\text{ten}}$  for the Al-25 sample, which is of the order of 2.2 times that of Al-17. In all the microphotographs taken of the metallic glass samples, without attack and with the attacks carried out with hydrofluoric acid, a non-crystalline structure is observed, as is to be expected in a material with a glassy structure. The samples studied show good corrosion behavior, although they show a notable increase in corrosion rate when tested at body temperature (40°C). Comparing the corrosion rate between the samples Al-17 and Al-25 at each temperature analyzed, it is observed that Al-17 at room temperature has a corrosion rate increase of about 4.5 times with respect to the corrosion rate of Al-25. It is concluded that the Al-25 sample presents a better behavior as biomaterial due to the higher mechanical resistance, a low Young's modulus and a lower corrosion rate. The metallographic study confirms the amorphous structure of the samples, in none of the micrographs crystalline structures are observed.

**Keywords:** *Metallic glass, Tensile strength, Corrosion*



**Uluslararası Bilimsel Araştırmalar ve  
Yenilikçi Çalışmalar Sempozyumu**

**International Symposium of Scientific  
Research and Innovative Studies**



**ÖZET BİLDİRİLER KİTABI  
ABSTRACTS BOOK**

**22-25 ŞUBAT 2021**

**22-25 February 2021**

**ISBN: 978-625-44365-8-1**





**Uluslararası Bilimsel Araştırmalar ve Yenilikçi  
Çalışmalar Sempozyumu**  
**International Symposium of Scientific Research and  
Innovative Studies**



**ELECTRONIC POWER SYSTEM FOR THE DYNAMIC CORROSION  
CONTROL**

J.M. Cabrera-Peña, N.R. Florido-Suarez\*, P.P. Socorro-Perdomo, S.J. Brito-García, J.C. Mirza-Rosca

*University of Las Palmas de Gran Canaria, Campus Tafira, Edificio Ingeniería, 35017, SPAIN*

[nestor.florido@ulpgc.es](mailto:nestor.florido@ulpgc.es)

*Corresponding Author ORCID: 0000-0002-1824-6792*

**ABSTRACT**

**Introduction**

Corrosion is currently a worldwide source of economic, material, environmental damage and in the worst case, even human loss due to corrosion in infrastructure. To combat it there are a variety of techniques and treatments, but even applying them in their strictest form, sooner or later, the phenomenon cannot be avoided. Cathodic protection is a technique used to control the corrosion of a metal surface by making it the cathode of an electrochemical cell. Impressed current cathodic protection systems consist of anodes that are connected to a power source that provides a perpetual source of electrical flow. This method can often provide much longer protection than a sacrificial anode, as the anode is supplied by an unlimited power source.

**Purpose**

The objective is the study, design and elaboration of the prototype, continuing a preliminary study called "Study of the protection against corrosion of a metallic structure" in order to introduce modifications and improvements to the prototype to allow to overcome corrosion in metallic structures.

**Experimental**

Therefore it is proposed a prototype based on cathodic protection is proposed, since it is defined as the method to reduce or eliminate the corrosion of a metal. To do this, the surface



must be made to function as a cathode when it is in an electrolyte, that is, a medium, whether aquatic, atmospheric or terrestrial. This is done by impressed current cathodic protection. Continuing with an already open line of research, design of a prototype starting from a DC - DC Buck - Boost converter to which a closed loop power system is incorporated, thus allowing control of the printing current and the relative humidity of the environment through of a voltage and humidity sensor, respectively.

For the characterization and viability of the prototype, different tests are carried out, among them, it tested in a salt spray chamber using steel specimens to test for corrosion by generation of an adverse environment in an accelerated manner.

### **Results and discussion**

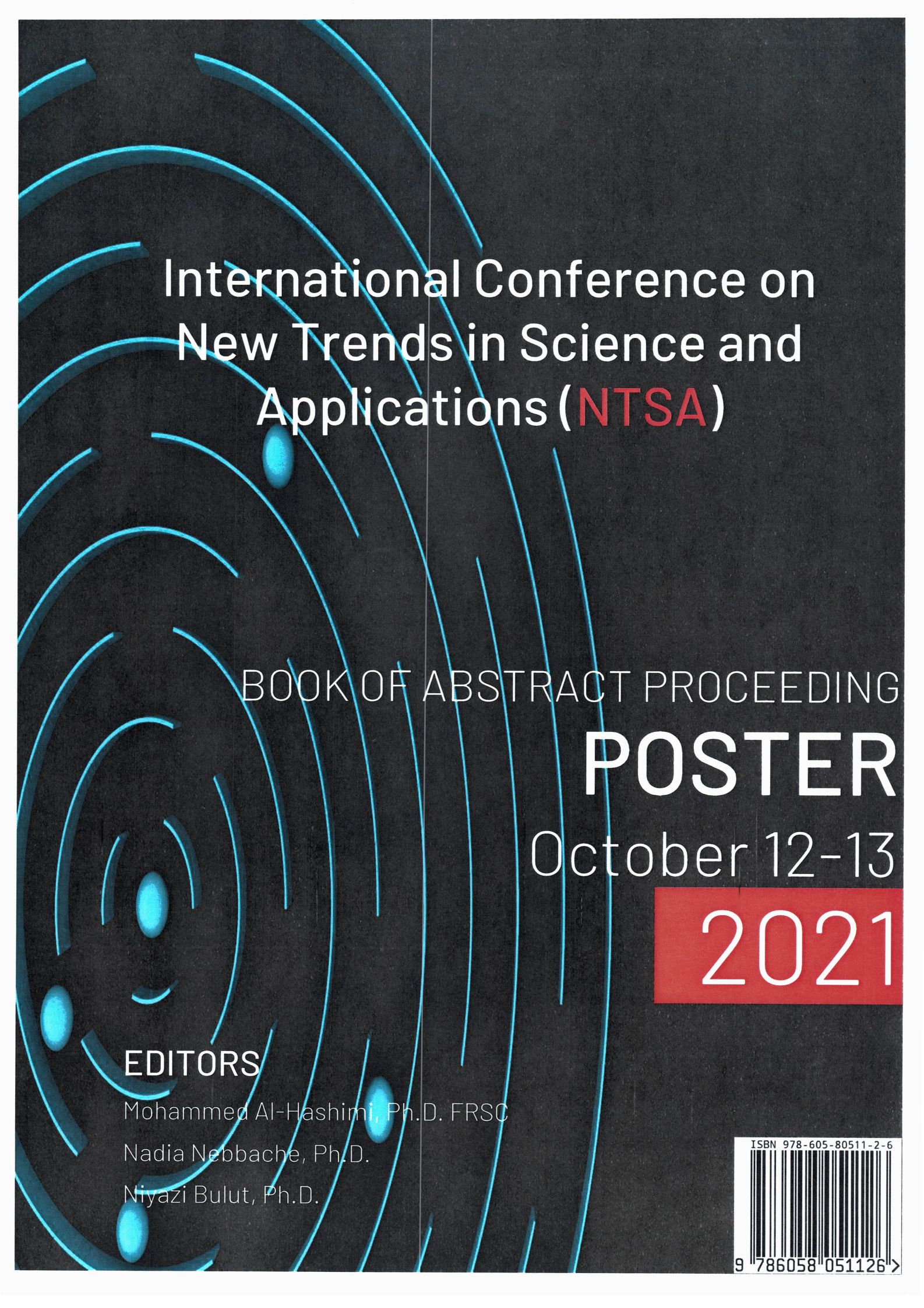
The conditions of the test, suppose an extreme reproduction to which any structure could face against the corrosion, the commutation between the values of intensity of polarization and maintenance can take a second plane, reason why all the attention was focused on the verification whether the current protection technique printed with the values calculated on the bias current during this line of research were capable of correctly protecting. When conducting the test using the impressed current technique, it was done with a zinc anode, a material that is not recommended for this type of protection due to its rapid consumption, which is why it has been changed in the current study for the installation of platinum anodes. The specific details of how structures are constructed can also add to the complexity — and therefore cost — of cathodic protection. In addition to this cost, the system also requires routine maintenance, including periodic visual inspection. In the case of impressed current cathodic protection there is also the ongoing cost of electricity. Sacrificial anodes in particular have a limited amount of current available, are subject to rapid corrosion, and therefore have a limited lifespan.

### **Conclusions**

In conclusion, the design proposed for the device has flaws, so it would represent a new line of research open to optimization. Regarding the tests carried out in a saline mist chamber, they proved that a greater resistance to corrosion is achieved than that obtained with the control specimen, so that different ways of applying it could be analyzed. At the same time, it is interesting to continue with the use of the new tests on the cathodic protection technique by impressed current.

**Keywords:** *Corrosion, Cathodic Protection, Prototype*





# International Conference on New Trends in Science and Applications (NTSA)

BOOK OF ABSTRACT PROCEEDING

# POSTER

October 12-13

2021

## EDITORS

Mohammed Al-Hashimi, Ph.D. FRSC

Nadia Nebbache, Ph.D.

Niyazi Bulut, Ph.D.

ISBN 978-605-80511-2-6



9 786058 051126 >



**PP-28****Mechanical Behavior of Three High Entropy Alloys (HEA) for Possible Use as Biomaterials**

S.J. Brito-García<sup>1</sup>, N. Florido-Suárez<sup>1</sup>, P. Socorro-Perdomo<sup>1</sup>, I. Voiculescu<sup>2</sup>, J.C. Mirza-Rosca<sup>1\*</sup>

<sup>1</sup> *Mechanical Engineering Department, University of Las Palmas de Gran Canaria*

<sup>2</sup> *Politehnica University of Bucharest, Bucharest, Romania*

Orcid: 0000-0003-0623-3318

julia.mirza@ulpgc.es

**Introduction**

High entropy alloys (HEA) are the new class of materials whose research has been developing in the last 17 years after Cantor et al. and Yeh et al. published their work in 2004. These materials have unique structural properties that open up a wide range of possibilities for the creation and development of novel materials for specific applications [1]. In the medical field, HEAs have been developed for metallic devices, in various alloy systems, where biocompatibility and mechanical properties are essential conditions [2].

**Experimental methods and results**

A base alloy is designed, a high entropy equiatomic multicomponent alloy with pure elements (99.95%), formed by the system Cr, Co, Fe, Mo and Ni (LAS1) and from this alloy two other alloys are obtained by adding another component to the alloy. In one alloy, Ti is added (LAS2) and in the other Zr is added (LAS3) in order to study the mechanical behavior that allows us to consider its use as a biomaterial. An ingot of each of these alloys is fabricated by vacuum arc melting in an inert argon atmosphere and six remeltings are carried out to ensure their homogeneity. By means of a three-point bending test, the modulus of elasticity E is calculated. For this purpose, filaments are cut and tested in an Electroforce\_3100 machine that applies a maximum load of 22 Newton. At least 10 tests are performed with each of the designed alloys and the mean,  $\bar{x}$  of the obtained values and the standard deviation sm are calculated.

**Conclusions**

Compared to the base sample LAS1, the modulus of elasticity increases slightly with the contribution of Ti, alloy LAS2, while the alloy LAS3 with the contribution of Zr, has a significant decrease in the value of the modulus of elasticity, which makes it interesting to carry out future research in this line of work.

**References**

- [1] Socorro-Perdomo, P.P.; Florido-Suárez, N.R.; Voiculescu, I.; Mirza-Rosca, J.C. Comparative eis study of alxcocrfeni alloys in ringer's solution for medical instruments. *Metals* (Basel). 2021, 11, doi:10.3390/met11060928.
- [2] López Ríos, M.; Socorro Perdomo, P.P.; Voiculescu, I.; Geanta, V.; Crăciun, V.; Boerasu, I.; Mirza Rosca, J.C. Effects of nickel content on the microstructure, microhardness and corrosion behavior of high-entropy AlCoCrFeNi<sub>x</sub> alloys. *Sci. Rep.* 2020, 10, 1–11, doi:10.1038/s41598-020-78108-5.



## Book of Abstracts

# EUROINVENT ICIR 2022

## International Conference on Innovative Research

**May 26<sup>th</sup> to 27<sup>th</sup>, 2022**

Iasi – Romania

**Organized by:**

- Romanian Inventors Forum
- Faculty of Materials Science and Engineering, The “Gheorghe Asachi” Technical University of Iasi, Romania
- ARHEOINVEST Platform, Alexandru Ioan Cuza University of Iasi
- Centre of Excellence Geopolymer and Green Technology CEGeoGTech), Universiti Malaysia Perlis (UniMAP)
- Department of Physics, Czestochowa University of Technology, Czestochowa, Poland

**With support of:**

- Universiti Malaysia Terengganu
- International Federation of Inventors' Associations - IFIA
- World Invention Intellectual Property Associations – WIIPA

**Editors:**

Andrei Victor SANDU, Mohd Mustafa Al Bakri ABDULLAH,

Petrică VIZUREANU, Marcin NABIALEK, Che Mohd Ruzaidi GHAZALI, Ion SANDU

ISSN Print 2601-4580

ISSN On-line 2601-4599

**Editors:**

Andrei Victor SANDU

Mohd Mustafa Al Bakri ABDULLAH

Petrică VIZUREANU

Marcin NABIALEK

Che Mohd Ruzaidi GHAZALI

Ion SANDU

Technical Editors:

Lecturer PhD.Eng. Manuela Cristina PERJU

Lecturer PhD.Eng. Dragos Cristian ACHITEI

Assist. PhD.Eng. Diana Petronela BURDUHOS NERGIS

Assist. PhD.Eng. Dumitru Doru BURDUHOS NERGIS

Copyright © 2022  
All Rights reserved to the Editors

All the abstracts are provided by the authors.  
No major corrections were applied by editor.

# Mechanical and Corrosion Behaviour of Two High Entropy Alloys (HEA) for Medical Applications

Santiago BRITO-GARCIA<sup>1</sup>, Julia MIRZA-ROSCA<sup>1,\*</sup>,  
Ionelia VOICULESCU<sup>2</sup>

<sup>1</sup> Mechanical Engineering Department, University of Las Palmas de Gran Canaria, Juan de Quesada street, 30, 35001, Las Palmas de Gran Canaria, España

<sup>2</sup> Faculty of Industrial Engineering and Robotics, Politehnica University of Bucharest, 313 Splaiul Independentei, 060042, Bucharest, Romania  
\*Julia.mirza@ulpgc.es

---

**Abstract.** A base alloy is designed, a high entropy multicomponent equiatomic alloy with pure elements (99.95%), formed by the Cr, Co, Fe, Mo and Ni system, LAS1, and from this alloy a new alloy is obtained by adding one more element, Zr, which we call LAS3. Both alloys were remelted by voltaic arc (VAR), to study the mechanical and corrosion behavior that allows us to consider its use as a medical material. One ingot of each alloy is produced by arc melting in an inert argon atmosphere [1] and six remelting operations are performed on each of these alloys to ensure homogeneity. The modulus of elasticity E of each of these alloys is calculated by a three-point bending test. For this purpose, strands are cut from each of the samples and tested in an Electroforce\_3100 machine applying a maximum load of 22 Newton. At least 10 tests are carried out with each of the alloys designed, the mean,  $\bar{x}$  of the values obtained is calculated, as well as the standard deviation m. A linear polarization test is also carried out to calculate the corrosion rate. A BioLogic SP\_150 potentiostat is used and for the electrochemical tests a 3.5 wt.% NaCl is employed. Beforehand, the samples are subjected to an open-circuit potential for 24 hours and also to Electrochemical Impedance Spectroscopy [2].

**Keywords:** High entropy alloy, corrosion, three-point flexion, arc melting

---

## References:

- [1] M. López Ríos *et al.*, "Effects of nickel content on the microstructure, microhardness and corrosion behavior of high-entropy AlCoCrFeNi<sub>x</sub> alloys," *Sci. Rep.*, vol. 10, no. 1, pp. 1–11, 2020, doi: 10.1038/s41598-020-78108-5.
- [2] P. P. Socorro-Perdomo, N. R. Florido-Suárez, I. Voiculescu, and J. C. Mirza-Rosca, "Comparative eis study of alxcocrfeni alloys in ringer's solution for medical instruments," *Metals (Basel)*, vol. 11, no. 6, 2021, doi: 10.3390/met11060928.



---

*28th International Symposium on Analytical and Environmental Problems*

---



***PROCEEDINGS OF THE***

***28<sup>th</sup> International Symposium  
on Analytical and Environmental Problems***

*Szeged, Hungary  
November 14-15, 2022*





## STUDY OF THE METALLOGRAPHIC STRUCTURE OF TWO TITANIUM ALLOYS FOR BIOMEDICAL PROSTHESES

**Héctor Guerra-Yáñez<sup>1</sup>, Santiago José Brito-García<sup>1</sup>, Ionelia Voiculescu<sup>2</sup>, Julia Claudia Mirza-Rosca<sup>1</sup>**

<sup>1</sup>*Mechanical Engineering Department, University of Las Palmas de Gran Canaria, Campus Universitario de Tafira, 35017 Las Palmas de Gran Canaria, Spain*

<sup>2</sup>*Faculty of Industrial Engineering and Robotics, Politehnica University of Bucharest, 313 Splaiul Independentei, 060042 Bucharest, Romania*  
*e-mail: hector.guerra106@alu.ulpgc.es*

### Abstract

The present study has the objective of defining the metallographic structure of two titanium alloys in order to find if they can be used in medical prostheses. The composition of the alloys is: Ti4Fe (93.2% Ti, 4% Fe, 2% Al, 0,8 V) and Ti10Al (89.5% Ti, 0.5% V, 10% Al). For the purpose of obtaining the metallographic structure, it was necessary to use an optic ZESS microscope Axio Vert A1. The materials were initially cut into samples of small volume and covered in epoxy resin in such a way as to leave a controlled surface exposed to the environment [1]. Afterwards the samples were polished and grinded with a Struers polishing machine, SiC papers and an alpha-alumina suspension of 0.1  $\mu\text{m}$  [2]. When this process was finished, the samples were cleaned for preventing possible contaminations that could affect the results. The alloys were then submerged in Kroll reactive for five seconds in order to expose their metallographic structure by acid attack. Shorter immersion times were not sufficient to observe the structure satisfactorily, and longer times caused regions of the alloys to burn.

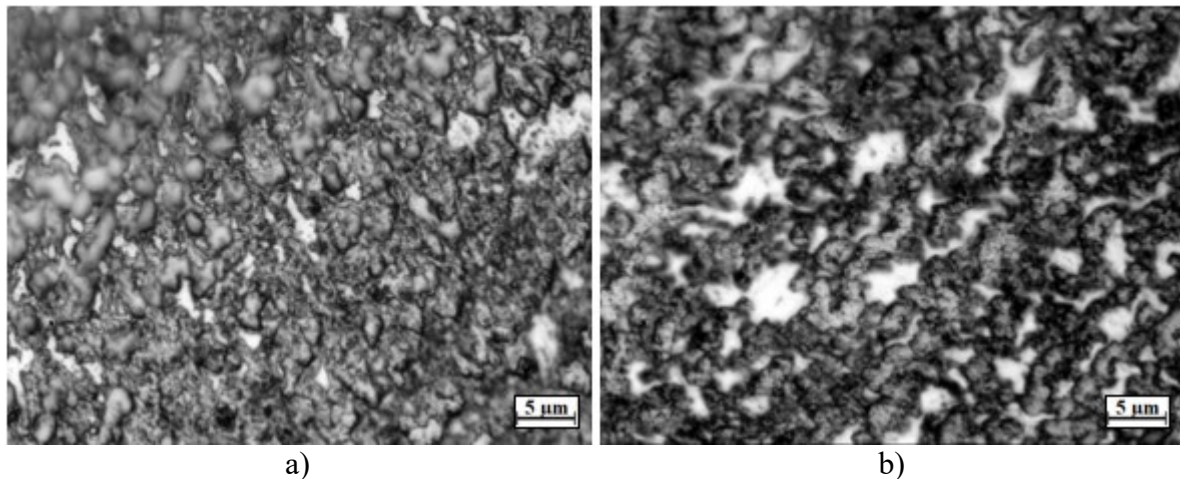


Figure 1. Metallographic structure of alloys Ti4Fe (a) and Ti10Al (b) observed with 100x magnifications.

The presence of the allotropic forms of  $\alpha$ -titanium and  $\beta$ -titanium can be seen in the two images obtained [3], although it is not possible to distinguish which of the regions corresponds to which. If one wanted to obtain this information, it would be necessary to use other tests [4,5]. It can be seen that in the Ti10Al alloy there is a greater presence of burnt regions by the acid attack of the Kroll reactive, although not enough so that the structure cannot be appreciated.

## **Acknowledgements**

The research was sponsored by Gran Canaria Cabildo, project number CABINFR2019-07. The authors gratefully acknowledge the support received from the Romanian National Authority for Scientific Research, CNDI–UEFISCDI, through the project number PN-III-P2-2.1-PED-2019-3953, contract 514PED / 2020 „New ceramic layer composite material processed by laser techniques for corrosion and high temperature applications – LASCERHEA“, Romania.

## **References**

- [1] M. López Ríos, P.P. Socorro Perdomo, I. Voiculescu, V. Geanta, V. Crăciun, I. Boerasu, J.C. Mirza Rosca, *Scientific Reports* 2020 10:1 10 (2020) 1–11.
- [2] P.P. Socorro-Perdomo, N.R. Florido-Suárez, I. Voiculescu, J.C. Mirza-Rosca, *Metals* 2021, Vol. 11, Page 928 11 (2021) 928.
- [3] D.W. Hetzner, W. van Geertruyden, *Mater Charact* 59 (2008) 825–841.
- [4] H.L. Du, P.K. Datta, D.B. Lewis, J.S. Burnell-Gray, *Oxidation of Metals* 45 (1996) 507–527.
- [5] W. Xie, X. Wang, E. Liu, J. Wang, X. Tang, G. Li, J. Zhang, L. Yang, Y. Chai, B. Zhao, *International Journal of Advanced Manufacturing Technology* 119 (2022) 4745–4755.



# ROMAT 2022



**9<sup>th</sup> International Conference on Materials Science  
and Technologies – RoMat 2022**



**Bucharest, Romania  
November 24-25<sup>th</sup>, 2022**



# ROMAT 2022

## Experimental Research on New High Entropy Alloys for Marine Applications

S.J. Brito-Garcia<sup>1</sup>, I. Voiculescu<sup>2</sup>, V. Geanta<sup>2</sup>, J.C. Mirza-Rosca<sup>1\*</sup>

<sup>1</sup>*Mechanical Engineering Department, Las Palmas de Gran Canaria University, 35017 Tafira, Spain;*

<sup>2</sup>*Faculty of Industrial Engineering and Robotics, Politehnica University of Bucharest, 313 Splaiul)*

*\*Corresponding author: [julia.mirza@ulpgc.es](mailto:julia.mirza@ulpgc.es)*

When was published the results of the multicomponent equiatomic alloys which they proposed, eventually called High Entropy Alloys (HEA), many combinations of components have been developed due to their improved properties compared to classic alloys (of a main element with more than 50 at.%).

Two new high entropy alloys were fabricated for this research: one from the system CoCrFeNiMo, and other alloy has the same composition but with Zr additions. They were tested in marine environment. Their microstructure, elastic modulus and corrosion characteristics has been examined in this work. In order to analyze the microstructure of the samples optical microscopy, Scanning Electron Microscopy and Energy-dispersive X-ray spectroscopy were employed; three-point bending test was used to evaluate their modulus of elasticity and linear polarization and electrochemical impedance spectroscopy to examine their electrochemical responses, corrosion kinetics and interface parameters.

**Keywords:** HEA, CoCrFeNiMo, microstructure, Zr, corrosion.





## Book of Abstracts

# EUROINVENT ICIR 2023

## International Conference on Innovative Research

**May 11<sup>th</sup> to 12<sup>th</sup>, 2023**

Iasi – Romania

### Organized by:

- Romanian Inventors Forum
- Faculty of Materials Science and Engineering, The “Gheorghe Asachi” Technical University of Iasi, Romania
- ARHEOINVEST Platform, Alexandru Ioan Cuza University of Iasi
- Centre of Excellence Geopolymer and Green Technology CEGeoGTech), Universiti Malaysia Perlis (UniMAP)
- Department of Physics, Czestochowa University of Technology, Czestochowa, Poland

### With support of:

- Universiti Malaysia Terengganu
- International Federation of Inventors' Associations - IFIA
- World Invention Intellectual Property Associations – WIIPA

### Editors:

Andrei Victor SANDU, Mohd Mustafa Al Bakri ABDULLAH,  
Petrică VIZUREANU, Marcin NABIALEK, Che Mohd Ruzaidi GHAZALI, Ion SANDU



ISSN Print 2601-4580  
ISSN On-line 2601-4599

**Editors:**

Andrei Victor SANDU  
Mohd Mustafa Al Bakri ABDULLAH  
Petrică VIZUREANU  
Marcin NABIALEK  
Che Mohd Ruzaidi GHAZALI  
Ion SANDU

Technical Editors:

Lecturer PhD.Eng. Manuela Cristina PERJU  
Lecturer PhD.Eng. Dragos Cristian ACHITEI  
Assist. PhD.Eng. Diana Petronela BURDUHOS NERGIS  
Assist. PhD.Eng. Dumitru Doru BURDUHOS NERGIS

Copyright © 2023  
All Rights reserved to the Editors

All the abstracts are provided by the authors.  
No major corrections were applied by editor.

# There Are No Limits to the Miracle of Alloys: High Entropy Alloys

Santiago BRITO GARCIA<sup>1</sup>, Julia Claudia MIRZA  
ROSCA<sup>1,\*</sup>, Victor GEANTA<sup>2</sup>, Ionelia VOICULESCU<sup>2</sup>

<sup>1</sup>Mechanical Engineering Department, University of Las Palmas de Gran Canaria,  
Campus Universitario Tafira, Edif. Ingenieria, 35017, Gran Canaria, Spain

<sup>2</sup> Faculty of Industrial Engineering and Robotics, Politehnica University of Bucharest,  
313 Splaiul Independentei, 060042 Bucharest, Romania

[julia.mirza@ulpgc.es](mailto:julia.mirza@ulpgc.es)

---

**Abstract.** The history of metallic alloys dates back to ancient times when humans first learned to extract and work with metals such as copper, tin, and bronze. The earliest known alloy, bronze, was created around 4000 BC by mixing copper with small amounts of tin. Over time, people discovered that by mixing one metal with small quantities of other, they could create alloys with improved properties (iron with small amounts of carbon to create steel).. In the Middle Ages, blacksmiths and metallurgists continued to experiment with different alloys, and many new ones were discovered. In the 18th and 19th centuries, the Industrial Revolution brought about significant advances in metallurgy, and many new alloys were developed. HEAs were first developed in the early 2000s, and they have attracted significant attention from materials scientists and engineers due to their unique properties. Unlike traditional alloys, HEAs have no dominant metal and are instead made up of a mix of multiple metals. This random mixture of metals in HEAs leads to a number of interesting properties, including high strength, high hardness, and good corrosion resistance. HEAs are also highly resistant to deformation and have good thermal stability.

**Keywords:** high entropy alloys, fabrication, microstructure, corrosion.

---

## References:

- [1] López Ríos, M.; Socorro Perdomo, P.P.; Voiculescu, I.; Geanta, V.; Crăciun, V.; Boerasu, I.; Mirza Rosca, J.C. Effects of nickel content on the microstructure, microhardness and corrosion behavior of high-entropy AlCoCrFeNi alloys. *Sci. Rep.* 2020, 10, 1–11, doi:10.1038/s41598-020-78108-5.



# EUROINVENT ICIR 2022

International Conference on Innovative Research

May 26<sup>th</sup> to 27<sup>th</sup>, 2022  
Iasi – Romania



May 26 – 27  
2022

MECHANICAL AND CORROSION BEHAVIOR OF TWO HIGH ENTROPY ALLOYS (HEA) FOR MEDICAL APPLICATIONS



ULPGC  
Universidad de  
Las Palmas de  
Gran Canaria  
CEGeoTech

Santiago J. Brito-García, Julia Mirza-Rosca,  
Mechanical Engineering Department, University of Las Palmas de Gran Canaria

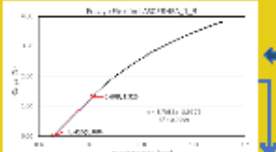
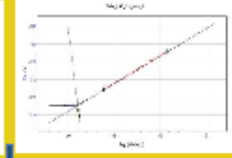
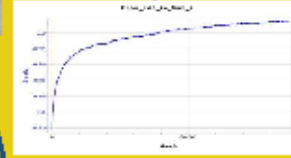
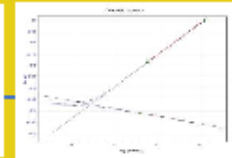
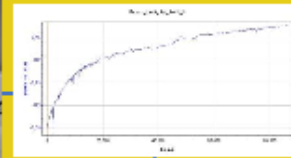
### Introduction

A base alloy is designed, a high entropy equiatomic multicomponent alloy with pure elements (99.95%), formed by the system Cr, Co, Fe, Mo and Ni (LAS1) and from this alloy other alloy is obtained by adding another component to the alloy. In alloy, Ti is added (LAS2) in order to study the mechanical behavior and corrosion behavior.

### Alloys

Chemical Composition	Alloy
Cr, Co, Fe, Mo, Ni	LAS1
Cr, Co, Fe, Mo, Ni, Ti	LAS2

### Techniques



Alcación	E (GPa)
Las1	173.99 ± 4.2%
Las2	177.89 ± 3.68

	$F_{cor}$ (mV)	mm <sup>2</sup> y
LAS_1	143,50	$0,149 \cdot 10^{-4}$
LAS_2	-117,46	$0,016 \cdot 10^{-4}$

### Conclusions

In comparison with the base sample LAS1, the modulus of elasticity increases slightly with the contribution of Zr, Corrosion rate decreases with zirconium addition, which makes it interesting to carry out future research in this line of work.



---

*28th International Symposium on Analytical and Environmental Problems*

---



***PROCEEDINGS OF THE***

***28<sup>th</sup> International Symposium  
on Analytical and Environmental Problems***

*Szeged, Hungary  
November 14-15, 2022*





# STUDY OF THE METALLOGRAPHIC STRUCTURE OF TWO TITANIUM ALLOYS FOR BIOMEDICAL PROSTHESES

*H. Guerra-Yáñez<sup>1</sup>, S.J. Brito-Gracia<sup>1</sup>, I. Voiculescu<sup>2</sup>, J.C. Mirza-Rosca<sup>1</sup>*

<sup>1</sup> Mechanical Engineering Dept., University of Las Palmas de Gran Canaria, University Campus of Tafira, Engineering building, 35017, Las Palmas de Gran Canaria, Spain

<sup>2</sup> Faculty of Industrial Engineering and Robotics, Politehnica University of Bucharest, 313 Splaiul Independentei, 060042 Bucharest, Romania

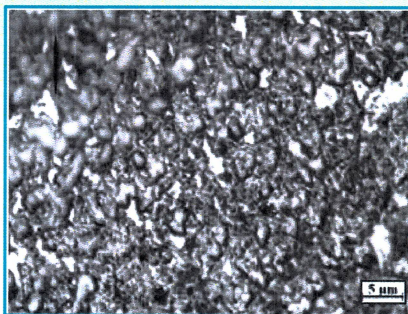
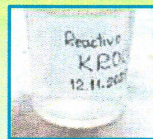
## Studied samples



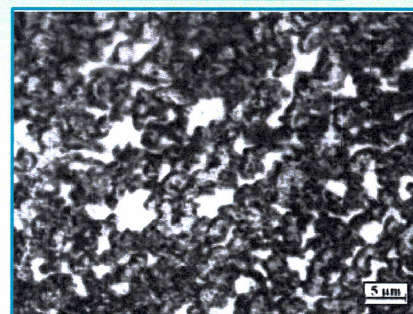
Element	Ti4Fe	Ti10Al
Ti	93.2%	89.5%
Mn	-	-
V	0.8%	0.5%
Fe	4%	-
Al	2%	10%

## Composition

## Images obtained



**Ti4FE**



**Ti10Al**

## CONCLUSIONS

- By applying Kroll's reagent, the structure of the studied titanium alloys can be appreciated.
- A time of 5 seconds resulted optimal for performing the metallographic test, shorter or longer times of submersion did not result in acceptable results.
- 100x magnifications are enough to appreciate the metallographic structure of the alloys.
- The presence of two different allotropic forms of titanium is confirmed by the presence of two regions.
- The Ti10Al alloy presents a notable number of regions affected by the chemical attack of the Kroll reactive.





# ROMAT 2022



**9<sup>th</sup> International Conference on Materials Science  
and Technologies – RoMat 2022**



**Bucharest, Romania  
November 24-25<sup>th</sup>, 2022**



S.J Brito-Garcia<sup>1</sup>, I. Voiculescu<sup>2</sup>, V. Geanta<sup>2</sup>, J. Mirza-Rosca<sup>1</sup>

<sup>1</sup> Mechanical Engineering Department, Las Palmas de Gran Canaria University, 35017 Tafia, Spain

<sup>2</sup> Faculty of Industrial Engineering and Robotics, Politehnica University of Bucharest, 313 Splaiul

### Introduction

A base alloy is designed, a high entropy multicomponent alloy with pure elements (99.95%), formed by the system Cr, Co, Fe, Mo and Ni (LAS1) and from this alloy other alloy is obtained by adding another component to the alloy. In alloy, Zr is added (LAS3) in order to study the mechanical behavior and corrosion behavior. Simulated corrosive solution was used to characterize the corrosion behavior of these materials by electrochemical techniques.

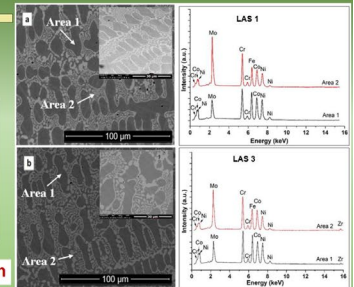
### Alloys

At %	Cr	Co	Fe	Mo	Ni	Zr
LAS1	23,58	21,52	21,84	12,92	20,14	
LAS3	23,33	21,15	22,20	12,25	20,60	0,48

### EDS quantification results

El.	LAS 1		LAS 3	
	Area 1	Area 2	Area 1	Area 2
Al	13.86	8.85	30.55	20.61
Cr	19.23	22.07	20.42	25.12
Fe	22.02	23.53	16.29	18.66
Co	22.49	22.78	18.34	19.91
Ni	22.41	22.78	14.40	15.69
Zr	-	-	-	0.59
				0.39
				0.8
				0.55

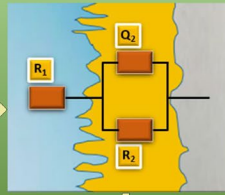
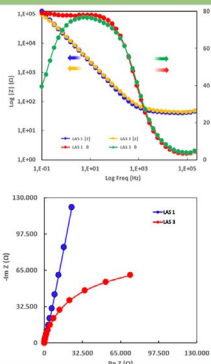
### SEM micrographs and corresponding EDS spectra LAS 1 and LAS 3



### Electrochemical techniques

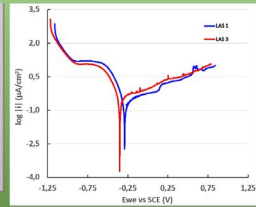


### EIS



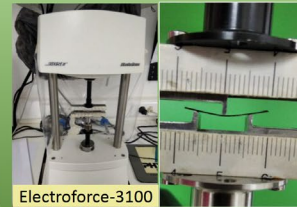
	LAS 1	LAS 3
$R_1$ (Ω)	42.70	45.09
$Q_2$ (F S <sup>-2</sup> )	$1.20 \cdot 10^{-5}$	$1.12 \cdot 10^{-5}$
$Q_2$ n	0.87	0.87
$R_2$ (Ω)	$2.5 \cdot 10^3$	$1.4 \cdot 10^3$
$\chi^2$	$1.84 \cdot 10^{-3}$	$1.87 \cdot 10^{-3}$

### Linear polarisation



	$E_{corr}$ mV	$i_{corr}$ mA/cm²	$R_p$ KΩ cm²	$mmpy$
LAS 1	-288,51	$1,86 \cdot 10^{-4}$	$2,90 \cdot 10^2$	$2,95 \cdot 10^{-3}$
LAS 3	-348,65	$2,63 \cdot 10^{-4}$	$1,76 \cdot 10^2$	$3,40 \cdot 10^{-3}$

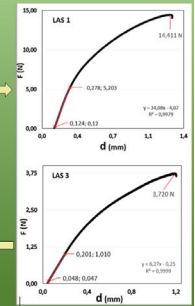
### Three-point flexion



Electroforce-3100

### Modulus of elasticity

	Modulus of elasticity GPa
LAS 1	$173,99 \pm 4,25$
LAS 3	$144,33 \pm 5,38$



### Conclusions

In comparison with the base sample LAS1, the modulus of elasticity decreases slightly, 17,05%, with the addition of Zr. The corrosion rate increases slightly, 15,25% with zirconium addition, which makes it interesting to carry out future research in this line of work.





[www.microscopy.org/MandM/2023](http://www.microscopy.org/MandM/2023)  
for up-to-date meeting information

# CALL FOR PAPERS

Submission Deadline: **February 16, 2023**



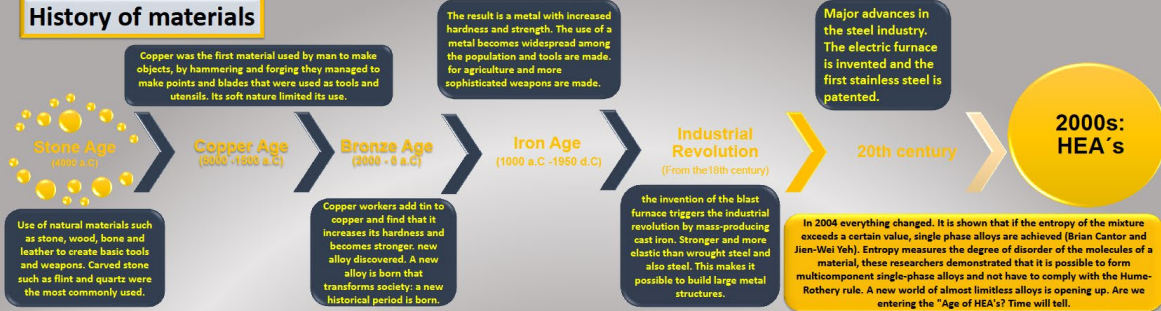
**M&M 2023**  
**MICROSCOPY &  
MICROANALYSIS**  
Minneapolis, MN • July 23-27



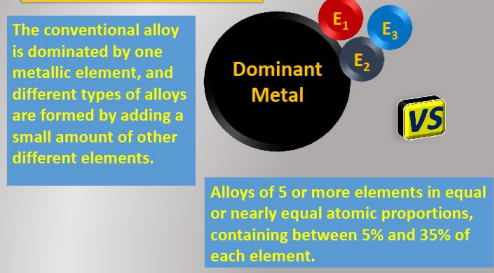


Santiago BRITO GARCIA<sup>1</sup>, Julia Claudia MIRZA ROSCAI<sup>1\*</sup>, Victor GEANTA<sup>2</sup>, Ionelia VOICULESCU<sup>2</sup>  
<sup>1</sup>Mechanical Engineering Department, University of Las Palmas de Gran Canaria, Campus Universitario, Edificio EMI, Ingenieros, 35017, Gran Canaria, Spain  
<sup>2</sup>Faculty of Industrial Engineering and Robotics, Politehnica University of Bucharest, 113 National Route, Bucharest, 060021, Bucharest, Romania  
\*julia.mirza@ulpgc.es

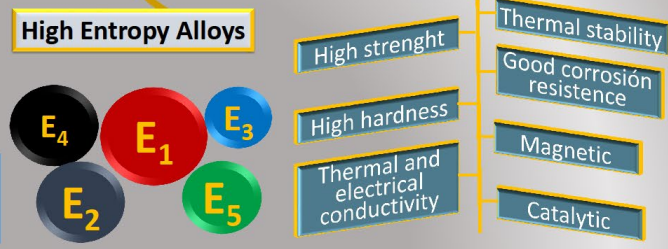
**History of materials**



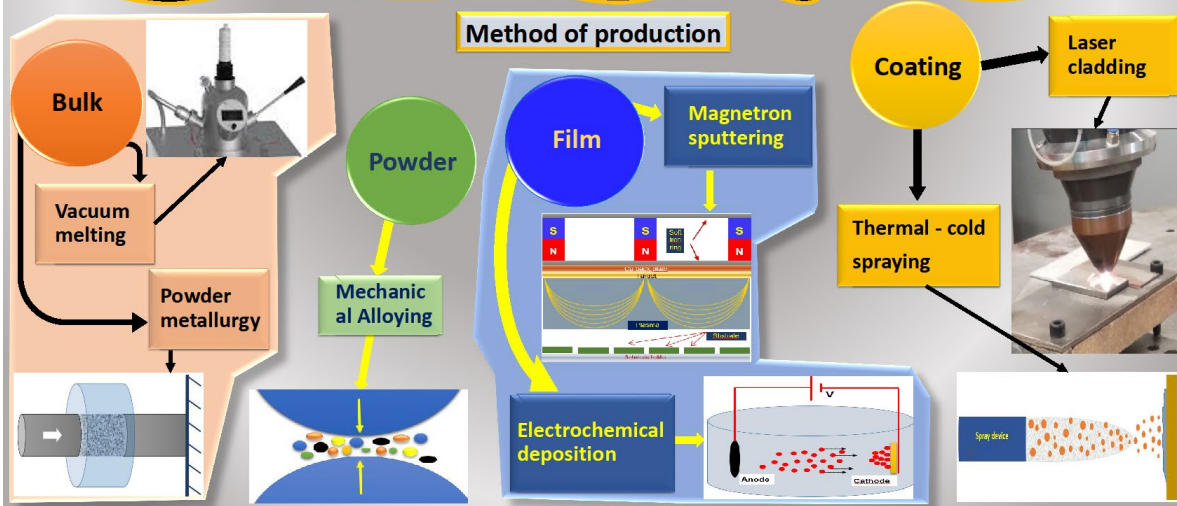
**Conventional alloys**



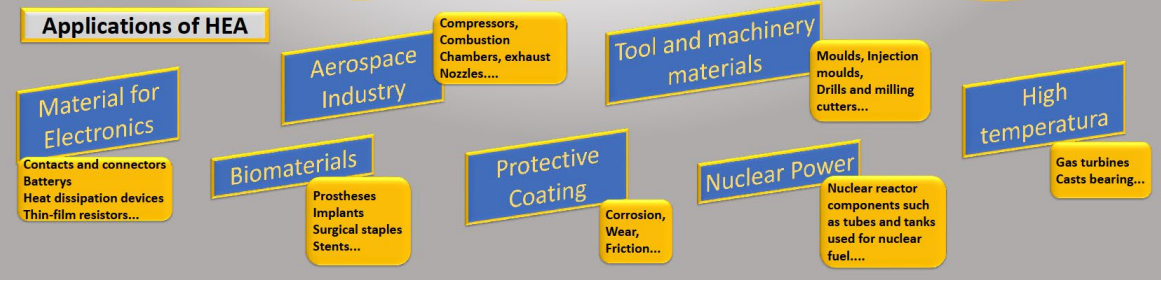
**Unique properties**



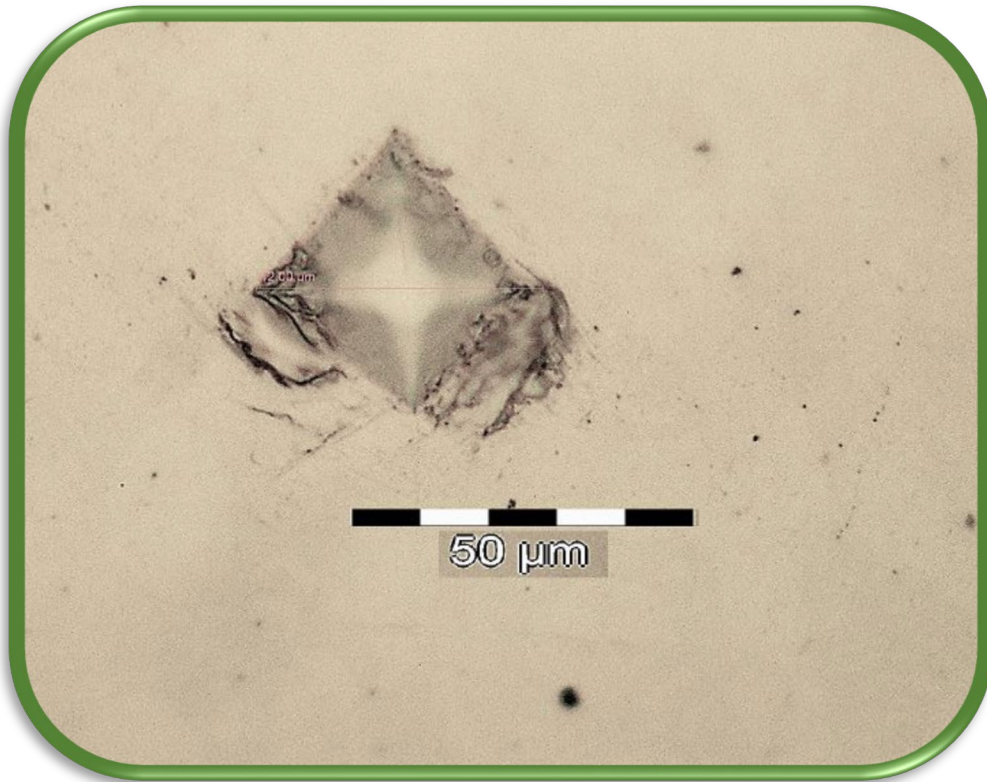
**Method of production**



**Applications of HEA**







Conclusiones

6



## 7. Conclusiones

Se sintetizan las principales conclusiones derivadas de la investigación y que se encuentran recogidas en las publicaciones científicas.

Las conclusiones son las siguientes:

- En ambas aleaciones se observó una fractura frágil con un plano de fractura similar a la hendidura.
- La aleación sin circonio era más resistente a la corrosión, con una tasa de corrosión muy baja ( $2,44 \times 10^{-3}$  mmpy en comparación con  $2,80 \times 10^{-3}$  mmpy para la muestra con Zr).
- La resistencia de la película pasiva disminuyó con la adición de Zr (de  $2,57 \times 10^7$  k $\Omega$ -cm<sup>2</sup> a  $1,47 \times 10^5$  k $\Omega$ -cm<sup>2</sup>) debido al aumento del número de puntos defectuosos en la película.
- El dopaje con 0,71 % en peso de Zr produjo un refinamiento del grano y aumentó la dureza, pero no incrementó el módulo de elasticidad ni la resistencia a la corrosión de la aleación CoCrFeNiMo.
- Por encima de 0,25 V frente a SCE, la muestra HEATi sufre corrosión por picaduras. La razón de la corrosión por picaduras en la aleación HEATi puede explicarse por la disolución preferente de iones de hierro en el electrolito debido al aumento de la relación de segregación de Fe cuando la aleación de alta entropía está dopada con Ti.

- El dopaje de la aleación CoCrFeMoNi con 0,36 at. % de Ti reduce la capacidad de la aleación para resistir la corrosión, ya que la aleación puede reaccionar más rápidamente con el entorno y provocar una disminución de la resistencia a la corrosión de la aleación.
- Se examinó la aleación de alta entropía CoCrFeMoNi para determinar el impacto del dopaje con Ti en su microestructura y propiedades mecánicas. El análisis de la microestructura reveló una matriz fundamental que consistía en fases cúbicas centradas en la cara (FCC) y cúbicas centradas en el cuerpo (BCC), junto con la formación de una fase Laves. Al añadir el dopante de Ti, se produjo un notable refinamiento de los granos dentro de la aleación. Además, se redujo la disparidad entre la concentración de Mo en las regiones interdendríticas y dendríticas. El aumento del dopado de Ti también dio lugar a un incremento de la microdureza, que se midió en 451 HV 0,2, frente a 369 HV 0,2. Este aspecto puede tenerse en cuenta a la hora de evaluar la calidad de la aleación. Este aspecto puede tenerse en cuenta a la hora de diseñar la aleación para condiciones en las que se requiera una mayor dureza o una buena resistencia al desgaste. Sin embargo, a pesar del aumento de los valores de resistencia a la rotura y microdureza, no se observaron modificaciones significativas en el módulo elástico de la aleación HEATi.

